1476

Université de Neuchâtel

Institut de Microtechnique

Distance Measurement by Multiple-Wavelength Interferometry

Thèse

présentée à la Faculté des sciences
pour obtenir le grade de docteur ès sciences

par

Yves Salvadé

Neuchâtel, juillet 1999

Université de Neuchâtel

Institut de Microtechnique

Distance Measurement by Multiple-Wavelength Interferometry

Thèse

présentée à la Faculté des sciences
pour obtenir le grade de docteur ès sciences

par

Yves Salvadé

Neuchâtel, juillet 1999

IMPRIMATUR POUR LA THÈSE

Distance measurement by multiple-wavelength interferometry

de M. Yves Salvadé

UNIVERSITÉ DE NEUCHÂTEL

FACULTÉ DES SCIENCES

La Faculté des sciences de l'Université de Neuchâtel sur le rapport des membres du jury,

MM. R. Dändliker (directeur de thèse), H.-P. Herzig, P. Thomann (Neuchâtel) et H. Tiziani (Stuttgart)

autorise l'impression de la présente thèse.

Neuchâtel, le 22 avril 1999

Le doyen:

F. Stoeckli

F. Stoeckli

Abstract

In this thesis, the application of multiple-wavelength interferometry to highly accurate distance measurement is discussed. Multiple-wavelength interferometry is, like classical interferometry, a coherent method, but it offers great flexibility in sensitivity by an appropriate choice of the different wavelengths. Indeed, the interferometric measurement at different well-known optical wavelengths enables the generation of new synthetic wavelengths, which are much longer than the optical wavelengths. Multiple-wavelength interferometry allows therefore to increase the range of unambiguity and to reduce the sensitivity of classical interferometry. Moreover it can be operated on rough surfaces. The accuracy depends essentially on the properties of the source and on the signal processing. Some solutions for the signal processing and calibration of multiple-wavelength sources are discussed in this thesis.

An electronically calibrated three-wavelength source for synthetic wavelengths in the millimeter range with an accuracy of better than 10^{-5} has been demonstrated. Using tunable DBR laser diodes, the synthetic wavelength can be chosen anywhere within 0.5 mm and 200 mm. Moreover, a compact multiple-wavelength source can be obtained using commercially available fiber-optic Fabry-Pérot resonator.

Signal processing based on heterodyne technique allows to obtain a signal which is directly sensitive to the synthetic wavelength rather than to the optical wavelength. This is of a great importance, since interferometric stability at the optical wavelength is not any more required. Absolute distance measurements were performed over 200 mm with an accuracy of 10 µm on cooperative (reflecting) targets. Using a custom designed CCD and an appropriate signal processing, distance resolution better than 10 µm has been obtained on non-cooperative (rough) targets. Moreover, we show that only a few mW of total optical power is required for the measurements at several meter distance, using appropriate beamshaping optics.

Finally, limitations of multiple-wavelength interferometry caused by the frequency noise of laser diodes are discussed.

Table of contents

1. Introduction **1**

2. Basic concepts of multiple-wavelength interferometry **4**

2.1 Interference phenomena 4

2.2 Classical interferometry 6

2.3 Multiple-Wavelength Interferometry 8

2.4 Signal processing for MWI 11

2.5 Temporal coherence of lasers 13

3. Multiple-Wavelength Source **18**

3.1 Overview of the existing laser sources for MWI 18

3.2 Frequency stabilization of semiconductor lasers 21
3.2.1 Frequency reference 21
3.2.2 Frequency stabilization principle 23

3.3 Multiple-wavelength source with electronic calibration 27
3.3.1 Principle of operation 27
3.3.2 Experiment 29
3.3.3 Synthetic wavelength calibration 30
3.3.4 Limitations of the multiple-wavelength source calibration 32

3.4 High-power multiple-wavelength source 33
3.4.1 Semiconductor optical amplifier 33
3.4.2 High-power DBR laser diodes 34

3.5 Fiber-optic Fabry-Pérot resonator 36
3.5.1 Fiber Fabry-Pérot resonator using Bragg grating reflectors 36
3.5.2 Fiber Fabry-Pérot resonator with dielectric mirrors 42
3.6 Conclusions 44

4. Heterodyne techniques for Multiple-Wavelength Interferometry **48**

4.1 Superheterodyne detection 48

4.2 Three-wavelength heterodyne interferometer 49

4.3 Two-dimensional measurements 53

4.4 Heterodyne frequency generation with movable reference mirror 55

4.5 Noise consideration 57
4.5.1 Lock-in CCD sensitivity 57
4.5.2 Noise in photodetection 58
4.5.3 Signal-to-noise ratio for heterodyne detection 59
4.5.4 Variations of sensitivity between samples 62

5. Distance measurements on non-cooperative targets by MWl 65

5.1 Statistical properties of speckle pattern 65
5.1.1 First-order statistics 66
5.1.2 Second-order statistics of speckle pattern 71
5.1.3 Speckle statistics in two-wavelength interferometry 75

5.2 Experimental results 80

5.3 Power limitation 83

6. Limitations of interferometry due to the frequency fluctuations of laser diodes 87

6.1 Instantaneous phase fluctuations 87

6.2 Integrated phase fluctuations 89

6.3 White frequency noise spectrum 90

6.4 Frequency noise spectrum of stabilized laser diodes 91

6.5 Frequency noise of DBR laser diodes 96

6.6 Conclusion 96

7. Conclusion 98

Annex A. Complex degree of correlation between speckle fields in the image plane for two-wavelength interferometry 101

Annex B. Calculation of the variance of the frequency fluctuations observed during the coherence time 106

Chapter 1

Introduction

Since the advent of lasers in 1960, distances or displacement measurements by optical techniques became very attractive in a wide range of activities. Examples of applications are machine tool calibration, geodesy, shape measurements in aircraft industry, surveying systems and robotics. The main advantage of optical metrology is the non-destructive probing of the test object. A great variety of products are nowadays commercially available with different measurement techniques.

Triangulation techniques as well as time-of-flight systems are non-coherent methods for distance measurements. The measurement accuracy of such techniques is typically larger than the millimeter. On the other hand, coherent methods, based on interferometry, enable high precision measurements of distances or displacements.

Classical interferometry is commonly used for high-resolution displacement measurements. Resolution better than 100 nm is obtained by using commercially available interferometers. However, the main drawback of this technique is the incremental manner of measuring, resulting from the counting of optical fringes. Several alternative interferometric methods, based on multiple-wavelength interferometry or white-light interferometry, have been developed in order to perform absolute distance measurements.

In 1895, A. A. Michelson and J.-R. Benoit managed to determine the number of wavelengths of the cadmium red line in the international meter prototype [1.1]. Although red cadmium line was the most coherent source in those days, interferometric measurements above 10 cm with such a light source was a difficult task. They determined therefore the number of wavelengths in an etalon of 10 cm length, with a resolution of 1/50 of a fringe, and they compared this etalon with the meter prototype. For this task, they used eight intermediate etalons with lengths of $10x2^{-1}$ cm, $10x2^{-2}$ cm,..., $10x2^{-8}$ cm. They counted at first the number of wavelengths in the smallest etalon, and compared it with the second etalon which is two times larger. This comparison procedure was performed by moving the smallest one over a distance which is equal to its own length. Observation of white-light interferences allowed to measure the optical path difference between the two rear sides of the etalons. Quasi-monochromatic light was then used to determine the excess fraction of the

interferometric fringe. Comparisons between different etalons were carried out similarly, in order to determine the number of wavelengths in the 10 cm long etalon. After each comparison, the excess fractions were measured with red, green and blue emission lines of the cadmium. Michelson and Benoit concluded that the use of several colors make it possible to directly measure the number of wavelengths in the etalons, without other operation. Principles of classical, white-light and multiple-wavelength interferometry were therefore known as early as 1895.

Today, the use of highly coherent lasers allows to measure displacements or distances up to at least 10 m by interferometric techniques. Moreover, data acquisition and electronic signal processing techniques enable fast and high-resolution measurements. Therefore, multiple-wavelength interferometry becomes of a great interest for large distance measurements with micrometer accuracy for industrial applications.

The work reported in this thesis is the result of a fruitful collaboration between IMT (Institut de Microtechnique, Neuchâtel), CSEM Zürich (formerly Paul Scherrer Institute) and Leica AG (Unterentfelden). The work was supported by the Swiss Priority Program "OPTIQUE". The goal of the project was the development of a new measuring system for large distance measurements with micrometer accuracy on non-cooperative (diffusing) targets. After a first project phase, multiple-wavelength interferometry has been chosen to be the most promising approach.

Most parts of this work have already been published and presented at international conferences:

[A] E. Zimmermann, Y. Salvadé and R. Dändliker, "Stabilized three-wavelength source calibrated by electronic means for high-accuracy absolute distance measurement", *Opt. Lett.* **21** (7), 531-533 (1995).

[B] R. Dändliker, Y. Salvadé and E. Zimmermann, "Distance measurement by multiple-wavelength interferometry", *J. Opt.* **29** (3), 105-114 (1998).

[C] Y. Salvadé, E. Zimmermann and R. Dändliker, "Limitations of interferometry due to frequency fluctuations of laser diodes", *Proc. Topical Meeting on Optoelectronic/ Displacement Measurements and Applications* (EOS, Nantes, 1997).

The basic concepts of this work are discussed in chapter 2. We will here present the principles of classical and multiple-wavelength interferometry, the principle of heterodyne detection, and the concept of temporal coherence.

The performance of multiple-wavelength interferometry is mainly given by the properties of the source (coherence, stability, power). The optimization of the multiple-

wavelength source is therefore an important task. A novel concept of multiple-wavelength source is presented in chapter 3. It allows an electronic calibration of the synthetic wavelength by beat frequency measurement. Further improvements to make the source more compact and suitable for measurements on non-cooperative targets will then be reported.

Earlier studies [I.2] were carried out several years ago at IMT to develop superheterodyne detection for high-resolution measurements at arbitrary synthetic wavelengths. Similar detection schemes were used in this work and are presented in chapter 4. Specially, we describe the use of a novel type of CCD detector for two-dimensional detection.

Chapter 5 is concerned with the applications of multiple-wavelength interferometry to non-cooperative targets. The scattering of coherent light on rough surface gives rise to a random variation of the light intensity. An appropriate signal processing will be discussed in order to improve the probability of detection. Statistical properties of the interference signal are considered for that purpose. Results of measurements on non-cooperative targets will be presented.

A well-known limitation of interferometry is the coherence length of the source. In addition, the phase fluctuations become more important for increasing distances. These phase fluctuations are related to the frequency noise spectrum of the source. The frequency noise spectrum of laser diodes is composed of two parts: a white noise part and a flicker (1/f) noise part, which may become a limiting factor for interferometry. We investigate in chapter 6 the effect of this 1/f noise part on the phase fluctuations observed at large distances.

References

[1.1] A. A. Michelson and J. R. Benoit, "Détermination expérimentale de la valeur du mètre en longueurs d'ondes lumineuses", *Trav. Mem. Bur. Int. Poids Mes.* **11**, 1 (1895)

[1.2] R. Dändliker, R. Thalmann and D. Prongué, " Two-wavelength laser interferometry using superheterodyne detection", *Optics Letters* **13**, 339-341 (1988).

Chapter 2

Basic concepts of multiple-wavelength interferometry

Absolute distance measurements cannot be covered by classical (i.e. one-wavelength) interferometry since the range of non-ambiguity is limited to half the optical wavelength (< 1 μm). However, the range of non-ambiguity can be extended by using several wavelengths [2.1, 2.2]. This will also reduce the sensitivity of classical interferometry.

The aim of this chapter is to explain the basic concepts of multiple-wavelength interferometry (MWI). For this task, we will shortly describe the interference phenomena between monochromatic waves in the first section. The one-wavelength Michelson interferometer will be presented in the second section of this chapter. Two-wavelength will then be considered as light source for this interferometer in order to understand how the non-ambiguity range can be extended. Signal processing for MWI, based on heterodyne detection, will be shortly discussed. Finally, the concept of temporal coherence will be considered in the last section, since this is a fundamental limitation of interferometry.

2.1 Interference phenomena

Interference is a typical property of all wave propagations. This phenomena is the result of the superposition of coherent waves, i.e. waves which have a phase relation between them. In optics, interference between two monochromatic light beams can be explained by considering the addition of the corresponding electro-magnetic waves.

In order to simplify the calculations, the wave propagation is assumed to be in a homogeneous and isotropic medium, and the electromagnetic waves will be described by using scalar complex wavefunctions. For a wave propagating in a medium of permittivity ε and permeability μ, the electric field can be expressed as

$$E(\mathbf{r},t) = \left(\frac{4\mu\mu_0}{\varepsilon\varepsilon_0}\right)^{1/4} \mathrm{Re}\{U(\mathbf{r},t)\}, \tag{2.1}$$

where t is the time, **r** is the vector-position, ε_0 and μ_0 are the permittivity and permeability of vacuum, respectively. The complex wavefunction is defined so that the

light intensity, which is the amount energy per unit time and per unit area [2.3], can be calculated from the simple relation

$$I(\mathbf{r}) = |U(\mathbf{r},t)|^2. \tag{2.2}$$

For a monochromatic wave of optical frequency ν, the complex wavefunction can be written in the form

$$U(\mathbf{r},t) = V(\mathbf{r})\exp(i2\pi\nu t), \tag{2.3}$$

where

$$V(\mathbf{r}) = a(\mathbf{r})\exp[i\phi(\mathbf{r})] \ . \tag{2.4}$$

The real functions $a(\mathbf{r})$ and $\phi(\mathbf{r})$ are the real amplitude and the phase of the electromagnetic wave, respectively. $V(\mathbf{r})$ is known as the complex amplitude.

By substituting Eq. (2.3) and (2.4) into (2.2), we find that the light intensity is given by

$$I(\mathbf{r}) = |V(\mathbf{r})|^2 = a(\mathbf{r})^2. \tag{2.5}$$

Let us consider two monochromatic waves with the same optical frequency. Their complex amplitudes can be written in the form

$$V_1(\mathbf{r}) = \sqrt{I_1(\mathbf{r})}\exp[i\phi_1(\mathbf{r})] \text{ and } V_2(\mathbf{r}) = \sqrt{I_2(\mathbf{r})}\exp[i\phi_2(\mathbf{r})] \ , \tag{2.6}$$

where I_1, I_2 and ϕ_1, ϕ_2 are the intensities and the phases of both individual waves, respectively. Their superposition gives rise to a resulting wave with the complex amplitude

$$V_3(\mathbf{r}) = V_1(\mathbf{r}) + V_2(\mathbf{r}). \tag{2.7}$$

The corresponding intensity is therefore given by

$$I_3(\mathbf{r}) = |V_1(\mathbf{r}) + V_2(\mathbf{r})|^2 = |V_1(\mathbf{r})|^2 + |V_2(\mathbf{r})|^2 + 2\cdot \mathrm{Re}\{V_1(\mathbf{r})V_2(\mathbf{r})^*\}. \tag{2.8}$$

The last term of Eq. (2.8), i.e. $2\,\mathrm{Re}\{V_1V_2^*\}$, denotes the interference between the two monochromatic waves [2.4]. Substituting (2.6) into (2.8), we obtain

$$I_3(\mathbf{r}) = I_1(\mathbf{r}) + I_2(\mathbf{r}) + 2\sqrt{I_1(\mathbf{r})I_2(\mathbf{r})}\cdot\cos[\phi_1(\mathbf{r}) - \phi_2(\mathbf{r})]. \tag{2.9}$$

The intensity resulting from the superposition of two monochromatic waves is therefore not necessarily the addition of the individual intensities. Indeed, an additional

interference term appears in the equation of the resulting intensity, which depends on the phase difference between the two waves. Coherent methods for distance or displacement measurements are based on this interference phenomena.

2.2 Classical interferometry

An interferometer is an optical instrument which divides an incident beam into two beams, delays them by making them travelling over two different paths, recombines them at the output, and detects the resulting intensity. This task can be achieved by using different optical configurations. Examples are Mach-Zehnder, Michelson, Sagnac or Twymann-Green interferometers. The most commonly used interferometer for displacement measurement is the Michelson interferometer [2.5]. It is composed of a single beamsplitter which is used for dividing and recombining the waves, a fixed reference mirror and a movable measurement mirror. Figure 2.1 shows a Michelson interferometer with a path difference L between the reference and the measuring arms. In classical interferometry, a quasi-monochromatic wave is injected in the Michelson interferometer. Stabilized HeNe lasers are often used in industrial interferometers for displacement measurement (e.g. Hewlett-Packard interferometers). However, compact and low-cost Michelson interferometers were developed by using stabilized laser diodes as light sources [2.6, 2.7].

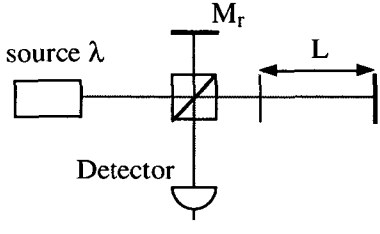

Figure 2.1: Michelson interferometer set-up.

Most lasers used for interferometry emit a Gaussian beam. However, for the following we will approximate the laser beam by a plane wave to simplify the calculations. The complex amplitude of a plane wave is

$$V(\mathbf{r}) = V_0 \exp\{-i\mathbf{k}\,\mathbf{r}\}, \tag{2.10}$$

where V_0 is the amplitude, and $\mathbf{k}$ is the wave vector [2.3]. In a medium of refractive index n, the magnitude of the wave vector is given by

$$k = n2\pi/\lambda_0 = 2\pi\nu/c \tag{2.11}$$

where λ_0 and c are the wavelength and the velocity of the light in vacuum, respectively. To simplify, we assume a wave propagating in the z-direction so that Eq. (2.10) becomes

$$V(z) = V_0 \exp\{-ikz\}. \tag{2.12}$$

By using Eq. (2.11) and (2.12), it can be shown that the phase difference $\Delta\phi = \phi_1 - \phi_2$ gets

$$\Delta\phi = \frac{2\pi n}{\lambda} 2L. \tag{2.13}$$

The interference signal can then be determined by substituting $\Delta\phi$ in Eq. (2.9), i.e.

$$I(L) = I_1 + I_2 + 2\sqrt{I_1 I_2}\cos\left(\frac{2\pi n}{\lambda} 2L\right). \tag{2.14}$$

The intensity will therefore depend on the optical path difference between the two arms of the interferometer. Figure 2.2 shows the detected output intensity as a function of the interferometric path difference L for a refractive index n = I.

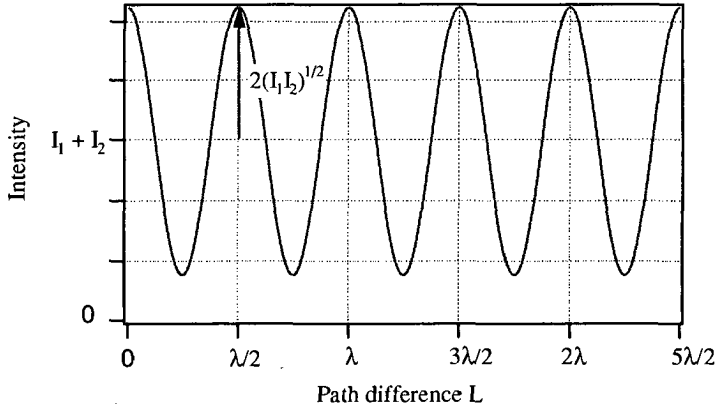

Figure 2.2: Interference signal as a function of the optical path difference L.

We note that the period of the interference signal is given by λ/2. The range of non-ambiguity, i.e. the range of distance which can be deduced unambiguously from the detected intensity, is therefore limited to half the optical wavelength. However, displacement can be measured accurately by counting the number of periods and by fringe interpolation. The distance is therefore measured incrementally. Many industrial

products for displacement measurements are based on classical interferometry (e.g. Hewlett-Packard, Zygo). In addition, advanced interferometric systems are able to follow a prism retroreflector using a tracking system (e.g. laser tracking interferometer LT500 from Leica) . This enables to scan the shape of large objects.

However, incremental measurement is a severe restriction in many cases. Moreover, it should be noted that classical interferometry is not applicable to optically rough surfaces, because of the randomly distributed phase of the diffused light (speckle effect) [2.8, 2.9, 2.10].

2.3 Multiple-Wavelength Interferometry

Multiple-wavelength interferometry is also a coherent method, but it offers great flexibility in sensitivity by an appropriate choice of the different wavelengths [2.11, 2.12].

For instance, let us consider two-wavelength interferometry using the optical wavelengths λ_1 and λ_2. For an interferometric path difference L, the phases ϕ_1 and ϕ_2 corresponding to the wavelengths λ_1 and λ_2 are given, for n = 1, by

$$\Delta\phi_1 = \frac{2\pi}{\lambda_1}2L \text{ and } \Delta\phi_2 = \frac{2\pi}{\lambda_2}2L. \tag{2.15}$$

The phase difference between ϕ_1 and ϕ_2 is therefore given by

$$\Delta\phi_{12} = \Delta\phi_1 - \Delta\phi_2 = 2\pi\left(\frac{1}{\lambda_1} - \frac{1}{\lambda_2}\right)2L = \frac{2\pi}{\Lambda}2L. \tag{2.16}$$

The phase difference is thus sensitive to a new synthetic wavelength Λ, which can be expressed as

$$\Lambda = \frac{\lambda_1\lambda_2}{|\lambda_1 - \lambda_2|} = \frac{c}{|\nu_1 - \nu_2|}. \tag{2.17}$$

Therefore, the use of two slightly different wavelengths permits to generate a new synthetic wavelength much longer than the individual optical wavelengths. The range of non-ambiguity of the phase difference $\Delta\phi_{12}$, which is also known as the synthetic phase, is therefore increased compared to the range of non-ambiguity of classical interferometry. Moreover, the sensitivity of the measurement is reduced.

Two-wavelength interferometry can be accomplished by injecting two wavelengths simultaneously into the interferometer, and by optically separating them at the output

using a prism or a grating [2.8, 2.9], as shown in Fig. 2.3. Both interference signals are then detected individually. The synthetic phase can be determined by measuring the interferometric phases at both wavelengths, and by computing the difference. However, this method works only for relatively large wavelength differences and thus small synthetic wavelengths (< 1 mm), since both wavelengths have to be separated by means of a prism or a grating. Moreover, this method requires interferometric stability at the optical wavelength, which is difficult to achieve in applications where reduced sensitivity is desired and sufficient.

Alternative methods [2.11, 2.12, 2.13, 2.14, 2.15] can be used to solve this problem by detecting the total interference signal without any optical separation of the two wavelengths. The complex amplitudes are given by two contributions at the wavelengths λ_1 and λ_2, namely

$$U(t) = U_{\lambda 1}(t) + U_{\lambda 2}(t), \tag{2.18}$$

with

$$U_{\lambda 1}(t) = V_{\lambda 1} \exp(i2\pi\nu_1 t) \quad \text{and} \quad U_{\lambda 2}(t) = V_{\lambda 2} \exp(i2\pi\nu_2 t), \tag{2.19}$$

where ν_1 and ν_2 are the optical frequencies corresponding to λ_1 and λ_2.

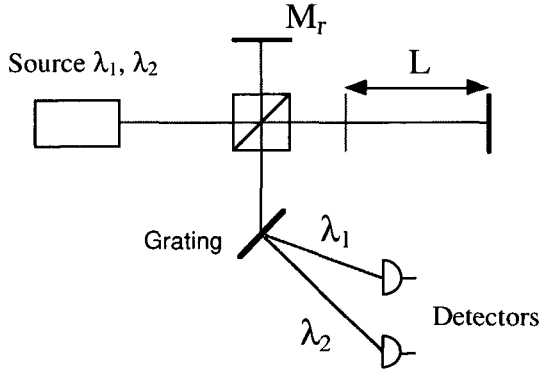

Figure 2.3: Two-wavelength interferometer with optical separation of both wavelengths.

After beam recombination, one gets the superposition of the reference wave and the measuring wave, which is delayed by the time $\tau = 2L/c$. If the two waves are of equal intensity, the averaged interference signal becomes

$$I(\tau) = \left\langle |U(t) + U(t-\tau)|^2 \right\rangle = 2\left(I_{\lambda 1} + I_{\lambda 2}\right) + 2\,\mathrm{Re}\left\{\left\langle U(t)U^*(t-\tau)\right\rangle\right\}, \tag{2.20}$$

where $I_{\lambda 1} = |V_{\lambda 1}|^2$ and $I_{\lambda 2} = |V_{\lambda 2}|^2$. The brackets <> denote the time average. The interference term is therefore given by the real part of the autocorrelation function of U(t). Using Eq. (2.18), the autocorrelation function becomes,

$$\begin{aligned}\left\langle U(t)U^*(t-\tau)\right\rangle = &\left\langle U_{\lambda 1}(t)U^*_{\lambda 1}(t-\tau)\right\rangle + \left\langle U_{\lambda 2}(t)U^*_{\lambda 2}(t-\tau)\right\rangle \\ &+ \left\langle U_{\lambda 1}(t)U^*_{\lambda 2}(t-\tau)\right\rangle + \left\langle U_{\lambda 2}(t)U^*_{\lambda 1}(t-\tau)\right\rangle .\end{aligned} \tag{2.21}$$

The autocorrelation function of U(t) depends not only on the individual autocorrelation functions of $U_{\lambda 1}(t)$ and $U_{\lambda 2}(t)$, but also on the statistical relation between these two contributions, through the cross-correlation functions. However, by substituting Eq. (2.19) into the cross-correlation functions we see that

$$\begin{aligned}\left\langle U_{\lambda 1}(t)U^*_{\lambda 2}(t-\tau)\right\rangle &= V_{\lambda 1}V^*_{\lambda 2}\exp(i2\pi\nu_2\tau)\left\langle \exp[i2\pi(\nu_1-\nu_2)t]\right\rangle = 0 \\ \left\langle U_{\lambda 2}(t)U^*_{\lambda 1}(t-\tau)\right\rangle &= V_{\lambda 2}V^*_{\lambda 1}\exp(i2\pi\nu_1\tau)\left\langle \exp[i2\pi(\nu_2-\nu_1)t]\right\rangle = 0 .\end{aligned} \tag{2.22}$$

It should be noted that in practice we observe the intensity during a finite integration time. Therefore, if the detection bandwidth is larger than the frequency difference of the two sources, a beat signal at $\nu_2 - \nu_1$ can be observed. On the other hand, for longer integration times, the beat signal is not detected anymore. In that case, by using Eqs. (2.20)–(2.22), the interference signal becomes

$$I(\tau) = 2(I_{\lambda 1} + I_{\lambda 2}) + 2\,\mathrm{Re}\left\{\left\langle U_{\lambda 1}(t)U^*_{\lambda 1}(t-\tau)\right\rangle\right\} + 2\,\mathrm{Re}\left\{\left\langle U_{\lambda 2}(t)U^*_{\lambda 2}(t-\tau)\right\rangle\right\}, \tag{2.23}$$

which is simply the incoherent superposition of the individual interference signals for λ_1 and λ_2. Substituting Eq. (2.19) into Eq. (2.23), we find

$$I(\tau) = 2(I_{\lambda 1} + I_{\lambda 2}) + 2I_{\lambda 1}\cos(2\pi\nu_1\tau) + 2I_{\lambda 2}\cos(2\pi\nu_2\tau). \tag{2.24}$$

This interference signal is depicted in the upper part of Fig 2.4 as a function of the optical path difference $2L = c\tau$. We note that the modulation depth of the fringes varies periodically along the optical path difference. The fringe visibility, first introduced by Michelson, is defined by

$$\mathcal{V} = (I_{max} - I_{min})/(I_{max} + I_{min}), \tag{2.25}$$

where I_{max} and I_{min} are the intensities at the maximum and minimum of the fringes. From Eq. (2.20), it can be seen that the visibility is equal to the magnitude of the normalized autocorrelation function, namely

$$\mathcal{V}(\tau)=\left|\frac{\langle U(t)U^{*}(t-\tau)\rangle}{\langle |U(t)|^{2}\rangle}\right|. \tag{2.26}$$

Using Eq. (2.18), (2.19) and (2.26), it can be shown that the square of the fringe visibility is

$$\mathcal{V}^{2}(\tau)=1+2\frac{I_{\lambda 1}I_{\lambda 2}}{I_{\lambda 1}^{2}+I_{\lambda 2}^{2}}\cos\left[2\pi(\nu_{2}-\nu_{1})\tau\right]. \tag{2.27}$$

The lower part of Fig. 2.4 shows $\mathcal{V}^{2}$ as a function of the optical path difference. It looks like a typical interference signal, but now rather for the synthetic wavelength Λ than for the optical wavelength λ.

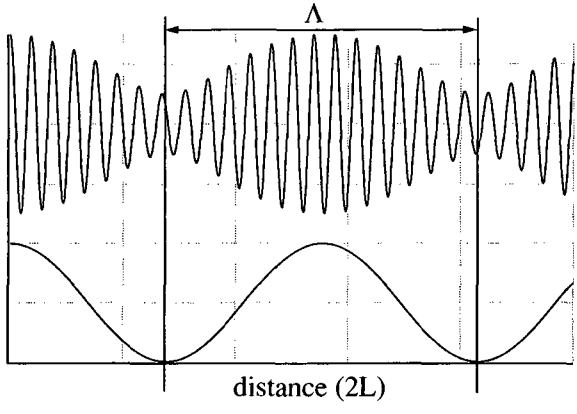

Figure 2.4: Interference signal obtained by using simultaneously two wavelengths (upper part), and the square of its corresponding fringe visibility (lower part).

2.4 Signal processing for MWI

Appropriate signal processing must be used to access the fringe visibility of the interference signal. Several detection techniques have been proposed [2.11–2.15], which are based on heterodyne detection. The aim of this section is to describe shortly this detection technique and its applications to multiple-wavelength interferometry.

Two different types of detection techniques can be used in interferometry: homodyne and heterodyne detection. Homodyne detection is a static method whereas heterodyne detection is a dynamic method [2.16]. The first one has the advantage to be simple and low-cost. However, the resolution may be limited by the intensity fluctuations of the laser.

Heterodyne technique is a powerful method to achieve high resolution fringe interpolation. It allows also shot noise limited detection even for low optical power in the measuring arm of the interferometer. In heterodyne interferometry an optical frequency offset f is generated between the reference and the measuring waves by means, for instance, of an acousto-optical modulator. The two waves are then given by

$$U_1(z,t) = \sqrt{I_1}\exp(i\phi_1)\exp(i2\pi\nu t) \text{ and}$$
$$U_2(z,t) = \sqrt{I_2}\exp(i\phi_2)\exp\{i2\pi(\nu+f)t\}. \qquad (2.28)$$

The interference signal, which is given by $I = |U_1 + U_2|^2$, becomes then

$$I(t) = I_1 + I_2 + 2\sqrt{I_1 I_2}\cos(2\pi ft + \Delta\phi), \qquad (2.29)$$

where $\Delta\phi = \phi_1 - \phi_2$. Therefore, heterodyne detection gives rise to a time-dependent interference signal of frequency f. The interferometric phase $\Delta\phi$ can be determined by measuring the phase difference between a reference signal, generated either optically or electronically, and the measurement signal. This allows to achieve fringe interpolation better than 1/1000 [2.17, 2.18].

Application of heterodyne technique to multiple-wavelength interferometry was first reported by Fercher et al. [2.8]. The synthetic phase is determined by measuring the interferometric phases at both wavelengths, and by computing the difference (see Fig. 2.3). This method provides fast measurement and works also for rough surfaces. However, as already mentioned, the technique can be used only for relatively large wavelength differences and thus small synthetic wavelengths Λ.

Superheterodyne detection, introduced by Dändliker et al. [2.13, 2.14], enables high-resolution measurements at arbitrary synthetic wavelengths Λ without the need for interferometric stability at the optical wavelengths λ_1 and λ_2 or separation of these wavelengths optically. This is of great importance for range finding and industrial distance measuring of large distances with sub-millimeter resolution. Both wavelengths are used to illuminate simultaneously a Michelson interferometer. Two different heterodyne frequencies f_1 and f_2 are generated for each wavelength. These frequency differences can be produced by acousto-optical modulators and are typically f_1 = 40.0 MHz and f_2 = 40.1 MHz. According to Eq. (2.29), the heterodyne signals corresponding to the individual wavelengths λ_1 and λ_2 are of the form

$$I_{\lambda 1}(t) = C_0 + C_1\cos(2\pi f_1 t + \Delta\phi_1) \text{ and } I_{\lambda 2}(t) = C_2 + C_3\cos(2\pi f_2 t + \Delta\phi_2), \qquad (2.30)$$

where the interferometric phases $\Delta\phi_1$ and $\Delta\phi_2$ are given by Eq. (2.15). Since the wavelengths are not separated optically, the interference signal is given by the incoherent superposition of $I_{\lambda 1}$ and $I_{\lambda 2}$, namely

$$I(t) = A_0 + A_1 \cos(2\pi f_1 t + \Delta\phi_1) + A_2 \cos(2\pi f_2 t + \Delta\phi_2). \tag{2.31}$$

Because $f_1 - f_2$ is chosen small compared with f_1 and f_2, the detector output has the form of a carrier-suppressed amplitude-modulated signal with carrier $(f_1+f_2)/2$ and modulation frequency $(f_1- f_2)/2$. After amplitude demodulation, one gets therefore

$$I_{dem}(t) = A_{12} \cos[2\pi(f_1 - f_2)t + (\Delta\phi_1 - \Delta\phi_2)]. \tag{2.32}$$

This signal at $f = f_1 - f_2$ makes it possible to measure directly the phase difference $\Delta\phi_1 - \Delta\phi_2 = 4\pi L/\Lambda$ which is now only sensitive to the synthetic wavelength Λ.

Simpler detection methods, which do not need separate modulation of the two wavelengths might be of interest [2.11, 2.12, 2.15]. If the two heterodyne frequencies f_1 and f_2 are chosen equal ($f_1 = f_2$), Eq. (2.31) becomes

$$I(t) = A_0 + A_1 \cos(2\pi f_1 t + \Delta\phi_1) + A_2 \cos(2\pi f_1 t + \Delta\phi_2). \tag{2.33}$$

The interference fringe function for the synthetic wavelength Λ is then obtained by detecting the electrical power of the ac part of this signal, which is

$$P_{ac} = \frac{1}{2}[A_1^2 + A_2^2 + 2A_1A_2 \cos(\Delta\phi_{12})]. \tag{2.34}$$

Equation (2.34) looks like a typical interference signal, but now rather for the synthetic wavelength Λ than for the optical wavelength λ (see Fig. 2.4). The interference phase $\Delta\phi_{12} = \Delta\phi_1 - \Delta\phi_2$ of the synthetic wavelength can now be determined by techniques similar to those used for phase interpolation in interferometry.

Schemes and apparatus for heterodyne frequency generation and detection will be discussed later in this thesis.

2.5 Temporal coherence of lasers

So far we only considered perfectly monochromatic waves. In this ideal case, displacements or distances can be measured at arbitrary large optical path differences.

However, the interfering waves are more realistically described by quasi-monochromatic waves. Indeed, single-mode laser sources have an average emission spectrum which is confined to a narrow band centered about the central frequency ν [2.19]. The spectral

width or linewidth of light is defined here as the full width at half maximum of the spectral density. Depending on the laser type, the linewidth can vary from a few kHz (gas lasers) to a few 10 MHz (standard diode lasers). The emitting frequency of the source is thus characterized by statistical fluctuations around the center frequency ν.

For an interferometer with an optical path difference L, we have to consider the superposition of two quasi-monochromatic plane waves [2.19]. The measuring wave is delayed by the time $\tau = 2L/c$. Assuming reference and measuring waves of equal intensity, the time averaged intensity becomes,

$$I = \left\langle |U(t) + U(t-\tau)|^2 \right\rangle = 2I_0 + 2\,\mathrm{Re}\left\{ \left\langle U(t)U^*(t-\tau) \right\rangle \right\}, \tag{2.35}$$

where $I_0 = \left\langle |U(t)|^2 \right\rangle$. It is convenient to work with the normalized autocorrelation function

$$g(\tau) = \frac{\left\langle U(t)U^*(t-\tau) \right\rangle}{\left\langle |U(t)|^2 \right\rangle}. \tag{2.36}$$

Equation (2.35) becomes then

$$I = 2I_0\left[1 + \mathrm{Re}\{g(\tau)\}\right]. \tag{2.37}$$

The normalized autocorrelation function $g(\tau)$ is also known as the complex degree of temporal coherence. Its magnitude $|g(\tau)|$ is a measure of the degree of correlation between U(t) and U(t-τ) [2.19]. Its value is equal to 1 for $\tau = 0$. Usually, $|g(\tau)|$ decreases with increasing τ, and the fluctuations become uncorrelated for sufficiently large time delays. Figure 2.5 shows a typical interference signal as a function of the interferometric delay τ.

It can easily be shown that the magnitude of the complex degree of temporal coherence $|g(\tau)|$ is the envelope of the interference signal. As already mentioned, it can therefore be interpreted as the interference contrast or the fringe visibility, namely

$$|g(\tau)| = \frac{I_{max}(\tau) - I_{min}(\tau)}{I_{max}(\tau) + I_{min}(\tau)}, \tag{2.38}$$

where $I_{max}(\tau)$ and $I_{min}(\tau)$ are the local maxima and minima of the intensity next to the interferometric delay τ, as shown in Fig. 2.5. For large interferometric delay, $|g(\tau)|$ becomes zero and the two interfering waves become therefore incoherent. This will limit the maximal optical path difference at which distance or displacement can be measured

by interferometry. Highly coherent lasers are thus required for large distance measurement by interferometric techniques.

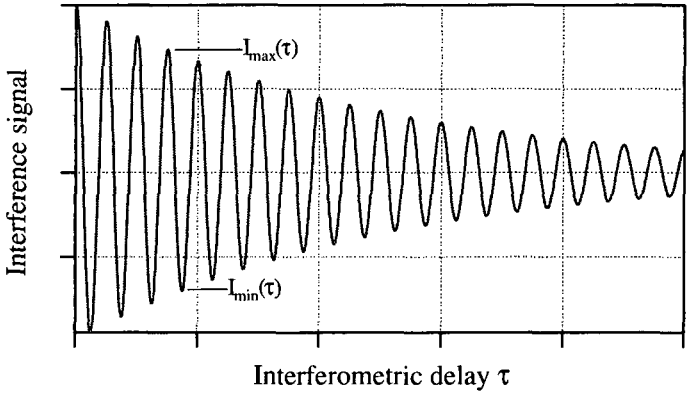

Figure 2.5: Interference signal as a function of the interferometric delay τ for a low-coherent source.

The interferometric delay at which the fringe visibility decreases to a prescribed value (e.g. 1/e or 1/2) is known as the coherence time of the source τ_c. Following Mandel [2.20], we define here the coherence time τ_c as

$$\tau_c = \int_{-\infty}^{+\infty} |g(\tau)|^2 d\tau. \tag{2.39}$$

The corresponding optical path difference is called the coherence length l_c of the source. The coherence length is therefore related to the coherence time by,

$$l_c = c\tau_c. \tag{2.40}$$

By using the well-known Wiener-Khintchine theorem, we note that the complex degree of temporal coherence $g(\tau)$ is related to the power spectral density of the source $S(\nu)$ by a Fourier transform [2.21], i.e.

$$g(\tau) = \frac{\int_0^\infty d\nu S(\nu) \exp(i2\pi\nu\tau)}{\int_0^\infty d\nu S(\nu)}. \tag{2.41}$$

Because of this Fourier-transform relation, the linewidth $\Delta\nu$ and the coherence time τ_c are inversely related. A light source of broad spectrum has a short coherence time,

whereas a laser source with narrow linewidth has a long coherence time. The exact relation between $\Delta\nu$ and τ_c depends on the lineshape function. Coherence time τ_c and interference contrast $|g(\tau)|$ for Gaussian and Lorentzian lineshape function are given in Table 2.1 [2.22].

Normalized PSD	Interference contrast $\lvert g(\tau)\rvert$	Coherence time τ_c
Lorentzian: $\dfrac{\Delta\nu/2\pi}{(\nu-\nu_0)^2+(\Delta\nu/2)^2}$	Decreasing exponential: $\exp(-\pi\Delta\nu\lvert\tau\rvert)$	$\dfrac{1}{\pi\Delta\nu}$
Gaussian: $\dfrac{2\sqrt{\ln 2/\pi}}{\Delta\nu}\exp\left[-4\ln 2\cdot\dfrac{(\nu-\nu_0)^2}{\Delta\nu^2}\right]$	Gaussian: $\exp\left[-\left(\dfrac{\pi\Delta\nu\tau}{2\sqrt{\ln 2}}\right)^2\right]$	$\dfrac{\sqrt{2\ln 2/\pi}}{\Delta\nu}$

Table 2.1: Normalized power spectral density (psd), interference contrast and coherence time for Gaussian and Lorentzian functions. The spectral width $\Delta\nu$ is the full width at half maximum value of the spectral density. The coherence time is defined by Eq. (2.39).

References

[2.1] J. C. Wyant, "Testing aspherics using two-wavelength holography", *Appl. Opt.* **10**, 2113-2118 (1971).

[2.2] C. Polhemus, "Two-wavelength interferometry", *Appl. Opt* **12**, 2071-2074 (1973).

[2.3] M. Born and E. Wolf in Principles of Optics (Pergamon Press, Oxford, 6th edition, 1980), chap. 1.4.

[2.4] M. Born and E. Wolf in Principles of Optics (Pergamon Press, Oxford, 6th edition, 1980), chap. 7.2.

[2.5] A. A. Michelson, "The relative motion of the earth and the luminiferous ether", *Amer. J. Sci.* **22**, 120-129 (1881).

[2.6] G. P. Barwood, P. Gill and W. R. C. Rowley, "A simple rubidium-stabilized laser diode for interferometric applications", *J. Phys. E: Sci. Instrum.* **21**, 966-971 (1988).

[2.7] A. Abou-Zeid, "Diode lasers for interferometry", *Prec. Eng.* **11** (3), 139-144 (1989).

[2.8] A. F. Fercher, H. Z. Hu and U. Vry, "Rough surface interferometry with a two-wavelength heterodyne speckle interferometer", *Appl. Opt.* **24**, 2181-2188 (1985).

[2.9] P. de Groot, "Interferometric laser profilometer for rough surfaces", *Opt Lett.* **16** (6), 357-359 (1991).

[2.10] R. Dändliker, M. Geiser, C. Giunti, S. Zatti, G. Margheri, "Improvement of speckle statistics in double-wavelength superheterodyne interferometry", *Appl. Opt.* **34**, 7197 (1995).

[2.11] R. Dändliker, "Distance measurements with multiple wavelength techniques", *2nd Internat. Workshop on High Precision Navigation*, ed. K. Linkwitz, U. Hangleiter, (Ferd. Dümmlers Verlag, Bonn, 1992), p. 159-170.

[2.12] R. Dändliker, K. Hug, J. Politch and E. Zimmermann, "High-accuracy distance measurements by multiple-wavelength interferometry", *Opt. Eng.* **34** (8), 2407-2412 (1995).

[2.13] R. Dändliker, R. Thalmann and D. Prongué, "Two-wavelength laser interferometry using superheterodyne detection", *Proc. SPIE* **813**, 9-10 (1987).

[2.14] R. Dändliker, R. Thalmann and D. Prongué, "Two-wavelength laser interferometry using superheterodyne detection", *Opt. Lett.* **13**, 339-341 (1988).

[2.15] R. Dändliker, Y. Salvadé and E. Zimmermann, "Distance measurement by multiple-wavelength interferometry", *J. Opt.* **29** (3), 105-114 (1998).

[2.16] H. J. Tiziani, "Optical methods for precision measurements", *Opt. Quant. Elec.* **21**, 253-282 (1989).

[2.17] R. Dändliker, "Heterodyne holographic interferometry", in *Progress in Optics*, E. Wolf, ed. (North-Holland, Amsterdam, 1980), Vol. XVII, 1-84.

[2.18] E. Zimmermann in *Signal Processing For Optical Phase Detection* (PhD Thesis, University of Neuchâtel, 1997), chap.3.

[2.19] B. E. A. Saleh and M. C. Teich in *Fundamental of Photonics* (Wiley & Sons, New York, 1991), chap. 10.

[2.20] L. Mandel, *Proc. Phys. Soc.* (London) **74**, 223 (1959)

[2.21] M. Born and E. Wolf in *Principles of Optics* (Pergamon Press, Oxford, 6th edition, 1980), chap. 10.3 – 10.4.

[2.22] J. W. Goodman in *Statistical Optics* (Wiley & Sons, New York, 1985), chap. 5.1.3

Chapter 3

Multiple-wavelength source

The source of a multiple-wavelength interferometer should produce an appropriate emission spectrum which consists of several discrete and stabilized wavelengths. As already mentioned, the range of non-ambiguity is given by the optical frequency difference. The stability and the calibration of the source will limit the absolute accuracy of the measurement. Moreover, the maximal distance which can be measured by multiple-wavelength interferometry is limited by the coherence length of the source. In addition, distance measurement on rough surfaces may be limited by the source power due to the scattering of the light. The design and the realization of the source are thus of a great importance, since the performance of the measuring set-up will be given by its properties (coherence, stability, power).

In this chapter, a novel concept of multiple-wavelength source is described, which allows to calibrate accurately the synthetic wavelengths by beat frequency measurement [3.1].

After an overview of the existing laser sources suitable for multiple-wavelength interferometry (MWI), we will discuss the stabilization technique which was used in our experiment. Then, the concept of synthetic wavelength calibration by beat frequency measurement will be described. In order to upgrade the source power and to get a more compact source, improvements of the multiple-wavelength source will finally be presented.

3.1 Overview of the existing laser sources for MWI

A multiple-wavelength source is usually composed of either a multimode laser or a combination of several lasers. Modern laser sources provide a great variety of optical frequencies or wavelengths to get interesting synthetic wavelengths.

Many gas lasers have the advantages to emit light at different wavelengths. For instance, CO_2 lasers emit at a large number of wavelengths between 9 and 11 μm, corresponding to transitions for the various vibrational-rotational levels. Bourdet and Orszag measured a length of 50 cm with an accuracy of 0.1 μm [3.2]. He-Ne lasers, which are traditionally used in most high-performance interferometers, can also be applied to MWI, using different laser lines, e.g. at 629.4 nm and 632.8 nm [3.3, 3.4]. This

allows to obtain synthetic wavelengths of about 117 µm. In addition, commercially available stabilized He-Ne lasers (e.g. Renishaw SL10) can produce two stabilized longitudinal modes with a frequency separation of about 1 GHz, corresponding to a synthetic wavelength of 30 cm. Other gas lasers, such as Ar lasers [3.5], He-Xe laser [3.6] and Kr-ion laser [3.7] have also been used in MWI experiments. The performance of these lasers is adequate. However, the discharge tube cannot be miniaturized and would not be compatible with a compact and low-cost measuring system.

Semiconductor laser diodes are currently the most energy efficient and the most compact lasers. Moreover, the emitted frequency can be tuned by changing the injection current and the temperature. Tunable lasers are of a great interest since the most appropriate synthetic wavelength can be chosen with more flexibility. However, when the most appropriate wavelength is chosen, they have to be frequency stabilized on an external reference.

Multimode laser diodes oscillate at a number of discrete wavelengths simultaneously, which provide a range of stable synthetic wavelengths if the laser is temperature controlled. The frequency separation $\Delta\nu$ between longitudinal modes is inversely related to the resonator length d by $\Delta\nu = c/2nd$, where n is the semiconductor refractive index ($n \approx 3.5$ for AlGaAs). The maximal synthetic wavelength which can be obtained in this way is therefore given by 2nd, i.e. a few mm. De Groot reported a simple synthetic wavelength interferometer by using two wavelengths of a multimode laser diode providing a synthetic wavelength of 620 µm [3.8].

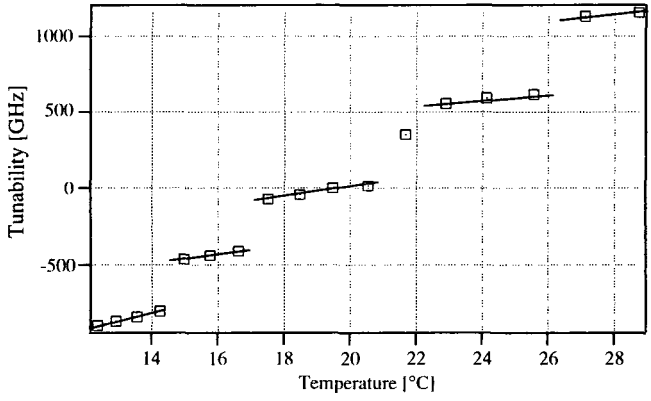

Figure 3.1: Mode-hop characteristic of a AlGaAs diode laser SHARP LT027MD

Standard single-mode AlGaAs diode lasers, such as lasers for CD-players, have often been used for multiple-wavelength interferometry experiments [3.1, 3.9, 3.10, 3.11]. In these lasers, the light is confined in a semiconductor waveguide and the feedback is obtained by cleaving the crystal planes normal to the plane of the junction. They are known as Fabry-Pérot lasers. The linewidth is moderate (typ. 10 MHz) and the frequency tunability with temperature is characterized by mode hops, as shown in Fig. 3.1. These mode hops are mainly due to the temperature induced change of the center of the gain curve (about 0.25 nm/°C). The temperature tuning behavior can vary from device to device. These discontinuities may therefore limit the choice of synthetic wavelengths.

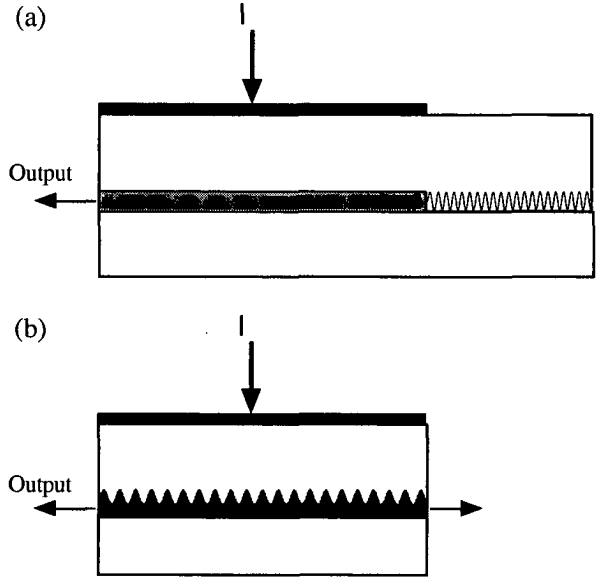

Figure 3.2: a) Distributed Bragg Reflector (DBR) laser diode
b) Distributed FeedBack (DFB) laser diode.

Distributed Bragg Reflector (DBR) diode lasers are devices where at least one of the cleaved facets is replaced by a Bragg grating. The Bragg grating acts as a frequency-selective mirror. In distributed feedback (DFB) diode lasers the grating is manufactured along the active layer and act as a distributed selective reflector. Structures of DBR and DFB lasers are shown in Fig. 3.2. The Bragg grating allows to increase the mode-hop free tuning range, since the tunability is mainly due to the temperature induced change of the refractive index [3.12]. Moreover, the selective mirror leads to high side-mode

suppression (> 25 dB). This allows to reduce substantially the power-independent contribution to the linewidth, which is mainly due to the mode partition noise in standard laser diodes [3.13]. DBR and DFB laser diodes are thus very promising for multiple-wavelength interferometry.

Tunable external cavity diode lasers may also provide a wide mode-hop free tuning range with small linewidth. For instance, a tuning range of at least 10 nm with less than 3 mode-hops can be obtained by using commercially available external cavity diode lasers (New Focus, Velocity Tunable Diode Laser) [3.14]. In addition, the linewidth may be less than 300 kHz. The main drawback is the complexity of the mechanical cavity.

Tunable Nd:YAG lasers may also be of great interest for interferometry. The phase fluctuations and the linewidth of such lasers are smaller than for standard diode lasers [3.15]. The frequency tunability is of about 50 GHz. However, Nd:YAG lasers exhibit poor efficiency since they require optical pumping by means of laser diodes.

In summary, Table 3.1 shows a list of modern tunable laser sources which are suitable to be used in multiple-wavelength interferometry.

Laser types	Standards diode lasers (SHARP)	DBR diode lasers (SDL 5722)	External cavity diode lasers (NewFocus)	Tunable Nd:YAG (Lightwave)
Max. tuning range	1 THz	600 GHz	8 THz	50 GHz
Synthetic wavelength	> 250 µm	> 0.5 mm	> 30 µm	> 6 mm
Mode-hop free tuning range	max. 80 GHz	600 GHz	1 THz	10 GHz
Linewidth	10 MHz	2.5 MHz	300 kHz	5 kHz
Coherence length (calculated)	10 m	40 m	300 m	20 km

Table 3.1: List of modern tunable lasers with their corresponding performance.

3.2 Frequency stabilization of semiconductor lasers

3.2.1 Frequency reference

The absolute accuracy of distance measurement by MWI depends essentially on the properties of the source (coherence, stability, power) and on the calibration of the

synthetic wavelength. Indeed, for highly accurate measurements, that is for $\delta L/L < 10^{-5}$, where L is the working distance and δL the resolution, the synthetic wavelength has to be known with at least the same accuracy. Therefore the laser sources must be stabilized and the synthetic wavelength has to be calibrated. The frequency reference is the key to the accurate frequency stabilization of semiconductor laser diodes. Today many frequency references are available. They mainly use atomic absorption lines or Fabry-Pérot interferometers. Rubidium or Cesium vapor cells are the most commonly used for frequency stabilization at 780 nm and 852 nm respectively.

For multiple-wavelength interferometry, the frequency difference $\Delta\nu$ corresponding to the synthetic wavelength $\Lambda = c/\Delta\nu$ has to be stabilized accurately. Unfortunately, stabilization of the wavelengths on different atomic absorption lines does not allow to choose the synthetic wavelength with a great flexibility. On the other hand, Fabry-Pérot resonators produce an infinite number of resonance frequencies which can be used to stabilize the different lasers. The frequency separation between two consecutive resonances is inversely proportional to the length of the resonator. The frequency difference of the two lasers depends on the number of resonances between the two selected frequencies. Fabry-Pérot resonators provide therefore a broad range of synthetic wavelengths, and are therefore good candidates as frequency reference for multiple-wavelength interferometry.

The transmission of a Fabry-Pérot resonator composed of two planar mirrors, without any loss inside the cavity, is described by

$$T(\nu) = \frac{T_{max}}{1 + (2F/\pi)^2 \sin^2(\pi\nu/FSR)}, \tag{3.1}$$

where T_{max} is the maximal transmission, ν is the optical frequency, F is the finesse of the resonator, and FSR is the free spectral range. For a Fabry-Pérot resonator composed of two mirrors with reflectivities R_1 and R_2 and transmissions T_1 and T_2, one gets

$$T_{max} = T_1 T_2 / \{1 - R\}^2 \text{ and } F = \frac{\pi\sqrt{R}}{1 - R}, \tag{3.2}$$

where $R = \sqrt{R_1 R_2}$. The frequency separation between two consecutive resonances is known as the free spectral range (FSR) of the Fabry-Pérot and is related to the distance d separating both mirrors by

$$FSR = c/2nd, \tag{3.3}$$

where c is the light velocity in vacuum and n is the refractive index of the medium inside the cavity. Figure 3.3 shows the Fabry-Pérot etalon transmission for different finesse F.

As already mentioned, Fabry-Pérot resonators are of great interest in multiple-wavelength interferometry, since the lasers can be stabilized on different resonances in order to generate a stable frequency difference $\Delta\nu$ and therefore a stable synthetic wavelength $\Lambda = c/\Delta\nu$. However its stability may be limited by the thermal expansion of the etalon length. This can be neglected if the resonator is made of super-invar or zerodur material for instance. The length of the Fabry-Pérot resonator may also be locked on a reference laser, e.g. a diode laser which is stabilized on an atomic absorption line [3.3]. In this way, an absolute stabilization of every laser is achieved. This enables to combine multiple-wavelength interferometry with classical interferometry, by using one of these stable optical wavelengths to obtain an absolute distance measurement with submicrometer accuracy.

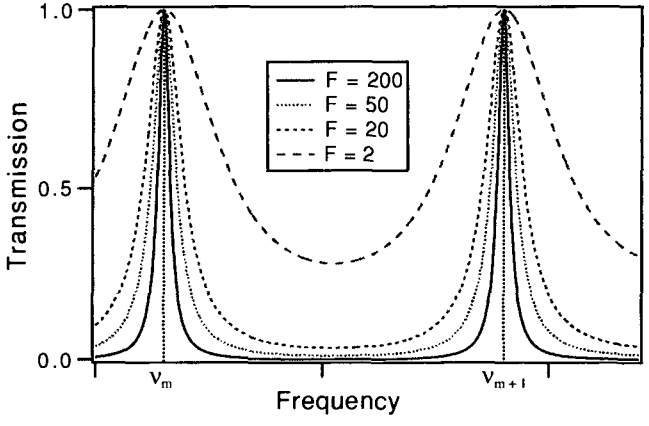

Figure 3.3: Fabry-Pérot transmission vs frequency for different finesse F.

In this work, we will discuss a concept which consists of using an electronic calibration by beat-frequency measurement. This allows to measure indirectly the length of the etalon in real-time. Slow variations of the etalon length can be taken into account for the absolute distance measurement in this way. This concept will be presented in chapter 3.3.

3.2.2 Frequency stabilization principle

A great variety of frequency stabilization schemes exists using Fabry-Pérot interferometers or atomic absorption lines as frequency references. Most of them involve a slight frequency modulation of the lasers [3.16]. As already mentioned, the emitted

frequency of semiconductor lasers depends on the injection current (typically –3.5 GHz/mA for AlGaAs Fabry-Pérot lasers).

The multiple-wavelength source presented in this thesis is based on the stabilization of laser diodes on a common stable Fabry-Pérot resonator. The frequency modulation is obtained by adding a small ac current to the dc injection current. The laser frequency ν_l becomes then

$$\nu_l = \nu_0 + \nu_{FM} \sin(2\pi ft), \tag{3.4}$$

where ν_0 is the average laser frequency, ν_{FM} is the frequency excursion and f is the modulation frequency.

Assuming a monochromatic wave, the transmitted light is given by

$$I_{out}(\nu_l) = I_{in} T(\nu_l) \tag{3.5}$$

where I_{in} is the intensity of the incident beam and $T(\nu_l)$ is the transmission function of the resonator. However, in our experiments we often used resonators with resonance widths of the same order as the linewidth of the source. In this case, the linewidth cannot be neglected and we have to consider the spectral distribution of the source. The transmitted intensity is then given by

$$I_{out}(\nu_l) = I_{in} \int_{-\infty}^{+\infty} d\nu D(\nu - \nu_l) T(\nu), \tag{3.6}$$

where $D(\nu)$ is the lineshape function of the source [3.17]. The lineshape of laser diodes is described to a good approximation by a Lorentzian function

$$D(\nu) = \frac{\Delta\nu/2\pi}{\nu^2 + (\Delta\nu/2)^2}, \tag{3.7}$$

where $\Delta\nu$ is the linewidth, defined here as the full width at half maximum. The transmission $H(\nu)$ of the system is therefore given by the convolution

$$H(\nu) = D(\nu) \otimes T(\nu). \tag{3.8}$$

of the lineshape function with the spectral response $T(\nu)$ of the Fabry-Pérot. For high finesse resonator, the resonance can also be approximated by a Lorentzian function (Eq. (3.1): $\sin^2(\pi\nu/FSR) \approx (\pi\nu/FSR)^2$). The convolution of the two Lorentzian functions is again a Lorentzian. It can be shown that the full width at half its maximum value (FWHM) is given by the sum of the laser linewidth and the resonance width.

By expanding $H(\nu_l)$ in a Taylor serie around the average frequency ν_0, the transmitted intensity becomes to a first-order approximation

$$I_{out}(\nu_l) = I_{in}\left[H(\nu_0) + H'(\nu_0)\nu_{FM}\sin(2\pi ft)\right], \tag{3.9}$$

where $H'(\nu_0)$ is the first derivative of the transmission curve with respect to the laser frequency. Amplitude and sign of the sinusoidal function at the frequency f is thus proportional to the first derivative of the transmission function.

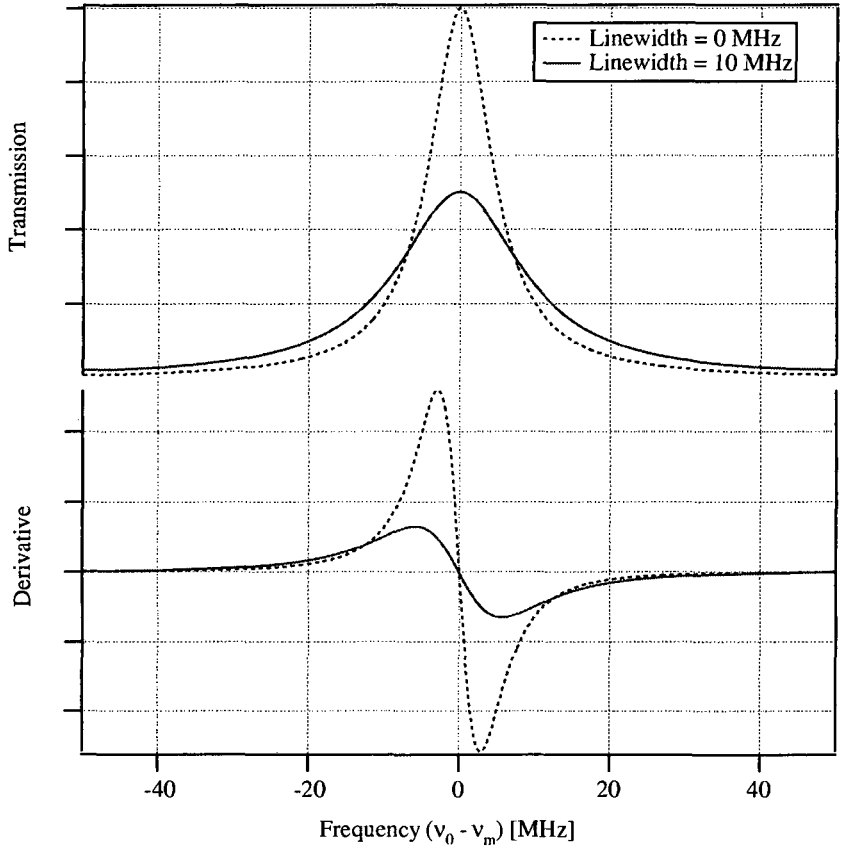

Figure 3.4: Calculated transmission of a Fabry-Pérot around a frequency resonance ν_m (upper part) and its corresponding first derivative (lower part) for a resonance width of 10 MHz and linewidths of 0 MHz (dotted curve) and 10 MHz (plain curve).

Figure 3.4 shows the intensity transmission and its corresponding first derivative for a negligible laser linewidth (dotted curve) and for a laser linewidth equal to the Fabry-Pérot resonance width (plain curve). In both cases, the value of the first derivative goes to zero when ν_0 is equal to the peak frequency ν_m, and changes sign whenever $(\nu_0 - \nu_m)$ changes sign. Therefore, this is a convenient error signal for the feedback loop of frequency stabilization. The slope of the derivative curve at the peak frequency ν_m determines the sensitivity of the frequency demodulator. As shown in Fig. 3.4, the sensitivity depends not only on the Fabry-Pérot resonance width, but also on the laser linewidth.

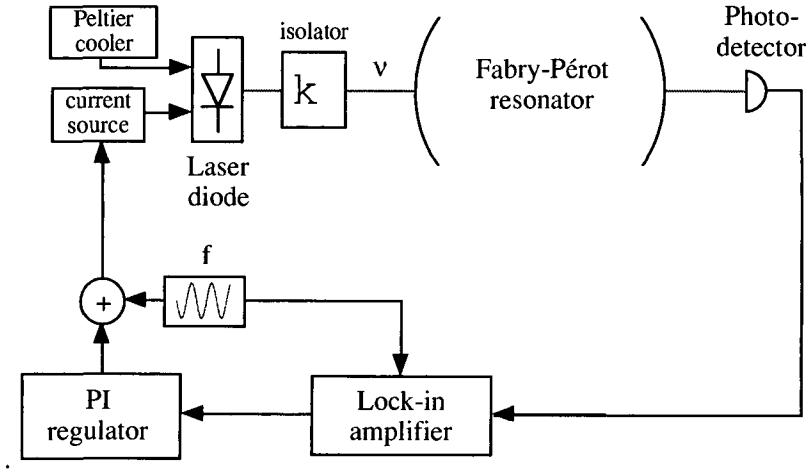

Figure 3.5: Frequency stabilization of a laser diode on a Fabry-Pérot resonator.

The stabilization principle which was used in this work is shown in Fig. 3.5 for one laser diode. The intensity at the output of the frequency reference is synchronously detected at the frequency f in order to obtain an error signal proportional to $H'(\nu_0)$. The error signal is then fed back to the injection current after being processed by an appropriate regulator.

Applications of this stabilization technique to external cavity laser diodes yield very stable laser with narrow linewidths. This may be of great interest for the measurement of large distances. Nielsen and Osmundsen realized frequency stabilization of linewidth-narrowed semiconductor lasers by controlling the phase of the optical feedback from the external cavity by means of a piezoelectric transducer (PZT) [3.18]. The error signal was fed to the PZT via an integrator, whereas higher frequencies of the error signal (beyond 20 Hz) were fed back to the injection current. In this way, they succeeded to get

linewidth reduction from 20 MHz to 300 kHz and a center frequency stability better than 1 kHz.

In multiple-wavelength interferometry, one is interested in stabilizing several lasers on the same frequency reference. For that purpose, the different frequencies can be optically separated at the output of the resonator using a diffraction grating or interference filters and detected individually [3.11]. However, this requires relatively large wavelength differences and thus small synthetic wavelengths (< 1 mm). In this work, we used different modulation frequencies for each laser diode to avoid the optical separation. In this way, the individual regulation of every laser diode is achieved by synchronous detections at the different modulation frequencies (see Fig. 3.6).

3.3 Multiple-wavelength source with electronic calibration [3.1]

As already mentioned, the absolute accuracy of distance measurement using MWI depends essentially on the calibration of the different wavelengths or frequencies. Indeed, the relative accuracy $\delta L/L$ for the measured distance L is given by $\delta L/L = \delta(\Delta\nu)/\Delta\nu$ where $\Delta\nu$ is the frequency difference corresponding to the synthetic wavelength $\Lambda = c/\Delta\nu$.

3.3.1 Principle of operation

Figure 3.6 shows the concept of the novel multiple-wavelength source with absolute calibration by opto-electronic beat-frequency measurement [3.1]. This three-wavelength source consists of three laser diodes, LD_1 to LD_3, operating at the frequencies ν_1, ν_2 and ν_3, respectively. Two of them (LD_1 and LD_2) are stabilized on two consecutive resonances of a common stable Fabry-Pérot resonator (FPR) used as frequency reference.

The superposition of the optical frequencies ν_1 and ν_2 gives rise to a resulting wave with the scalar wavefunction

$$U_{12}(t) = \sqrt{I_1}\exp[i\phi_1(t)]\exp[i2\pi\nu_1 t] + \sqrt{I_2}\exp[i\phi_2(t)]\exp[i2\pi\nu_2 t] \tag{3.10}$$

where I_1, I_2 are the intensities of the individual beam and ϕ_1, ϕ_2 are the corresponding phase fluctuations of the electrical fields. The instantaneous intensity becomes then

$$I_{12}(t) = |U_{12}(t)|^2 = I_1 + I_2 + 2\sqrt{I_1 I_2}\cos[2\pi(\nu_2 - \nu_1)t + \phi_1(t) - \phi_2(t)]. \tag{3.11}$$

The superposition of the two beams gives rise therefore to a beat frequency of $\nu_2 - \nu_1$. In this experiment, we used a confocal Fabry-Pérot resonator with a free spectral range (FSR) of 0.75 GHz, as shown in the bottom part of Fig. 3.6. The beat frequency ν_{21}

resulting from the superposition of the optical frequencies ν_1 and ν_2 can therefore be detected electronically using a high-speed photodetector.

For statistically independent lasers, the phase fluctuations of the beat note $\langle\phi_{12}(t)\rangle^2$ will be given by the addition of the individual phase fluctuations, namely

$$\langle\phi_{12}(t)\rangle^2 = \langle\phi_1(t)\rangle^2 + \langle\phi_2(t)\rangle^2. \tag{3.12}$$

For Lorentzian lineshape functions, it can be shown [3.19] that the corresponding width of the beat note is given by the sum of the two laser linewidths.

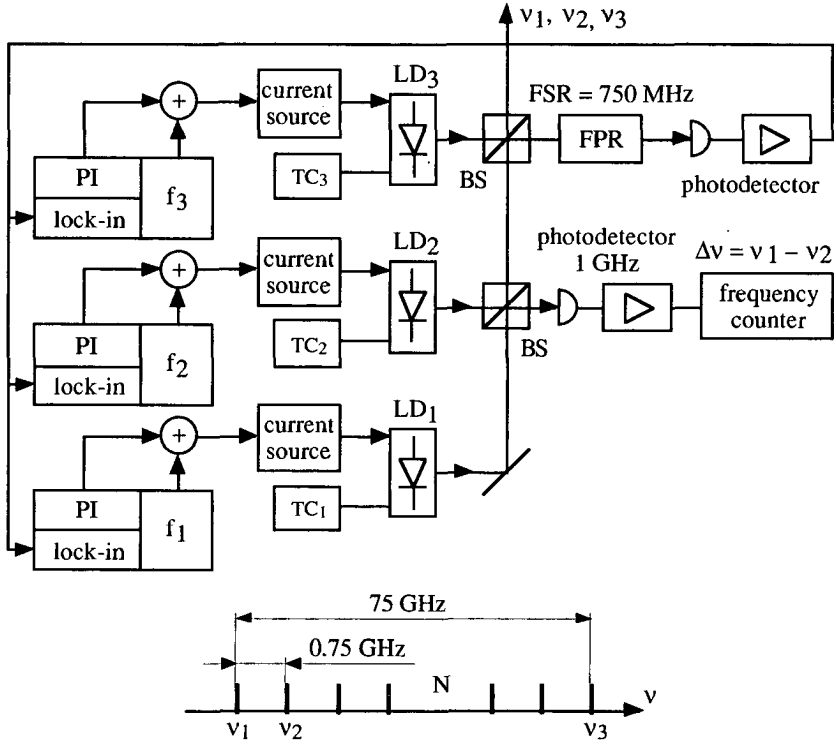

Figure 3.6: Stabilized three-wavelength source calibrated by electronic means.

The beat-frequency of 0.75 GHz is then measured by a frequency counter with electronic accuracy. The third laser diode (LD_3) is tuned continuously from ν_1 to ν_3 over N resonances of the FPR. The frequency difference $\nu_{31} = \nu_3 - \nu_1 = NxFSR$ is then known with the same accuracy as the electronically calibrated beat-frequency ν_{21}. For N = 100, we obtain ν_{31} = 75 GHz ($\Lambda_{31} = c/\nu_{31}$ = 4 mm). Thus, by measuring the beat-frequency ν_{21} and by counting the number of resonances N, an absolute calibration

of the synthetic wavelengths Λ_{21} and Λ_{31} can be achieved. Assuming a fringe interpolation of at least $2\pi/200$ for the synthetic wavelength, it would be possible with such a multiple-wavelength source to measure distances without ambiguity within 200 mm (Λ_{21} = 0.4 m) and with a resolution of 10 µm (Λ_{31} = 4 mm, $2\pi/200$ fringe interpolation [3.10]).

3.3.2 Experiment

Experimental investigations were performed with commercial GaAlAs monomode laser diodes (Sharp LT027MD) emitting at approximately 780 nm with a maximum optical power of 10 mW. The full width at half maximum (FWHM) of the emission linewidth of the laser diodes LD_1 and LD_2 was first determined using the self-heterodyne interferometric technique [3.20]. We measured linewidths of 9 MHz for LD_1 and 8 MHz for LD_2.

The temperature of the diodes is stabilized to better than 0.01 °C by means of Peltier coolers. As shown in Fig. 3.6, a portion of the light from the different lasers is launched into the FPR. The center frequencies of the lasers are brought, by temperature tuning, near a resonance peak of the FPR where the feedback loop is closed. To allow the stabilization of the laser sources, the optical frequency of the diodes is modulated through the injection current at f_1 = 10 kHz, f_2 = 40 kHz and f_3 = 50 kHz. The excursion of the optical frequency is approximately 1 MHz for the three lasers, which is much less than the sum of the laser linewidth (≈ 10 MHz) and the resonance width (7.5 MHz). These frequency modulations are then transformed by the FPR into intensity modulations, which are detected and synchronously demodulated with lock-in amplifiers. An error signal for the feedback loop is thus obtained. Processing of this signal by the PI regulator leads to the voltage which serves as input for the current source.

We detected the beat-frequency ν_{21} using a high-speed photodetector (New Focus 1601) followed by a wide-band amplifier (Hamamatsu C4890). The width of the beat note $\Delta\nu_{21}$ determined from the beat-frequency power spectrum was $\Delta\nu_{21} \cong 18$ MHz (FWHM). This corresponds approximately to the sum of the laser linewidths measured by a self-heterodyne technique. Finally, using a frequency counter (HP 53131), the absolute calibration of the synthetic wavelengths by opto-electronic beat-frequency measurement is achieved.

Frequency stability is commonly evaluated by the Allan deviation [3.21]. For samples y_k obtained with a counter which measures the beat frequency, the Allan deviation is

$$\sigma^2_{Allan}(T) = \left\langle (y_{k+1} - y_k)^2 / 2 \right\rangle_k , \tag{3.13}$$

where T is both the integration time and the sampling time (i.e. there is no dead time between counts).

The results of measurements obtained for different integration times T of the counter are shown in Fig. 3.7. For an integration time of 10 s, the difference frequency $\Delta\nu_{21}$ is therefore calibrated with an accuracy of $\delta\nu_{21}/\nu_{21} = 1.3\text{x}10^{-5}$, and the same accuracy can be expected for $\Delta\nu_{31}$.

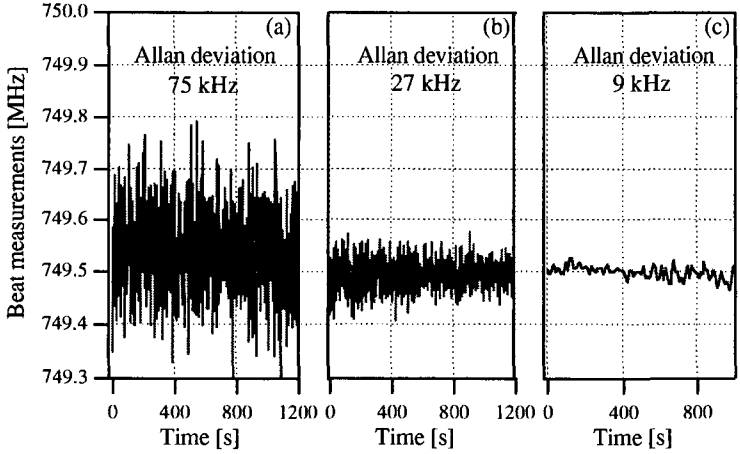

Figure 3.7: Beat frequency measurements for different gate time T of the frequency counter. (a) T = 100 ms, (b) T = 1 s and (c) T = 10 s

3.3.3 Synthetic wavelength calibration

In order to check the accuracy of the synthetic wavelength calibration by beat frequency measurement, we made a calibration of the synthetic wavelength by comparison with a HP-laser interferometer. The optical set-up is depicted in Fig. 3.8. This set-up is similar to a wavemeter. We used ν_1 and ν_3 to illuminate the heterodyne Michelson interferometer. A number of N = 100 resonances of the FPR was counted while tuning the laser diode LD_3 from ν_1 to ν_3. The detection at the output of the two-wavelength interferometer is achieved by a photodiode and a lock-in amplifier to obtain the interference signal by heterodyne detection. For this end, the multiple-wavelength source is followed by a device which creates two orthogonal polarizations of slightly different frequencies. This frequency difference is produced by two acousto-optic modulators operating at F_1 = 40.0 MHz and F_2 = 40.1 MHz. As shown in Fig. 3.8, a polarizing beam splitter directs the optical frequencies $\nu_i + F_i$ (i = 1, 3) toward a reference mirror,

while the optical frequencies $\nu_i + F_2$ go to the target. The output of the interferometer is then detected by a photodiode and a lock-in amplifier, which performs the detection at the heterodyne frequency given by $\Delta F = F_2 - F_1 = 100$ kHz.

The interference fringe function for the synthetic wavelength Λ_{31} is then obtained by detecting the electrical power of the ac part of the photodiode signal (Eq. 2.34). The phase $\Delta\phi_{31}$ of the synthetic wavelength is determined by moving the reference mirror in steps of $\Lambda_{31}/8 = 0.5$ mm to get five 90° phase steps. From the corresponding measured values of the heterodyne signal power, the phase is calculated with a 5-frame error-compensation algorithm. By measuring over a common path difference of about 1 m, using both the MWI and the HP-laser interferometer, a calibrated value of the synthetic wavelength is obtained. From this calibration procedure and taking into account the atmospheric conditions (group index: $n_g = 1.00027127$), we got a synthetic wavelength $\Lambda_{31} = 4.00014 \pm 0.00006$ mm, corresponding to an interpolation accuracy better than $2\pi/100$.

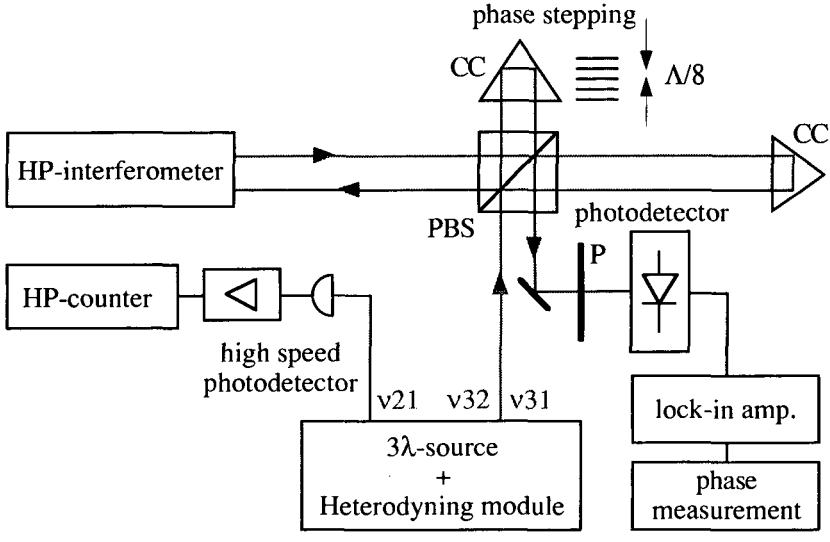

Figure 3.8: Optical set-up used for the calibration of the synthetic wavelength by comparison with a HP-laser interferometer and for the test of distance measurement accuracy

On the other hand, we determined the beat-frequency from ten values obtained with the frequency counter. For a gate time of 10 s, we measured $\nu_{21} = 749.25 \pm 0.01$ MHz. We found with this value a synthetic wavelength $\Lambda_{31} = c/(n_g \nu_{31}) = c/(n_g N \nu_{21})$ of 4.00014 ± 0.00005 mm (in air as above). This result proves that a calibration of the

synthetic wavelength with an accuracy of at least $1.25 \cdot 10^{-5}$ is achieved. The synthetic wavelength Λ_{31} can be chosen anywhere within the tuning range of the laser diode LD_3, which is about 100 GHz, by selecting the number N of resonances of the Fabry-Pérot counted while tuning the laser diode LD_3 from ν_1 to ν_3.

3.3.4 Limitations of the multiple-wavelength source calibration

The measurement accuracy of the beat frequency is mainly limited by the phase or frequency fluctuations of the lasers, as shown from Eq. (3.11). The fluctuations of the measured beat-frequency can be related to the power spectral density of the frequency noise $S_{\delta\nu}(f)$ of the lasers. The frequency stability of a laser, evaluated by the Allan deviation σ_{ν_T}, is related to its frequency noise $S_{\delta\nu}(f)$ by

$$\sigma^2_{\nu_T} = 2\int_0^\infty df\ S_{\delta\nu}(f)\frac{\sin^4(\pi fT)}{(\pi fT)^2}, \tag{3.14}$$

where T is the integration time of the frequency measurements [3.19]. Assuming that the frequency noise $S_{\delta\nu}(f)$ is the same for both lasers, the Allan deviation $\sigma^2_{\Delta\nu_T}$ of the beat frequency is then given by $\sigma^2_{\Delta\nu_T} = 2\sigma^2_{\nu_T}$.

For a laser diode under free-running condition, the frequency noise spectrum has two components: a white noise and a flicker (1/f) noise. Therefore, it can be expressed as $S_{\delta\nu}(f) = C_1/f + C_0$. Assuming that the emission linewidth $\Delta\nu$ is mainly caused by the white noise part of $S_{\delta\nu}(f)$, the value for C_0 is approximately given by $C_0 = \Delta\nu/\pi$, i.e. about 2.7×10^6 Hz^2/Hz in our case. We can note that the flicker noise is divergent for $f \cong 0$. However, $S_{\delta\nu}(f)$ is reduced for low frequencies by the electronic feedback loop.

As long as the regulator does not introduce additional noise, the frequency noise spectrum with electronic feedback is given by

$$S_{\partial\nu}(f)\Big|_{\text{with feedback}} = \frac{1}{|1+H(f)|^2} S_{\partial\nu}(f)\Big|_{\text{free-running}}, \tag{3.15}$$

where H(f) is the transfer function of the loop [3.22]. The power spectrum of the remaining error signal was measured in order to determine the power spectral density of the frequency noise with the stabilization loop closed. The result is shown in Fig. 3.9. The maximum values are found between 1 Hz and 10 Hz and they are slightly above 10^9 Hz^2/Hz, which is much greater than the expected C_0 of 2.7×10^6 Hz^2/Hz. Using Eq. (3.14) and Fig. 3.9, we get Allan deviations for the beat-frequency of 100 kHz and 29 kHz for integration times T of 0.1 s and 1 s, respectively. These values correspond very well with those obtained from direct measurements of the beat note, namely 75 kHz and

27 kHz as shown in Fig. 3.7. For T = 10 s, one would expect from Fig. 3.9 an Allan deviation which is smaller than the measured 9 kHz (see Fig. 3.7). However, there are probably other noise sources, e.g. mechanical noise in the optical set-up.

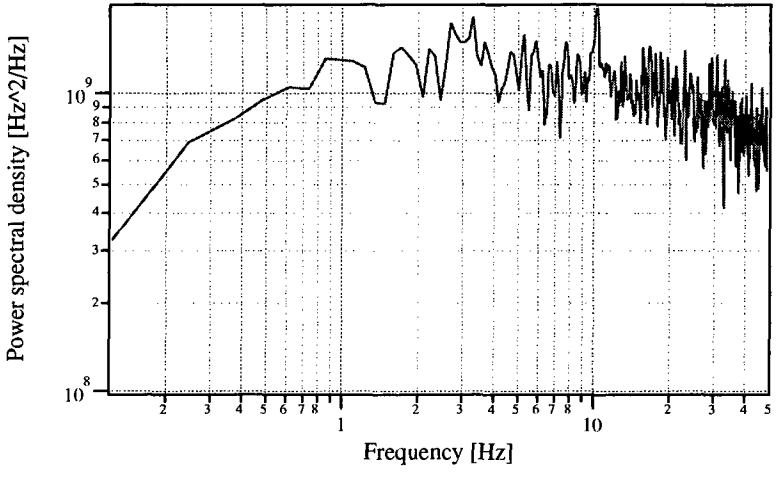

Figure 3.9: Measured power spectral density of the frequency noise of the laser diodes when the feedback loop is closed.

3.4 High-power multiple-wavelength source.

As it will be discussed in chapter 5, absolute distance measurement can be performed on rough surfaces by means of multiple-wavelength interferometry. The problems with non-cooperative targets (rough surfaces) are: statistical properties of returning light (speckles) and low coherent power (scattered light, speckles) [3.23]. The multiple-wavelength source which is described above is composed of low optical power diode lasers (i.e. about 7 mW). Only a few mW optical power is available to illuminate the diffusing target. For distance measurements beyond 1 m, the received coherent power on the detector would not be enough for measurements with reasonable response time.

There are different possibilities to increase the source power. Two solutions have been studied.

3.4.1 Semiconductor optical amplifier.

The first one consists of using a semiconductor optical amplifier after the low power source. For this task, we used a tapered amplifier chip for 785 nm (SDL 8630). The

geometry of this device is shown in Fig. 3.10. The tapered design allows a high efficiency and a near-diffraction limited output beam [3.24]. For a few mW of input power, we obtained an output power of about 100 mW for each wavelength, corresponding to a gain of about 100. In this MOPA (master oscillator power amplifier) configuration, the spectral characteristics are only determined by the low-power diode lasers.

In this way, the multiple-wavelength source is composed of only one high-power device. This is of great importance in order to get a low-cost measuring system. The main drawback is the high optical isolation (> 70 dB) which is required between the low-power source and the optical amplifier because of the feedback sensitivity of diode lasers.

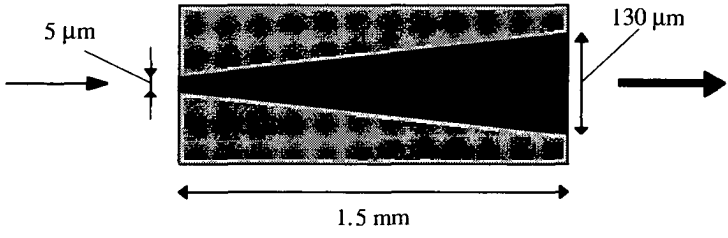

Figure 3.10: Tapered amplifier chip used in the SDL 8630 system.

3.4.2 High-power DBR laser diodes.

The second solution consists of using directly high-power distributed Bragg reflectors laser diodes (SDL-5722H) emitting at approximately 850 nm. The maximal output power is of about 150 mW. A multiple-wavelength source similar to the low-power source described in chapter 3.3 was mounted with such diode lasers. The frequency tunability with temperature is mode-hop free over at least 1.5 nm (620 GHz), as shown in Fig. 3.11. This allows to choose the most appropriate synthetic wavelength with a great flexibility between 0.5 mm and 200 mm, depending on the number of Fabry-Pérot resonances between the two frequencies. Moreover, as shown in Fig. 3.12, the linewidth measured from the beat note spectrum is only 2.5 MHz, which corresponds to a coherence length of about 40 m, which is 4 times longer than for the standard low power laser diodes.

In addition to the high optical power, this solution provides a multiple-wavelength source with better spectral characteristics compared to the low-power source. This is a substantial advantage for multiple-wavelength interferometry. However, at least two

expensive high-power DBR lasers are required. The solution is therefore more expensive than the semiconductor amplifier.

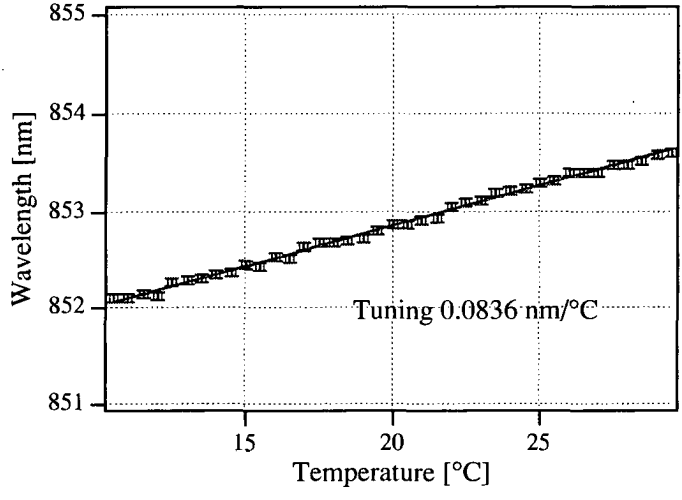

Figure 3.11: Wavelength tuning with temperature for DBR diode lasers SDL 5722

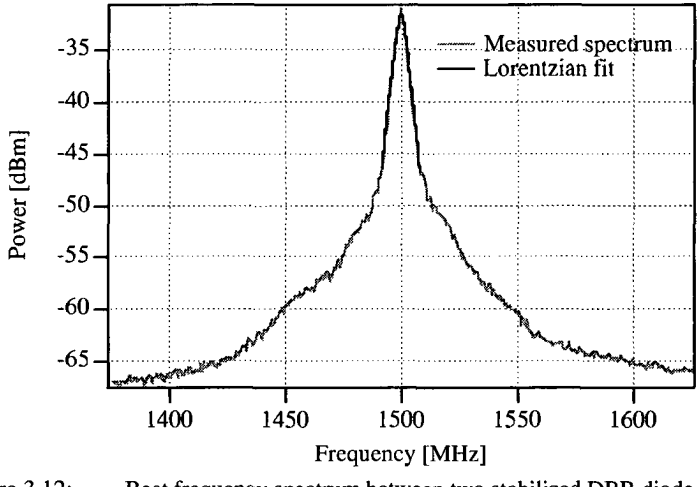

Figure 3.12: Beat frequency spectrum between two stabilized DBR diode lasers.

3.5 Fiber-optic Fabry-Pérot resonator

For industrial applications, a portable measuring set-up is required. Diode lasers help to obtain a compact system. However, the confocal optical resonator which was used for the experiments described in chapter 3.3 should be replaced by a more compact frequency reference. Moreover, some beamsplitters and mirrors could also be replaced by a fiber network. In order to obtain a compact all-fiber system we investigated different solutions to replace the bulky confocal resonator by a fiber-optic resonator. We will describe in this chapter two types of fiber-optic Fabry-Pérot resonators.

3.5.1 Fiber Fabry-Pérot resonator using Bragg grating reflectors

Fiber Bragg gratings are often used as filters for fiber-optic telecommunications. Moreover, they have many applications as sensors for strain and temperature measurements [3.25]. Fiber Bragg gratings are written into the core of a germania doped single-mode fiber by photoinduced refractive-index changes. This allows to use the grating as a frequency-selective mirror. By writing two identical Bragg gratings at different location in the same optical fiber, we can thus achieve a Fabry-Pérot effect if both gratings are reflective at the wavelength of the laser source. Fabry-Pérot interferometers composed of fiber Bragg gratings has been reported by Morey et al. [3.26]. They achieved a very high-finesse (> 600) for a FSR (free spectral range) of about 10.6 GHz. Fabry-Pérot resonators composed of fiber Bragg gratings would allow an all-fiber etalon without any pigtailing at relatively low-cost. The principle of a fiber Bragg grating is similar to a dielectric mirror. The reflectivity is achieved by stacks of $\lambda/4$ layers with two different refractive indexes. However, contrary to dielectric mirrors, the refractive index modulation is very small in fiber Bragg gratings. Therefore, long gratings are required to achieve high reflectivities. For that reason, fiber Bragg gratings are more dispersive than dielectric mirrors. A resonator composed of Bragg gratings and the standard Fabry-Pérot resonator may therefore exhibit different behavior.

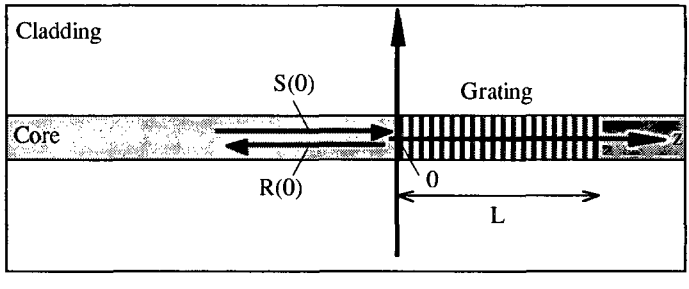

Figure 3.13: Intra-core fiber Bragg grating.

Figure 3.13 shows an intra-core grating structure of length L. Assuming a sinusoidal index modulation with a spatial period Λ_G, the refractive index along the grating is

$$n(z) = n_{eff} + \Delta n \sin(2\pi z/\Lambda_G), \tag{3.16}$$

where n_{eff} is the effective refractive index and Δn is the amplitude of the phase grating.

The maximal reflection occurs when the Bragg condition

$$\Delta k = \frac{2\pi}{\Lambda_G} - k_R - k_S = 0 \tag{3.17}$$

is fulfilled, where k_R and k_S are the wave numbers of the backward- and forward-travelling waves, respectively. The wavelength λ_B at which the grating reflectivity is maximal is therefore

$$\lambda_B = 2n_{eff}\Lambda_G. \tag{3.18}$$

For frequencies ν different from $\nu_B = c/\lambda_B$, the phase mismatch Δk can be expressed as

$$\Delta k = \frac{4\pi}{c} n_{eff}(\nu_B - \nu). \tag{3.19}$$

The complex amplitudes R(z) and S(z) of the backward- and forward-traveling waves can be derived from the well-known coupled-mode equations [3.27]

$$\begin{aligned} \frac{dR(z)}{dz} &= -i\kappa(z)S(z)\exp(-i\Delta kz) \\ \frac{dS(z)}{dz} &= i\kappa(z)R(z)\exp(+i\Delta kz) \end{aligned} \tag{3.20}$$

where $\kappa(z)$ is the coupling coefficient. We assume that the coupling occurs between $z = 0$ and $z = L$, so that $\kappa(z)$ vanishes elsewhere. Assuming that all the light intensity is located in the fiber core, the coupling coefficient is given by [3.28]

$$\kappa = \frac{\pi\Delta n}{\lambda_B}, \quad \text{for } 0 \le z \le L. \tag{3.21}$$

Using Eqs. (3.20) and the boundary conditions $S(0) = S_0$ and $R(L) = 0$, we get for the reflection coefficient of the complex amplitude

$$r = i\kappa \frac{\exp(\kappa\rho L) - \exp(-\kappa\rho L)}{\gamma_2 \exp(\kappa\rho L) - \gamma_1 \exp(-\kappa\rho L)} \tag{3.22}$$

where $\rho = \sqrt{1-(\Delta k/2\kappa)^2}$, $\gamma_1 = -i\Delta k/2 + \kappa\rho$ and $\gamma_2 = -i\Delta k/2 - \kappa\rho$.

The phase of the complex reflection coefficient is [3.29]

$$\phi_r = \arctan\left[\frac{2\kappa\rho}{\Delta k}\coth(\kappa\rho L)\right]. \tag{3.23}$$

The group delay t_D is given by

$$t_D = \frac{d\phi_r}{d\omega}, \tag{3.24}$$

where $\omega = 2\pi\nu$. We can introduce a path length

$$L_G = ct_D/n_{eff} \tag{3.25}$$

in the grating which corresponds to the group delay t_D. This length L_G can therefore be considered as the additional path traveled by the light in the grating due to the phase dispersion. Using Eqs. (3.23), (3.24) and (3.25), we get

$$L_G = \frac{L - 2\frac{\kappa}{\rho\cdot\Delta k^2}\sinh(2\kappa\rho L)}{1 - 4\frac{\kappa^2}{\Delta k^2}\cosh^2(\kappa\rho L)} \tag{3.26}$$

as a function of the phase mismatch Δk. Assuming a Fabry-Pérot resonator composed of two identical Bragg gratings, as shown in Fig. 3.14, the corresponding free spectral range becomes then

$$FSR = \frac{c}{2n_{eff}(d + L_G)}, \tag{3.27}$$

where d is the cavity length between the two gratings. It is important to note that FSR depends on the phase mismatch Δk. Therefore, the frequency separation between two consecutive resonances will not remain constant over the bandwidth of the grating because of the dispersion of the grating.

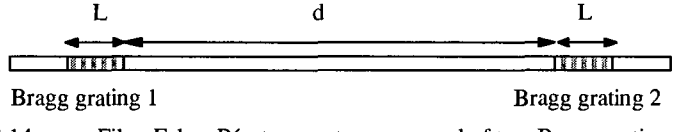

Figure 3.14: Fiber Fabry-Pérot resonator composed of two Bragg gratings.

Experimental results were obtained by using a Fabry-Pérot resonator with Bragg gratings commercially available from 3M. We measured a center wavelength of about

787 nm, a bandwidth of about 0.5 nm, corresponding to a frequency range of about 240 GHz, and a reflectivity of about 95% for both gratings. The cavity length between the two reflectors was about 13 cm. Figure 3.15 shows the transmission of the resonator which was measured by tuning the optical frequency of the laser diode. The measured finesse was about F = 20.

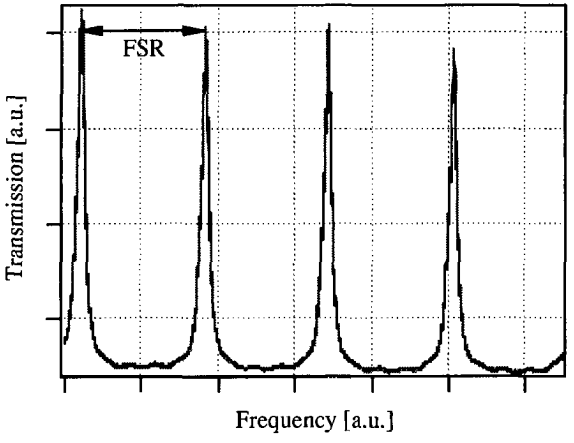

Figure 3.15: Measured transmission spectrum of the fiber Fabry-Pérot with Bragg grating reflectors.

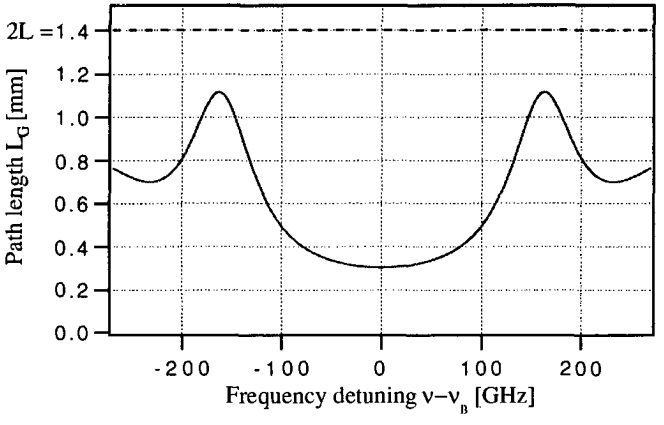

Figure 3.16: Equivalent path length L_G of the light in the grating for L = 700 µm and $\Delta n = 10^{-3}$.

We estimated the grating length to be about L = 700 μm and the index variation to be about $\Delta n = 8 \times 10^{-4}$, so that the calculated bandwidth and the maximal reflection match the measured values. We computed then the equivalent path length in the grating as a function of the frequency detuning $\nu - \nu_B$ using Eq. (3.26). The corresponding relative variations of the free spectral range over 80 GHz were also calculated. Results are shown in Fig. 3.16 and Fig. 3.17. The principle of the multiple-wavelength source described above requires a relative variation of the free spectral range which is smaller than 10^{-5} over a bandwidth of 75 GHz in order to achieve the reported accuracy. As shown in Fig. 3.17, this condition is not fulfilled and therefore the resonator is not suitable for the multiple-wavelength source described above.

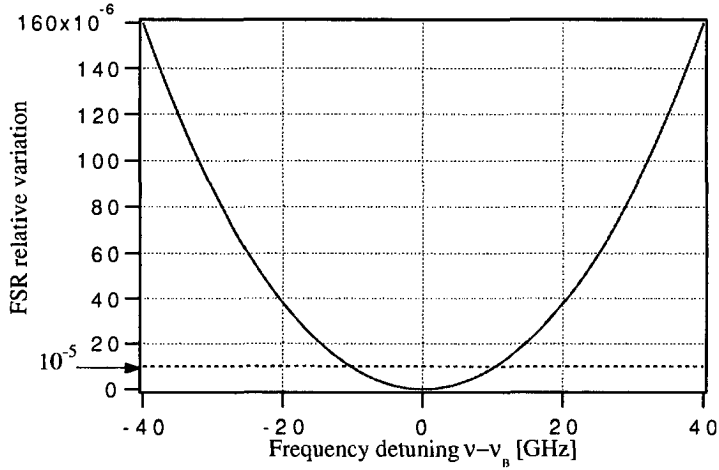

Figure 3.17: Relative variation of the free spectral range for L = 700 μm, $\Delta n = 10^{-3}$ and d = 13 cm.

Experimental investigations were performed by using two laser diodes stabilized on two consecutive resonances. Similarly to the concept described in Fig. 3.6, we measured the corresponding beat frequency for three different values of $(\nu - \nu_B)$, obtained by tuning the laser frequencies over about 40 GHz. As shown in Fig. 3.18, the mean values of the beat frequency measurements are different depending on the frequency detuning. The maximal difference between measurements is about 0.6 MHz, corresponding to a relative FSR variation of 7×10^{-4}. The variations are therefore four times larger than the values predicted by Fig. 3.17. However, we should take into account that the center frequencies of the two Bragg gratings were not identical. A difference of about 80 GHz was measured. For one of the gratings, the detuning frequency $(\nu - \nu_B)$ was therefore rather between 80 GHz to 120 GHz than between 0 GHz to 40 GHz during our

measurements. As shown in Fig. 3.16, the path length variation in this frequency detuning range is larger than at the center of the curve, which may explain the larger FSR variations measured for our Fabry-Pérot resonator.

Lower dispersion values could be obtained by using larger grating bandwidths. Large bandwidths with high reflectivities could be achieved by manufacturing shorter gratings with higher index variation Δn. Unfortunately, higher index variations are not easy to achieve and therefore the reflectivity of shorter gratings may be smaller. As a result, the finesse of the Fabry-Pérot may be too low to stabilize accurately the frequency of the laser diodes. In addition, it should be noted that this analysis does not take into account grating nonuniformities, which may occur due to saturation effects [3.26]. As a result, the Bragg wavelength may vary along the grating. This may introduce a strong additional dispersion, since one can define for each position along the grating a local Bragg wavelength [3.30]. Therefore, resonators composed of fiber Bragg gratings are unfortunately not good candidates as frequency reference for the stabilization and calibration of synthetic wavelengths.

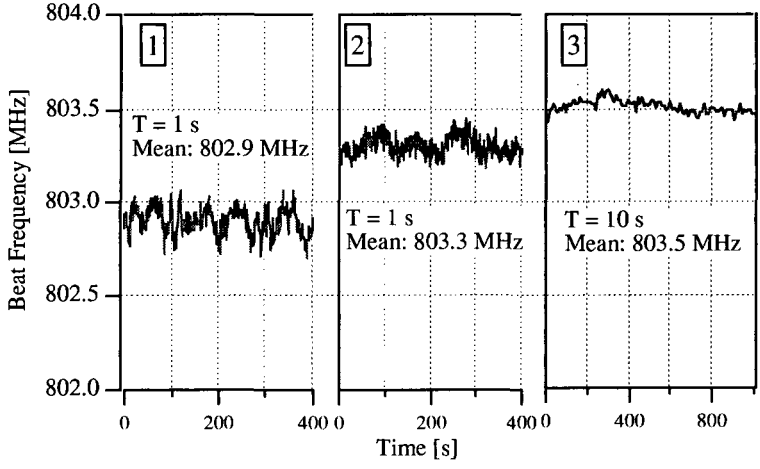

Figure 3.18: Beat frequency measurements for different frequency detuning ($\nu - \nu_B$), obtained by tuning the laser frequencies over about 40 GHz.

3.5.2 Fiber Fabry-Pérot resonator with dielectric mirrors

Fiber optic Fabry-Pérot resonators are also fabricated by depositing directly two highly reflective multilayer mirrors onto each end of an optical fiber. A fiber Fabry-Pérot scanning interferometer is shown in Fig. 3.19. This device is commercially available from Micron Optics, Inc. Since the fiber is birefringent, a polarization controller should be used to match the input light with one of the two polarization eigenmodes of the resonator.

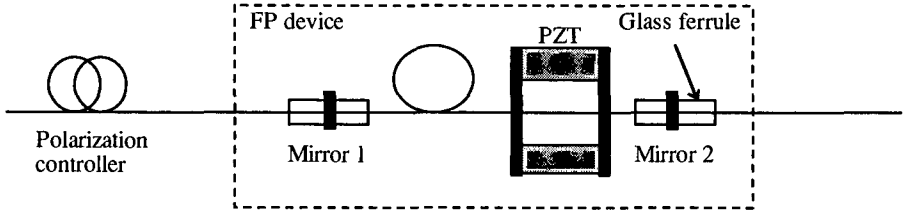

Figure 3.19: Fiber Fabry-Pérot etalon composed of highly reflective mirrors (Micron Optics, Inc).

The piezo-electric transducer allows to scan the length of the Fabry-Pérot cavity by axially straining a short section of the fiber. In addition, it enables to lock the Fabry-Pérot etalon to a stabilized reference laser if necessary. This may be of interest for applications which require absolute stabilization of the lasers. Strong thermal variations of the fiber are compensated in this way. However, this function was not used in our experiment, since the real-time calibration of the source by electronic beat frequency measurements (see chapter 3.3) allows to take into account these slow thermal variations. In addition, the thermal expansion of the silica fiber is low (about 6×10^{-6} /°C).

The length of the Fabry-Pérot cavity is about 15 cm, corresponding to a free spectral range FSR of 700 MHz. A finesse of 200 was specified by the manufacturer, corresponding to a resonance width of about 3.5 MHz. The fiber resonator was first tested by using a DBR diode laser (SDL5722) as light source. Figure 3.20 shows the transmission obtained by scanning the fiber Fabry-Pérot length by means of the piezo transducer. The resonance width is slightly broadened because of the linewidth of the laser which is about 2.5 MHz. Indeed, we measured a width of 6 ± 1 MHz, corresponding to the sum of the Fabry-Pérot resonance width and the laser linewidth.

The resonances which are due to the orthogonal polarization eigenmode have been substantially decreased by optimizing the polarization controller.

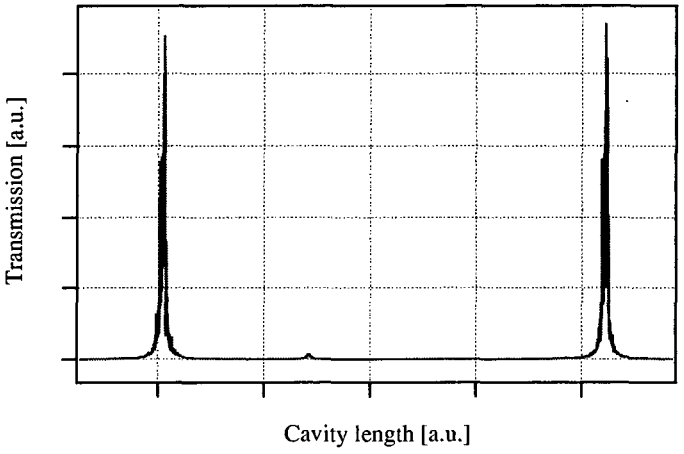

Figure 3.20: Measured transmission of the scanning Fabry-Pérot interferometer.

Two DBR diode lasers and the fiber Fabry-Pérot etalon were used to realize a two-wavelength source with calibration by beat-frequency measurements which is similar to the source shown in Fig. 3.6. During the calibration procedure, both diode lasers are stabilized with a frequency difference of two resonances, as described in Fig. 3.21.

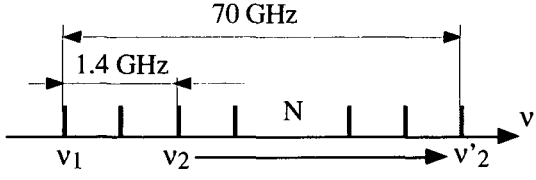

Figure 3.21: Two-wavelength source stabilized on a fiber Fabry-Pérot etalon.

The beat-frequency $\nu_2 - \nu_1$ was measured by means of a high-speed photodetector (Newport AD-300AC) and a frequency counter (HP 53131A). Results are shown in Fig. 3.22 for an integration time of 10 s. The frequency difference $\Delta\nu_{21}$ is therefore calibrated with an accuracy of $\delta\nu_{21}/\nu_{21} = 5\text{x}10^{-6}$. Note that the beat frequency remained stable over more than 20 minutes, showing a high stability of the resonator length.

After the calibration procedure, the second diode laser can be tuned from ν_2 to ν'_2 over N resonances, as shown in Fig. 3.21. A larger frequency difference is generated in this way, corresponding to a smaller synthetic wavelength. The synthetic wavelength can be

chosen anywhere within the tuning range of the DBR laser diode, which is about 600 GHz, by selecting the number N of resonances of the Fabry-Pérot counted while tuning the laser diode from ν_2 to ν'_2. In our experiment, we tuned the frequency over 98 resonances in order to generate a frequency difference of 70 GHz, corresponding to a synthetic wavelength of 4.3 mm. The same calibration accuracy is expected for $\nu_2'-\nu_1$, since the cavity length should remain stable during the tuning time (a few seconds). However, the calibration procedure should be repeated every twenty minutes to overcome the problem of ambient temperature variations. This concept allows to use two diode lasers instead of the three lasers described in chapter 3.3, and therefore the cost of the system will be reduced.

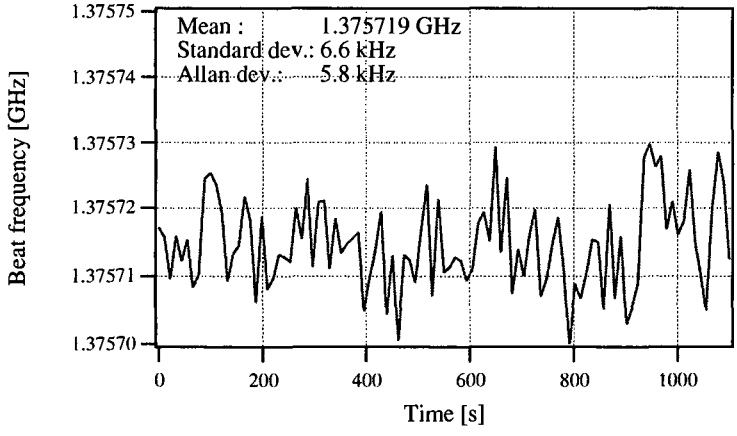

Figure 3.22: Beat frequency measurements for an integration time of 10 s.

3.6 Conclusions

Highly accurate distance measurements by MWI require sources with a high stability as well as a highly accurate calibration. In this chapter, a new concept of multiple-wavelength source has been presented which consists of three diode lasers stabilized on a common Fabry-Pérot etalon. Fast and accurate calibration of the synthetic wavelength is achieved by beat-frequency measurement. An accuracy better than 10^{-5} has been obtained.

The performance of the source was substantially improved by using high-power DBR diode lasers. Their wide mode-hop free tunability allows to choose the most appropriate synthetic wavelength with a great flexibility between 0.5 mm and a few 10 cm, depending on the number of Fabry-Pérot resonances between both frequencies. Furthermore, the coherence length of the DBR lasers is 40 m instead of the 10 m for the

initially used low power laser diodes. In addition, the higher power of the source (> 100 mW) is of advantage for the measurement on scattering surfaces.

A more compact source is a key element for industrial applications. For that purpose we demonstrated that a fiber-optic frequency reference can be used instead of a bulky confocal Fabry-Pérot etalon. The potential of miniaturization of the multiple-wavelength source is thus increased.

As a final result, we demonstrated that a compact and powerful multiple-wavelength source can be achieved with modern technologies.

References

[3.1] E. Zimmermann, Y. Salvadé and R. Dändliker, "Stabilized three-wavelength source calibrated by electronic means for high-accuracy absolute distance measurement", *Opt. Lett.* **21** (7), 531-533 (1995).

[3.2] G. L. Bourdet and A. G. Orszag, "Absolute distance measurements by C02 laser multiwavelength interferometry", *Appl. Opt.* **18** (2), 225-227 (1979).

[3.3] R. Dändliker, K. Hug, J. Politch and E. Zimmermann, "High-accuracy distance measurements by multiple-wavelength interferometry", *Opt. Eng.* **34** (8), 2407-2412 (1995).

[3.4] R. Dändliker, "Distance measurements with multiple wavelength techniques", *2nd Internat. Workshop on High Precision Navigation*, ed. K. Linkwitz, U. Hangleiter, (Ferd. Dümmlers Verlag, Bonn, 1992), p. 159-170.

[3.5] R. Dändliker, R. Thalmann and D. Prongué, "Two-wavelength laser interferometry using superheterodyne detection", *Opt. Lett.* **13**, 339-341 (1988).

[3.6] H. Matsumoto, "Infrared He-Xe laser interferometry for measuring length", *Appl. Opt.* **20** (2), 231-234 (1981).

[3.7] A. F. Fercher, H. Z. Hu and U. Vry, "Rough surface interferometry with a two-wavelength heterodyne speckle interferometer", *Appl. Opt.* **24**, 2181-2188 (1985).

[3.8] P. de Groot, "Interferometric laser profilometer for rough surfaces", *Opt. Lett.* **16** (6), 357-359 (1991).

[3.9] Z. Sodnik, E. Fischer, T. Ittner and H. J. Tiziani, "Two-wavelength double interferometry using a matched grating technique", *Appl. Opt.* **30**, 3139-3144 (1991).

[3.10] R. Dändliker, Y. Salvadé and E. Zimmermann, "Distance measurement by multiple-wavelength interferometry", *J. Opt.* **29** (3), 105-114 (1998).

[3.11] P. de Groot and S. Kishner, "Synthetic wavelength stabilization for two-color laser diode interferometry", *Appl. Opt.* **30** (28), 4026-4033 (1991).

[3.12] D. Hofstetter in *Monolithically integrated interferometer for optical displacement measurement* (PhD thesis, University of Neuchâtel, 1996) chap. 5.

[3.13] K. Petermann in *Laser diode modulation and noise* (Kluwer Academic Publishers, Dordrecht, 1988)

[3.14] T. Day, M. Brownell and I.-F. Wu, "Widely Tunable External Cavity Diode Lasers", *Proc. SPIE* **2378**, 35-41 (1995).

[3.15] K. H. Bechstein and W. Fuchs, "Absolute interferometric distance measurements applying a variable synthetic wavelength", *J. Opt.* **29** (3), 179-182 (1998).

[3.16] Y. C. Chung and T. M. Shay, "Frequency stabilization of a diode laser to a Fabry-Pérot interferometer", *Opt. Eng.***27** (5), 424-426 (1988).

[3.17] G. Hernandez in *Fabry-Perot Interferometers* (Cambridge University Press, London, 1986)

[3.18] C. J. Nielsen and J. H. Osmunden, "New approach towards frequency stabilization of linewidth-narrowed semiconductor lasers", *Electron. Lett.* **19**, 644-646 (1983).

[3.19] T. Ikegami, S. Sudo and Y. Skai in *Frequency stabilization of semiconductor laser diode* (Artech House Publishers, london, 1995) chap 3.

[3.20] T. Okoshi, K. Kikuchi and A Nakayama,"Novel method for high resolution measurement of laser output spectrum", *Electron. Lett.* **16**, 630-631 (1980).

[3.21] D. W. Allan, "Statistics of Atomic Frequency Standards", *Proc IEEE* **54** (2), 221-230 (1966).

[3.22] K. Petermann in *Laser diode modulation and noise* (Kluwer Academic Publishers, Dordrecht, 1988) 294.

[3.23] R. Dändliker, M. Geiser, C. Giunti, S. Zatti, G. Margheri, "Improvement of speckle statistics in double-wavelength superheterodyne interferometry", *Appl. Opt.* **34**, 7197 (1995).

[3.24] D. Mehuys, D. F. Welch and L. Goldberg, "2.0 W cw, diffraction-limited tapered amplifier with diode injection", *Electron. Lett.* **28**, 1944-1946 (1992).

[3.25] W. W. Morey, G. Meltz, and W. H. Glenn, "Fibre optic Bragg grating sensors", *Proc SPIE* **1169**, 98-107 (1989).

[3.26] W. W. Morey, G. A. Ball and G. Meltz, "Photoinduced Bragg gratings in optical fibers", *Optic & Photonics News*, February 1994, 6-14.

[3.27] A. W. Snyder, "Coupled-Mode Theory for Optical Fibers", *J. Opt. Soc. Am.* **62**, 1267-1277 (1972).

[3.28] D. K. W. Lam and B. K. Garside, "Characterization of single-mode optical fiber filters", *Appl. Opt.* **20** (3), 440-445 (1981).

[3.29] D. K. W. Lam, B. K. Garside and K. O. Hill, "Dispersion cancellation using optical-fiber filters", *Opt. Lett.* **7** (6), 291-293 (1982).

[3.30] J. E. Sipe, L. Poladian and C. Martijn de Sterke, "Propagation through nonuniform grating structures", *J. Opt. Soc. Am. A* **11** (4), 1307-1320 (1994).

Chapter 4

Heterodyne techniques for multiple-wavelength interferometry

Application of heterodyne detection to multiple-wavelength interferometry can produce signals which are directly sensitive to the synthetic wavelength. This is a considerable advantage, since the interferometric stability at the optical wavelength is not any more required. The basic concepts of this detection technique have already been discussed in chapter 2.4.

In this chapter, applications of this detection technique to multiple-wavelength interferometry will be considered in detail. In the first section, the optical set-up previously used for superheterodyne detection will be presented [4.1, 4.2], since we used a similar heterodyne technique in this work.

The different optical set-ups which were used in this work will then be described. Results obtained on cooperative targets (retroreflector, mirror) by means of the different techniques will also be presented.

Specially, we will emphasize in this chapter the two dimensional measurements with modern CCD technologies, for the application of multiple-wavelength interferometry to non-cooperative targets (rough surfaces).

4.1 Superheterodyne detection

Superheterodyne detection, introduced by Dändliker et al. [4.1, 4.2], enables high-resolution measurements at arbitrary synthetic wavelengths Λ without the need for interferometric stability at the optical wavelengths λ_1 and λ_2 or separation of these wavelengths optically.

Figure 4.1 shows a typical set-up of a two-wavelength interferometer with superheterodyne detection. Each source is followed by a device which creates two orthogonal polarizations of slightly different frequencies. These frequency differences can be produced by acousto-optical modulators and are typically $f_1 = 40.0$ MHz and $f_2 = 40.1$ MHz. Both sources are then used to illuminate a polarizing Michelson-type interferometer. Two photodetectors behind appropriate polarizers produce reference and interferometer signals $I_r(t)$ and $I_s(t)$ of the form

$$I(t) = A_0 + A_1 \cos(2\pi f_1 t + \Delta\phi_1) + A_2 \cos(2\pi f_2 t + \Delta\phi_2), \quad (4.1)$$

where $\Delta\phi_1 = 4\pi L/\lambda_1$ and $\Delta\phi_2 = 4\pi L/\lambda_2$. Both signals are fed to a quadratic detector to access directly to the phase difference $\Delta\phi_1 - \Delta\phi_2 = 4\pi L/\Lambda$. Indeed, by performing an amplitude demodulation (rectification and low-pass filtering) one gets a signal of frequency $f_1 - f_2$ and phase $\Delta\phi_1 - \Delta\phi_2$ (see Eq. (2.32)). The phase difference between the two amplitude-demodulated signals is then measured by means of a phasemeter in order to obtain $\Delta\phi_1 - \Delta\phi_2$.

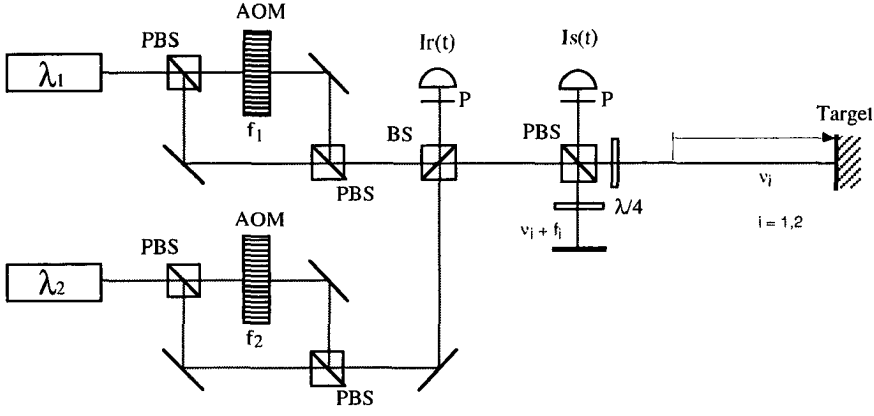

Figure 4.1: Two-wavelength superheterodyne interferometer set-up. P: polarizers; BS:beam splitters; PBS: polarizing beam splitters; λ/4: quarter-wave plate; AOM: acousto-optical modulators.

Successful application of superheterodyne detection has been reported for multiple-wavelength interferometry with different types of sources, namely two detuned single frequency Ar lasers (Λ = 60 mm) [4.1], diode laser and acousto-optic modulator for a 500 MHz frequency shift (Λ = 0.6 m) [4.3, 4.4], two-wavelength HeNe laser (Λ = 55.5 μm) [4.5], tunable Nd:YAG lasers (Λ > 6 mm) [4.6, 4.7, 4.8].

4.2 Three-wavelength heterodyne interferometer

As already discussed in chapter 2.4, simpler detection methods, which do not need separate modulation of the two wavelengths, might be of interest. In this work, a three-wavelength interferometer based on this simpler detection technique was realized for absolute distance measurements up to 200 mm [4.9].

The set-up of the three-wavelength heterodyne interferometer is shown in Fig. 4.2. As light source, we used the calibrated multiple-wavelength source described in chapter 3.3.

The source is then followed by a device which creates two orthogonal polarizations of slightly different frequencies. This frequency difference is produced by two acousto-optic modulators operating at $F_1 = 40.0$ MHz and $F_2 = 40.1$ MHz. A polarizing beam splitter directs the optical frequencies $\nu_i + F_1$ (i = 1...3) toward a reference mirror, while the optical frequencies $\nu_i + F_2$ go to the target. Contrary to superheterodyne detection, the heterodyne frequency, given by $\Delta F = F_1 - F_2 = 100$ kHz, is therefore the same for both wavelengths. The output of the interferometer is then detected by a photodiode followed by a lock-in amplifier in order to determine the modulation power P_{ac} of the interference signal (see Eq. (2.34)). Techniques similar to those used for phase interpolation in interferometry can now be applied in order to get the phase of the synthetic wavelength. For this purpose, we moved the reference mirror in steps of $\Lambda/8$ to get five 90° phase steps.

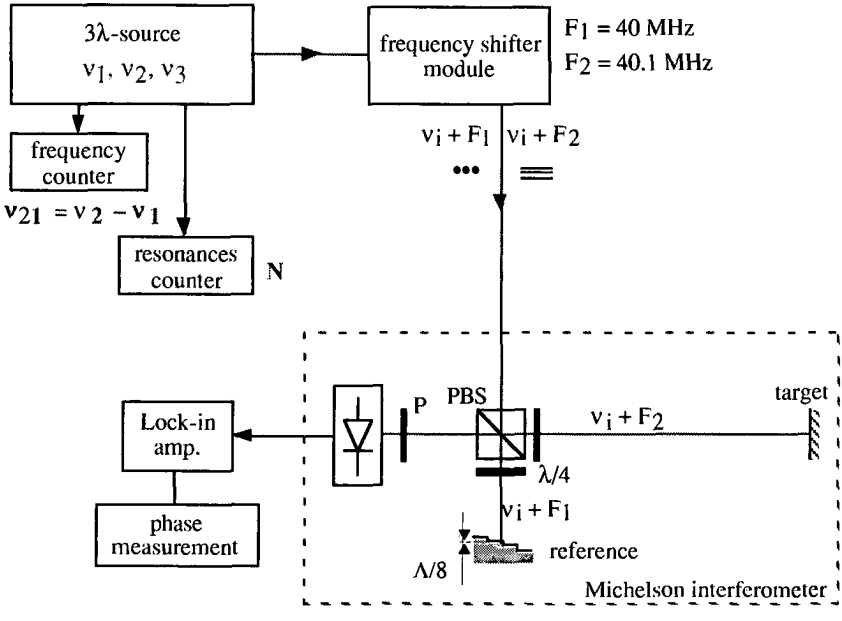

Figure 4.2: Three-wavelength heterodyne interferometer.

From the corresponding measured values of modulation power P_j (j = 1...5) the synthetic phase is calculated with the so-called 5-frame error-compensating algorithm [4.10], i.e.

$$\Delta\phi = \tan^{-1}\left(\frac{2(P_2 - P_4)}{P_1 + P_5 - 2P_3}\right). \qquad (4.2)$$

This algorithm has the advantage of being simple and having a large tolerance to miscalibration of the phase shift. Indeed, for a linear phase shift error of 10% the residual phase error was estimated to less than $2\pi/500$. In addition, the algorithm is not sensitive to detector non-linearities [4.10].

Assuming a fringe interpolation of at least $2\pi/200$ for the synthetic wavelength, it would be possible with the three-wavelength source described in chapter 3.3 to measure distances without ambiguity within 200 mm (Λ_{21} = 400 mm) and with a resolution of 10 µm (Λ_{31} = 4 mm). The technique consists of two successive two-wavelength interferometric measurements, the first one using ν_3 and ν_1 and the second one using ν_3 and ν_2 to illuminate simultaneously the Michelson-type interferometer. The corresponding synthetic wavelengths are Λ_{31} = 4 mm and Λ_{32} = 4.04 mm, respectively. For an interferometric path difference L, the phases $\Delta\phi_{31}$ and $\Delta\phi_{32}$, obtained by moving the reference mirror in steps of $\Lambda_{31}/8$ = 0.5 mm, are given by

$$\Delta\phi_{31} = \frac{4\pi}{\Lambda_{31}}L \text{ and } \Delta\phi_{32} = \frac{4\pi}{\Lambda_{32}}L. \tag{4.3}$$

The phase difference $\Delta\phi_{21} = \Delta\phi_{31} - \Delta\phi_{32}$ can then be calculated and is related to the path difference L by

$$\Delta\phi_{21} = \frac{4\pi}{\Lambda_{21}}L, \tag{4.4}$$

which is now sensitive to the synthetic wavelength Λ_{21} = 400 mm. Assuming that the resolution of $\Delta\phi_{21}$ is better than $2\pi/200$, this phase measurement can be used to evaluate the fringe order M of the synthetic wavelength Λ_{31} without ambiguity, using the algorithm

$$M = \text{Round}\left\{\frac{1}{2\pi}\left(N\Delta\phi_{21} - \Delta\phi_{31}\right)\right\}, \tag{4.5}$$

where N = 100 is the number of resonances of the Fabry-Pérot between ν_1 and ν_3, and Round(x) denotes the function which returns the closest integer to x. The path difference L can then be calculated by

$$L = \left(M + \frac{\Delta\phi_{31}}{2\pi}\right)\frac{\Lambda_{31}}{2} \tag{4.6}$$

The multiple-wavelength source allows to calibrate accurately the frequency difference $\nu_3 - \nu_1$, as already explained in chapter 3.3. The refractive index of air was estimated from the atmospheric conditions [4.11].

We checked the resolution of the setup by measuring distances over a range of 2 mm, corresponding to a displacement of $\Lambda_{31}/2$. Once again, we used the HP-laser interferometer as a reference. The measuring time was 500 ms (5x100 ms, using a five-phase stepping algorithm). For each distance, the measurement was repeated 10 times, yielding a repeatability of the order of 8 µm, which corresponds to a phase accuracy of approximately $2\pi/250$. We measured then the phase $\Delta\phi_{21}$ as described above over a range of 200 mm. The standard deviation $\delta(\Delta\phi_{21})$ was about $2\pi/400$, which is better than expected for independent measurements of $\delta(\Delta\phi_{31})$ and $\delta(\Delta\phi_{32})$. After fringe order estimation, the distance was determined using Eq. (4.6). The lower trace of Fig. 4.3 reports the multiple-wavelength interferometry (MWI) results versus the HP-interferometer, whereas the upper graph shows the corresponding deviation of the MWI mean value from the reference value given by the HP-interferometer. The standard deviation is about 9 µm.

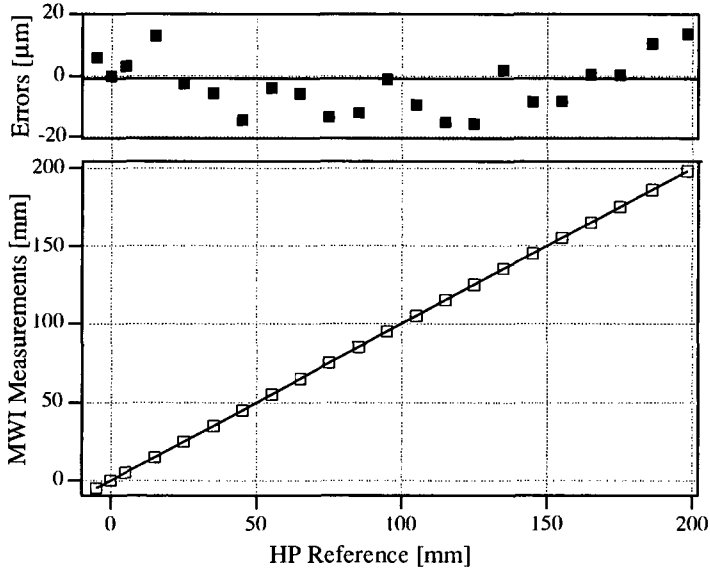

Figure 4.3: Absolute distance measurements over 200 mm.

4.3 Two-dimensional measurements

In the previous sections, we showed the advantage of heterodyne detection applied to multiple-wavelength interferometry. However, this technique requires synchronous detection of the heterodyne signal, which is not compatible with standard CCD. In view of the application of multiple-wavelength interferometry to non-cooperative targets (rough surfaces), a new type of CCD image sensor for two-dimensional synchronous detection at the heterodyne frequency was proposed and developed [4.12].

The so-called lock-in CCD is based on photocharge detection and storage. For each pixel, modulated light is detected with four or more samples per period. The corresponding photo-charges are stored at different locations (buckets). The samples are then read out by charge transfer. Amplitude, phase or power of the modulation (beat frequency) can then be determined for each pixel.

Improved versions of lock-in CCD have recently been developed at CSEM Zürich [4.13]. The schematic layout of one pixel is shown in Fig. 4.4. During the integrating and storing cycle, the photo-generated electrons are collected under the photo-gate. The charge packet is then transferred into an adjacent CCD shift register (ϕ_1–ϕ_4) for successive detection of samples. After the integration of the desired number of samples, the charge packets are transferred in parallel into the read-out CCD shift register (ϕ_a–ϕ_d) using the transfer gate (TG). The cycle of integrating and storing can be repeated over many periods, which allows to detect even low intensity signals. After an arbitrary number of demodulation cycles, the resulting charge packets are read-out sequentially. A test chip (FS21) was first fabricated with a standard CMOS process. Three different pixel layouts were designed on the chip, which allows to detect the modulated light with 8, 12 or 16 samples.

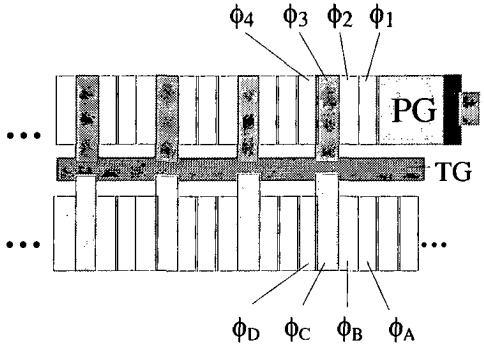

Figure 4.4: Recent version of lock-in CCD (CSEM Zürich). Schematic layout of one pixel.

The lock-in CCD can be used in multiple-wavelength heterodyne interferometry to detect the modulation power of the interference signal. For N samples per modulation period, the modulation power can be computed using the relation

$$P_{ac} = \frac{\left[\sum_{k=1}^{N} I_k \sin\left(k\frac{2\pi}{N}\right)\right]^2 + \left[\sum_{k=1}^{N} I_k \cos\left(k\frac{2\pi}{N}\right)\right]^2}{N}, \tag{4.7}$$

where I_k are the measured samples. Figure 4.5 shows the CCD read-out signal obtained by focusing the heterodyne interference signal onto a pixel which allows to detect up to 12 samples.

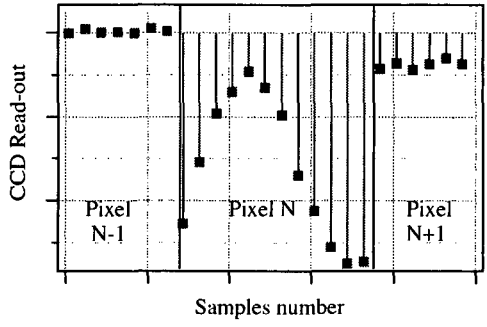

Figure 4.5: CCD read-out signal for a heterodyne interference signal focused onto one pixel.

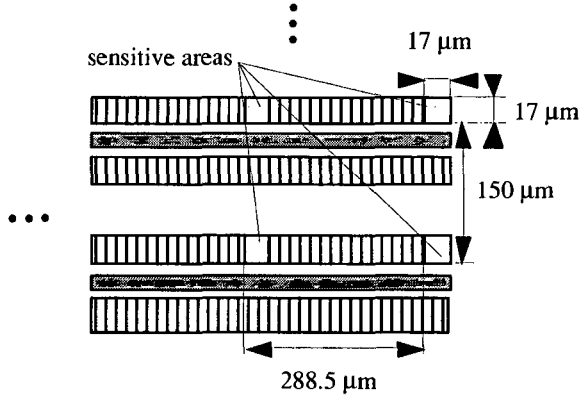

Figure 4.6: Layout of the two-dimensional lock-in CCD.

Two-dimensional array with 5×12 pixels has been designed and fabricated recently (CSEM Zürich: chip FS38). The layout is shown in Fig. 4.6. Each pixel allows to detect up to 8 samples per modulation period. The fill-factor is of about 0.7 %. This device has been used for measurements on non-cooperative targets, in order to improve the detection probability of speckles (see chapter 5).

4.4 Heterodyne frequency generation with movable reference mirror

A simpler method for heterodyne frequency generation was developed during the present work to avoid the expensive acousto-optical modulators [4.9]. If the reference mirror of a one-wavelength interferometer is moved at constant velocity v, the interferometric signal I(L+vt) (Eq. (2.14)) takes the form, for a refractive index $n \approx 1$,

$$I(L + vt) = I_1 + I_2 + 2\sqrt{I_1 I_2}\cos\left(2\pi\frac{2v}{\lambda}t + kL\right). \tag{4.8}$$

A heterodyne frequency $2v/\lambda$ is therefore produced by this way. It can be interpreted as the Doppler frequency shift due to the velocity of the reference mirror. If the mirror moves at constant speed over half the synthetic wavelength, the heterodyne frequency is generated and the phase-shifting at the synthetic wavelength is provided at the same time.

The optical set-up which was used to test this technique is depicted in Fig. 4.7. We used a moving retroreflector on a magnetic translator (loud-speaker) to provide the phase shifting at the synthetic wavelength and to generate the frequency shift for the heterodyne detection. This retroreflector moves at nearly constant speed of about 20 mm/s over a distance of about 3 mm, which produces a heterodyne frequency of $2v/\lambda \approx$ 50 kHz. A reference interference signal is detected at the output of the interferometer by means of a photodiode. After ac coupling, the reference signal is fed to a limiter amplifier in order to obtain a TTL signal of frequency $f = 2v/\lambda$. This reference TTL signal is then used by the CCD driver to generate synchronously the appropriate clocking signals for the lock-in CCD. A phase-locked loop system allows to operate the lock-in CCD synchronously even with changing heterodyne frequencies. On the other hand, the phase-shifting is controlled accurately by counting the number of periods of the reference signal, since one period corresponds to a reference displacement of $\lambda/2$, where λ is the optical wavelength.

Preliminary results were obtained by using a cooperative target (retroreflector) and one pixel of the lock-in CCD test chip (FS31), which allows to detect 12 samples per modulation period. The power of the modulated signal was computed from the CCD

output. The phase of the synthetic wavelength Λ_{31} was measured over a length L of 4 mm. Results are shown in Fig. 4.8. The charge was collected over 10 modulation periods (0.2 ms) for 5 quadrature positions (0.5 mm) of the reference retroreflector. The standard deviation of the error between the MWI and the HP-interferometer is about 4 μm, which corresponds to a phase resolution of $2\pi/500$. This resolution is good enough to perform absolute distance measurements over 200 mm with the reported three-wavelength source.

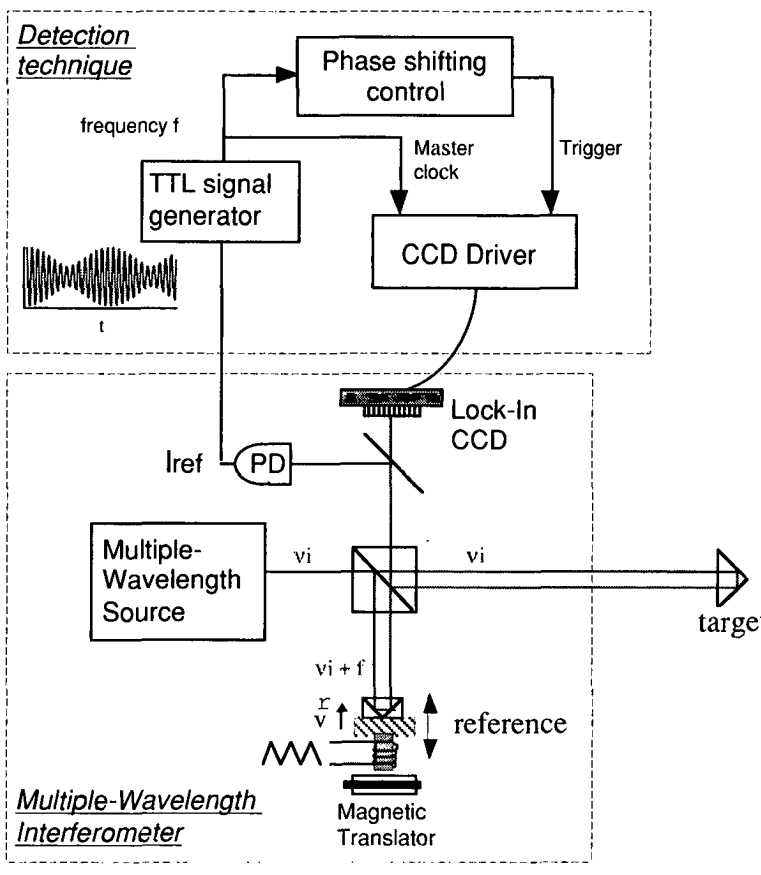

Figure 4.7: Multiple-wavelength interferometer using a movable retroreflector on a magnetic translator to produce simultaneously the heterodyne frequency and the phase shifting at the synthetic wavelength.

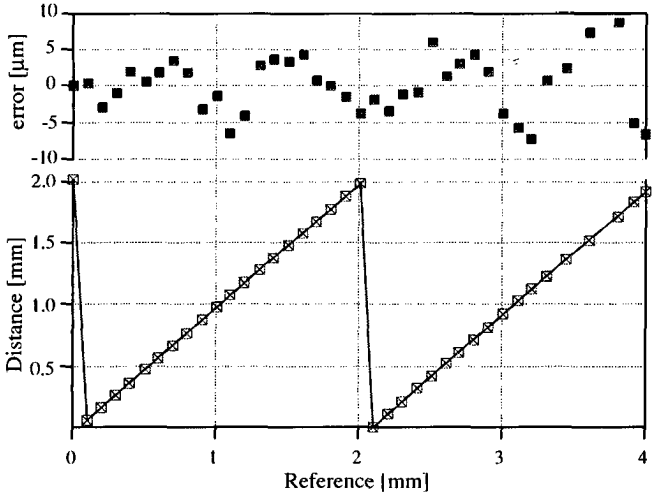

Figure 4.8: Distance measurements over a range of 4 mm, using a lock-in CCD detector (HP-interferometer as reference).

4.5 Noise consideration

As already mentioned, heterodyne detection allows to perform shot noise limited detection, even for low power in the measuring arm. This is of a great importance for measurements on diffusing surfaces, where the power of the returning light may be very low. The aim of this section is to determine the minimal optical power in the measuring arm which can be detected by the lock-in CCD, taking into account its noise level.

4.5.1 Lock-in CCD sensitivity

Figure 4.9 shows the two-stage source follower which is used in the lock-in CCD. The first part of the output stage is devoted to convert the photocharge into a voltage. The conversion factor is given by the inverse of the total effective input capacitance C_{sense}. The sensitivity, in terms of voltage/photon is given by

$$S_{VP} = \frac{e\eta}{C_{sense}}, \tag{4.9}$$

where η is the quantum efficiency of the photodetector. The lock-in CCD was tested by comparison with a calibrated detector. For a wavelength of 850 nm, we measured a sensitivity of the lock-in CCD (FS38) of about S_{VP} = 0.78 µV/photon. The saturation level is of about 10^6 photons.

Charges are accumulated while the pixel is active. The CCD sensor measures therefore the number of photons which arrive onto the sensor during the integration time T. For an average number of $\bar{n}$ photons, the output voltage becomes

$$V = \bar{n} S_{VP}. \tag{4.10}$$

The corresponding electrical power of the signal is given by

$$P_S = \frac{V^2}{R} = \frac{\bar{n}^2 S_{VP}^{\ 2}}{R}. \tag{4.11}$$

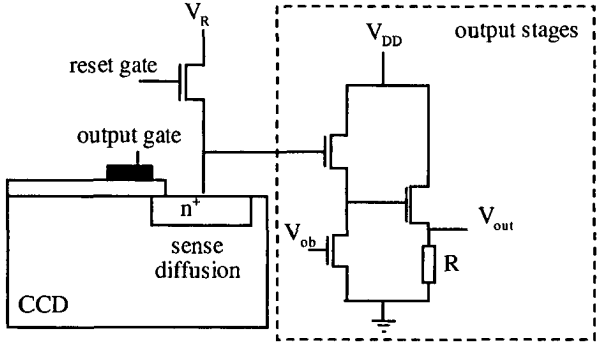

Figure 4.9: Schematic diagram of the output stage of the lock-in CCD.

4.5.2 Noise in photodetection.

Several sources of noise are inherent in the process of photon detection. They can be classified in two categories, namely, (i) shot noise and (ii) electronic noise.

The shot noise is a fundamental limitation, which is due to the random fluctuations of the photons which arrive onto the detector [4.14]. The shot noise is conveniently described by Poisson statistics. The variance of the fluctuating number of photo-electrons is therefore given by

$$\sigma_n^2 = \bar{n}_{pe}, \tag{4.12}$$

where $\bar{n}_{pe}$ is the mean number of detected photo-electrons. The corresponding number of photons is

$$\bar{n} = \frac{\bar{n}_{pe}}{\eta}, \tag{4.13}$$

where η is the quantum efficiency of the photodetector. The voltage fluctuations due to the shot noise are

$$\left\langle \Delta V^2 \right\rangle_{SN} = \frac{\sigma_n^2}{\eta^2} S_{VP}{}^2 = \frac{\bar{n}}{\eta} S_{VP}{}^2 . \tag{4.14}$$

Using Eq. (4.11) and (4.14), the electrical power corresponding to the shot noise becomes

$$P_{SN} = \frac{\left\langle \Delta V^2 \right\rangle_{SN}}{R} = \frac{\bar{n} S_{VP}{}^2}{\eta R} . \tag{4.15}$$

The electrical power of the shot noise is therefore proportional to the mean number of photons which arrive onto the detector during the observation time.

On the other hand, the detection is often limited by noise in the electronic circuit of the detector. The main source is the thermal or Johnson noise caused by the fluctuations of the thermal radiation in resistive electrical materials. The expected variance of the current across a resistor with resistance R at temperature T_e is given by [4.14]

$$\left\langle \sigma_i^2 \right\rangle = 4 k_B T_e B / R , \tag{4.16}$$

where k_B is the Boltzmann constant and B is the detection bandwidth.

In the detection circuit of Fig. 4.9, mainly three noise sources have to be considered [4.15]: (i) Johnson noise in the channel of the MOS-FET transistor, (ii) Johnson noise of the reset switch, and (iii) 1/f noise in the channel of the MOS-FET. We will consider here the number of photons corresponding to the electrical power P_{EN} of the electronic noise, namely

$$n_{EN} = \frac{\sqrt{P_{EN} R}}{S_{VP}} . \tag{4.17}$$

In our case, we measured an equivalent number of photons of about 690 for the lock-in CCD (FS38).

4.5.3 Signal-to-noise ratio for heterodyne detection

In the case of heterodyne detection, only the ac part of the interference signal is of interest. From Eq. (2.29) we find that the ac part of the optical power is of the form

$$\left(P_{opt} \right)_{ac} = 2 \sqrt{P_{opt,r} P_{opt,m}} \cos(2\pi f t + \phi) , \tag{4.18}$$

where $P_{opt,m}$ and $P_{opt,r}$ are the optical power of the measuring and reference waves, respectively. For each sample, the modulated light is integrated over a time ΔT within the modulation period and stored at a specific location (bucket). The cycle of integrating and storing is repeated over N periods. The effective integration time is therefore $T = N \times \Delta T$. Assuming that ΔT is small compared with the modulation period, the ac part of the number of photons which arrive onto the pixels during the observation time is

$$(n)_{ac} = \frac{(P_{opt})_{ac} T}{h\nu} = 2\sqrt{n_r n_m}\cos(2\pi ft + \phi), \tag{4.19}$$

where n_m and n_r are the number of photons in the measuring and reference arms, respectively. Using Eq. (4.11), the corresponding averaged electrical power is

$$P_{ac} = S_{VP}{}^2 \frac{\langle (n)_{ac}^2 \rangle}{R} = 2S_{VP}{}^2 \frac{n_r n_m}{R}. \tag{4.20}$$

Using Eqs. (4.15), (4.17) and (4.20), the signal-to-noise ratio becomes

$$SNR = \frac{P_{ac}}{P_{SN} + P_{EN}} = \frac{2n_m n_r}{\frac{(n_r + n_m)}{\eta} + n_{EN}{}^2}. \tag{4.21}$$

The optical power of the reference wave can be increased until the shot noise P_{SN} dominates the electronic noise P_{EN}. Using Eqs. (4.15) and (4.17) and assuming that $n_r >> n_m$, the minimal number of photons at which $P_{SN} = P_{EN}$ is given by

$$(n_r)_{min} = \frac{\eta R}{S_{VP}{}^2} P_{EN} = \eta n_{EN}{}^2. \tag{4.22}$$

As already mentioned, we measured a noise floor n_{EN} of about 690 photons. A typical value for the quantum efficiency η is about 0.6. The required number of photons in the reference arm for a shot noise limited detection is therefore of $(n_r)_{min} = 0.6 \times 690^2 \cong 285'700$, corresponding to the quarter of the saturation level (about 10^6). For an effective integration time T, the corresponding minimal optical power is then

$$(P_{opt,r})_{min} = (n_r)_{min} \frac{h\nu}{T}, \tag{4.23}$$

where ν is the optical frequency. In the reported experiments the effective integration time for each sample was T = 0.625 ms. For wavelengths around 800 nm, the minimal

power of the reference beam is therefore about 110 pW per pixel, corresponding to an optical intensity of 0.4 $\mu W/mm^2$ on the detector (Fig. 4.6: pixel size 17 μm x 17 μm).

The noise of the detected signal will introduce phase fluctuations, which can be explained by considering the phasor representation of a noisy component on a harmonic signal. Therefore, the signal-to-noise ratio should be high enough to ensure a good synthetic phase interpolation. The phase noise for a given SNR is found to be [4.16]

$$\delta\phi = \frac{1}{\sqrt{SNR}}. \tag{4.24}$$

From Eq. (4.24), we see that a signal-to-noise ratio of about 1000 is required to get a phase interpolation of $2\pi/200$. Using Eqs. (4.20) and (4.21) the required number n_m of photons in the measuring arm to get a certain SNR is found to be

$$n_m = \frac{R}{2S_{VP}^2 n_r}(P_{EN} + P_{SN})SNR. \tag{4.25}$$

In the case of the shot noise limited detection, i.e. $P_{EN} = P_{SN}$ and $n_r = (n_r)_{min}$ from Eq. (4.22), the required number of photons in the measuring arm becomes

$$n_m = \frac{SNR}{\eta}, \tag{4.26}$$

which is consistent with the fact that for shot noise limited detection the signal-to-noise ratio is equal to the mean number of photo-electrons due to the signal [4.14].

Assuming a quantum efficiency of 0.6, we see that 1670 photons should arrive from the measuring arm onto each pixel to obtain a signal-to-noise ratio of 1000. We note that this is true only if the optical power of the reference beam allows a shot noise limited detection. For an integration time of 0.625 ms and a wavelength of 850 nm, we find an optical power $P_{opt,m}$ = 650 fW per pixel, corresponding to an intensity of 2.2 nW/mm^2.

For a perfect match of the measuring and reference waves, the corresponding modulation depth m of the interference signal is given by

$$m = 2\sqrt{n_r n_m}/(n_r + n_m). \tag{4.27}$$

For n_m = 1670 and n_r = 285'700, the corresponding modulation depth is of about 15 %.

4.5.4 Variations of sensitivity between samples

In practice, low interference contrast may be difficult to detect with the lock-in CCD due to the variations of sensitivity between the 8 samples per pixel. These variations result from incomplete charge transport and local potential barriers [4.13]. Measurements of the 8 samples of one pixel have been performed by exposing the sensor to a constant light source. As shown in Fig. 4.10, the maximal relative deviation between samples is about 2%. Correct measurements at low interference contrasts are therefore difficult to obtain.

Numerical simulations showed that a modulation depth of 25% is required to obtain a phase resolution of $2\pi/200$. For 285'700 photons in the reference arm (shot noise limited detection) the required number of photons in the measuring arm should be about 9000, following Eq. (4.27). For an integration time of 0.625 ms and wavelengths around 800 nm, we get an optical power of 3.5 pW per pixel, instead of 650 fW for perfectly uniform samples.

However, this problem could be solved by taking into account these variations of sensitivity in the phase calculation. The effective sensitivity of the 8 samples have therefore to be calibrated in order to use the lock-in CCD at its ultimate performance.

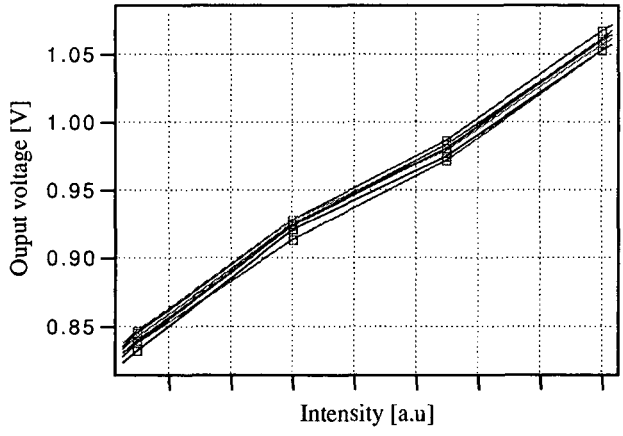

Figure 4.10: Samples of one pixel, obtained by exposing the sensor to a source of constant power.

References

[4.1] R. Dändliker, R. Thalmann and D. Prongué, " Two-wavelength laser interferometry using superheterodyne detection", *Opt. Lett.* **13**, 339-341 (1988).

[4.2] R. Dändliker, R. Thalmann and D. Prongué, "Two-wavelength laser interferometry using superheterodyne detection", *Proc. SPIE* **813**, 9-10 (1987).

[4.3] S. Manhart, R. Maurer, "Diode laser and fiber optics for dual-wavelength heterodyne interferometry", *Proc. SPIE* **1319**, 214-216 (1990).

[4.4] E. Fischer, E. Dalhoff, S. Heim and H. J. Tiziani, "High precision absolute interferometry up to 100 m", *Internat. Workshop on High Precision Navigation*, ed. K. Linkwitz, U. Hangleiter, (Ferd. Dümmlers Verlag, Bonn, 1995), p. 531-538.

[4.5] Z. Sodnik, E. Fischer, T. Ittner, H. J. Tiziani, "Two-wavelength double heterodyne interferometry using a matched grating technique", *Appl. Opt.* **30**, 3139-3144 (1991).

[4.6] E. Gelmini, U. Minoni, F. Docchio, "Tunable, double-wavelength heterodyne detection interferometer for absolute-distance measurement", *Opt. Lett.* **19**, 213-215 (1994).

[4.7] K.-D. Salewski, K.-H. Bechstein, A. Wolfram und W. Fuchs, "Absolute Distanzinterferometrie mit variabler synthetischer Wellenlänge", *tm-Technisches Messen* **63**, 5-13 (1996).

[4.8] K.-H. Bechstein and W. Fuchs, "Absolute interferometric distance measurements applying a variable synthetic wavelength", *J. Opt.* **29** (3), 179-182 (1998).

[4.9] R. Dändliker, Y. Salvadé and E. Zimmermann, "Distance measurement by multiple-wavelength interferometry", *J. Opt.* **29** (3), 105-114 (1998).

[4.10] J. Schmit and K. Creath, *Appl. Opt.* **34**, 3610 (1995).

[4.11] B. Edlén, "The refractive index of air", *Metrologia* **2**, 71-79 (1966).

[4.12] T. Spirig, P. Seitz, O. Vietze and F. Heitger, "The lock-in CCD – two dimensional synchronous detection of light", *IEEE J. Quantum Electron.*, **31**, 1705 (1995).

[4.13] T. Spirig, M. Marley and P. Seitz, "The multitap lock-in CCD with offset substraction", *IEEE Trans. Electron Devices* **44**, 1643-1647 (1997).

[4.14] B. E. A. Saleh and M. C. Teich in *Fundamental of Photonics* (Wyley & Sons, New York, 1991), chap. 17.5

[4.15] K. Knop and P. Seitz, "Image sensors", in *Sensors Update* (VCH-Verlag, Weinheim, 1995).

[4.16] R. Dändliker, "Heterodyne holographic interferometry", in *Progress in Optics*, E. Wolf, ed. (North-Holland, Amsterdam, 1980), Vol. XVII, 1-84.

Chapter 5

Distance measurements on non-cooperative targets by MWI

Applications of interferometry to non-cooperative targets (rough surfaces) give rise to two major problems: (i) The low coherent power which returns to the sensor due to the scattered light and (ii) the randomly distributed intensity and phase of the reflected light due to the speckle effect. The first problem can be overcome by using high-power sources, as already mentioned in chapter 3 or by using longer integration time. The problem of the speckle effect is partially overcome in multiple-wavelength interferometry, since the diffusely scattering target looks like a reflecting surface at the synthetic wavelength, at least from the point of view of the synthetic phase [5.1]. Nevertheless, the problem of the randomly distributed intensity remains. To improve the probability of detection by averaging, two-dimensional measurement is of a great interest [5.2].

The first section is concerned with the theoretical background of multiple-wavelength speckle interferometry. The statistical properties of a speckle pattern have been fully investigated by Goodmann [5.3], and are summarized in the beginning of this section. Then, the incoherent superposition of two correlated speckle patterns will be considered, in order to explain how the rough target is "reflecting" at the synthetic wavelength. Finally, we will investigate in detail how the probability of detection can be improved by thresholding and averaging. In the second section, a new multiple-wavelength interferometer will be presented, which allows to improve substantially the probability of detection, by means of heterodyne technique and the lock-in CCD presented in chapter 4.3. Finally, the light scattering on rough target will be considered, in order to estimate the optical power which returns to the sensor.

5.1 Statistical properties of speckle pattern

When quasi-monochromatic light is reflected on a rough surface, the resulting light observed at any observation point consists of many superposed wavelets, each arising from a different microscopic element of the surface, as shown in Fig. 5.1. For a roughness larger than the optical wavelength of the light, the optical paths of each wavelet may differ by several wavelengths. Interference between these coherent wavelets results in the granular pattern of intensity, which is known as speckle [5.3].

Speckle patterns appear in free-space propagation and in imaging systems.

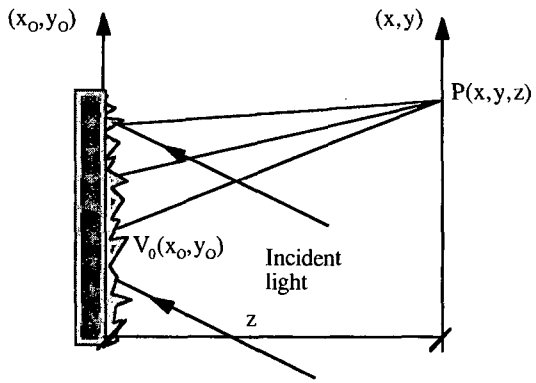

Figure 5.1: Light scattering on a rough surface.

5.1.1 First-order statistics

5.1.1.1 Statistics of a polarized speckle pattern.

We assume in this section that the rough object is illuminated by a monochromatic source and that the speckle pattern is perfectly polarized. As shown in Fig. 5.1, the complex amplitude of the resulting wave observed at the point P(x,y,z) consists of a multitude of dephased contributions from different microscopic "grains" of the rough surface. Thus the amplitude is represented as a sum of many phasor elements, namely

$$A(x,y,z) = \sum_{k=1}^{N} \frac{1}{\sqrt{N}} \cdot a_k(x,y,z) \tag{5.1}$$

where

$$a_k = |a_k(x,y,z)| \cdot e^{i\phi_k}. \tag{5.2}$$

In the following analysis, the following assumptions are made:

(i) The amplitudes $a_k/\sqrt{N}$ and phases ϕ_k of the kth phasor elements are statistically independent from each other.

(ii) The phases ϕ_k are uniformly distributed on the interval $[-\pi, \pi]$. This condition is fulfilled when the roughness of the surface is larger than the optical wavelength.

Thus, the amplitude of the sum of the phasor elements A(x,y,z) follows a random walk process in the complex plane, as illustrated in Fig. 5.2.

One gets the following properties for the real and imaginary part of the resultant field,

$$< \mathrm{Re}[A(x,y,z)] > = < \mathrm{Im}[A(x,y,z)] > = 0,$$

$$< \mathrm{Re}^2[A(x,y,z)] > = < \mathrm{Im}^2[A(x,y,z)] > \text{ and}$$

$$< \mathrm{Re}[A(x,y,z)] \cdot \mathrm{Im}[A(x,y,z)] > = 0 \tag{5.3}$$

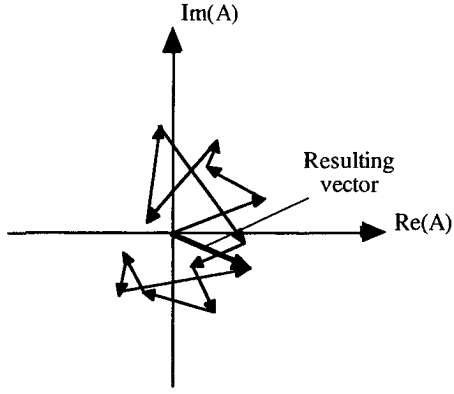

Figure 5.2: Amplitude of the phasor sum in the complex plane.

Assuming a large number N of phasor elements, it follows from the central limit theorem of statistics, that the joint probability density function of the real and imaginary part of the resulting field approaches asymptotically the circular Gaussian density function

$$p(\mathrm{Re}[A],\mathrm{Im}[A]) = \frac{1}{2\pi\sigma^2}\exp\left\{-\frac{\mathrm{Re}^2[A]+\mathrm{Im}^2[A]}{2\sigma^2}\right\}, \tag{5.4}$$

with

$$\sigma^2 = \lim_{N\to\infty}\frac{1}{N}\sum_{k=1}^{N}\frac{<|a_k|^2>}{2}. \tag{5.5}$$

The joint probability density function of the intensity I and phase ϕ, can be obtained by performing the change of variables $I = \mathrm{Re}^2[A]+\mathrm{Im}^2[A]$ and $\phi = \tan^{-1}(\mathrm{Im}[A]/\mathrm{Re}[A])$. The marginal probability density functions of the intensity or the phase alone are obtained by integrating over all possible phase or intensity values, respectively. One gets [5.3]

$$p(I) = \frac{I}{2\sigma^2}\exp\left(-\frac{I}{2\sigma^2}\right), \qquad I \geq 0, \text{ and} \tag{5.6}$$

$$p(\phi) = 1/2\pi \qquad -\pi < \phi \leq \pi. \tag{5.7}$$

The probability density function of Eq. (5.6) indicates that the most probable intensity in a speckle pattern is zero. It can also be shown from Eq. (5.6), that the mean and the variance of the intensity are

$$\langle I \rangle = 2\sigma^2 \text{ and } \left\langle \Delta I^2 \right\rangle = \langle I \rangle^2. \tag{5.8}$$

5.1.1.2 Incoherent superposition of non-correlated speckle patterns.

In many cases, the measured intensity at an observation point consists of the sum of several speckle patterns. We will here consider the incoherent superposition of K non-correlated speckle patterns, of equal mean intensity, namely

$$I = \sum_{j=1}^{K} I_j \text{ with } \left\langle I_j \right\rangle = \frac{\langle I \rangle}{K}. \tag{5.9}$$

In order to derive the probability density function (pdf) of the intensity I, we will consider the characteristic function of the individual speckle pattern, defined by the Fourier transform

$$M_j(\zeta) = \left\langle e^{i\zeta I_j} \right\rangle = \int_{-\infty}^{+\infty} e^{i\zeta I_j} p(I_j) dI_j. \tag{5.10}$$

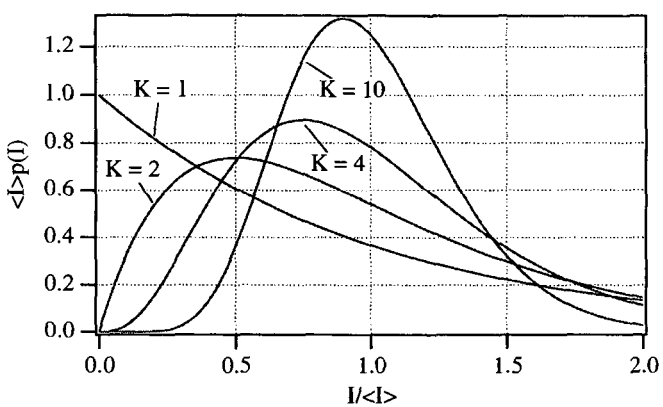

Figure 5.3: Probability density function of the intensity for different number of superposed statistically independent (non-correlated) speckle patterns M.

The Fourier transform, and thus the characteristic function of the negative exponential pdf is

$$M_j(\zeta) = \frac{1}{1 - i\zeta\langle I_j\rangle/K}. \tag{5.11}$$

In the case of statistically independent intensities I_j, the characteristic function of the total intensity I is found to be

$$M(\zeta) = \left\langle e^{i\zeta I}\right\rangle = \prod_{j=1}^{K}\left\langle e^{i\zeta I_j}\right\rangle = \left(\frac{1}{1 - i\zeta\langle I\rangle/K}\right)^K, \tag{5.12}$$

which is the product of the individual characteristic functions $M_j(\zeta)$. By performing an inverse Fourier transform, we find the probability density function [5.3]

$$p_K(I) = \frac{K^K I^{K-1}}{(K-1)!< I >^K}\exp\left(-\frac{KI}{< I >}\right). \tag{5.13}$$

Figure 5.3 shows the probability density function for different values of K. We note that for K = 1 we find Eq. (5.6), and for a very large number of speckle patterns, the pdf approaches a Dirac function at <I>.

5.1.1.3 Superposition of partially correlated speckle patterns.

So far, we only considered the sum of statistically independent speckle patterns. In many cases, especially in two-wavelength interferometry, two superposed beams coming from independent lasers are used to illuminate a rough target. The superposition is incoherent since the phase fluctuations of the laser are statistically independent. However, if the two beams illuminate the same area of the surface, the speckle pattern may be correlated. This case is important for two-wavelength interferometry.

Consider the complex amplitudes A_1 and A_2 of the two speckle patterns. The complex degree of correlation A_1 and A_2 is defined as

$$\mu = \frac{\left\langle A_1 A_2^*\right\rangle}{\sqrt{|A_1|^2|A_2|^2}}. \tag{5.14}$$

To specify the joint pdf of A_1 and A_2, we have to consider the fourth-order joint probability density function of the real valued variables $Re(A_1)$, $Im(A_1)$, $Re(A_2)$ and $Im(A_2)$. Due to the circular complex Gaussian statistics of A_1 and A_2, it can be shown [5.3] that the joint pdf becomes

$$p(A_{1r}, A_{1i}, A_{2r}, A_{2i}) = \frac{1}{4\pi^2\sigma^4(1-|\mu|^2)}\exp\left[-\frac{|A_1|^2 + |A_1|^2 - \mu A_1 A_2^* - \mu^* A_1^* A_2}{2\sigma^2(1-|\mu|^2)}\right]. \tag{5.15}$$

It has been assumed in Eq. (5.15) that $\langle|A_1|^2\rangle = \langle|A_2|^2\rangle = 2\sigma^2$. Using the appropriate transformation of variables, we get the joint pdf of the intensities and the phases

$$p(I_1,I_2,\phi_1,\phi_2) = \frac{1}{16\pi^2\sigma^4(1-|\mu|^2)}\exp\left[-\frac{I_1+I_2-2\sqrt{I_1I_2}|\mu|\cos(\phi_1-\phi_2+\psi)}{2\sigma^2(1-|\mu|^2)}\right], \quad (5.16)$$

where ψ is the phase of the complex degree of correlation μ. To find the joint pdf of I_1 and I_2, we have to integrate over ϕ_1 and ϕ_2 and find

$$p(I_1,I_2) = \frac{1}{\langle I\rangle^2(1-|\mu|^2)} J_0\left(\frac{2\sqrt{I_1I_2}|\mu|}{<I>(1-|\mu|^2)}\right)\exp\left[-\frac{I_1+I_2}{\langle I\rangle(1-|\mu|^2)}\right], \quad (5.17)$$

where J_0 is the modified Bessel function of the first kind, zero order. It is easily seen from Eq. (5.17) that for $|\mu| = 0$, which means statistically independent (non-correlated) intensities, $p(I_1,I_2) = p(I_1)p(I_2)$, as expected. For completely correlated (identical) speckle patterns ($|\mu| = 1$), we find $p(I_1,I_2) = p(I_1)\delta(I_2-I_1)$.

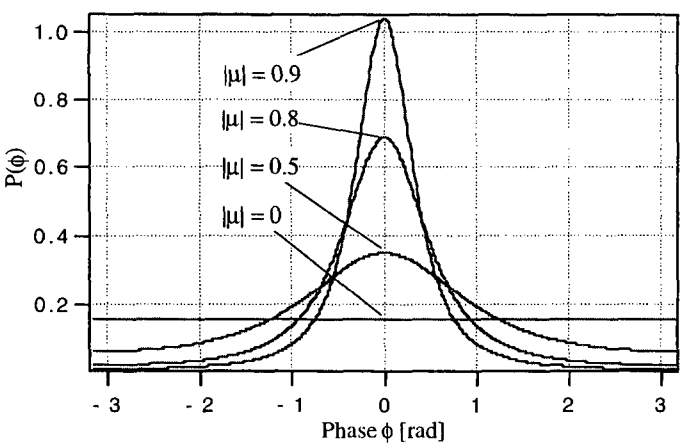

Figure 5.4: Probability density function $p(\phi)$ of the phase $\phi = \phi_2 - \phi_1 + \psi$ for different correlation factors $|\mu|$.

For two-wavelength interferometry, the joint pdf of the phases is of interest. It is obtained by integrating Eq. (5.16) over the intensities I_1 and I_2. It can be shown [5.4] that

$$p(\phi_1,\phi_2) = \frac{1-|\mu|^2}{4\pi^2\left(1-\beta^2\right)^{3/2}}\left(\beta\sin^{-1}\beta+\frac{\pi\beta}{2}+\sqrt{1-\beta^2}\right), \quad (5.18)$$

where $\beta = |\mu|\cos(\phi_2 - \phi_1 + \psi)$. Introducing the new variable $\phi = \phi_2 - \phi_1 + \psi$ and integrating the joint pdf $p(\phi_1,\phi)$ over the uniformly distributed phase ϕ_1, we obtain for the marginal pdf of ϕ alone

$$p(\phi) = \frac{1-|\mu|^2}{2\pi\left(1-|\mu|^2\cos^2\phi\right)^{3/2}}\left(|\mu|\cos\phi\sin^{-1}\left(|\mu|\cos\phi\right) + \frac{\pi|\mu|\cos\phi}{2} + \sqrt{1-|\mu|^2\cos^2\phi}\right). \tag{5.19}$$

Figure 5.4 shows the pdf of ϕ for different values of $|\mu|$. As the correlation factor increases, the pdf becomes more concentrated about small values of ϕ, indicating that the phase differences $\phi_1 - \phi_2$ are closer to ψ. Finally, using the pdf of ϕ, it can be shown [5.5] that the variance of ϕ is given by

$$\sigma_\phi^2 = \frac{\pi^2}{3} - \pi\sin^{-1}|\mu| + \left(\sin^{-1}|\mu|\right)^2 - \frac{1}{2}\sum_{n=1}^{\infty}\frac{|\mu|^{2n}}{n^2}. \tag{5.20}$$

5.1.2 Second-order statistics of speckle pattern

The first order statistics of speckle pattern do not take into account the statistical shape and size of the speckles. From the autocorrelation function of the intensity of the speckle pattern, we can deduce the geometrical shape of the speckles. Specially, the coherence length of the intensity will determine the average speckle size. The size may differ depending on the optics between the rough surface and the observation plane. In this section we will treat two cases: (i) speckle formation in free-space propagation and (ii) speckle formation in imaging system.

5.1.2.1 Free-space propagation

We will consider here the free-space propagation described by Fig. 5.1. The incident light is assumed to have in the surface plane (x_O,y_O) a complex amplitude $V_0(x_O,y_O)$. The light scattered by the rough object in the plane (x_O,y_O) is given by

$$V(x_O,y_O) = V_0(x_O,y_O)\ \rho(x_O,y_O), \tag{5.21}$$

where $\rho(x_O,y_O) = a(x_O,y_O)\exp\{i\varphi(x_O,y_O)\}$ is the complex factor of random amplitude and phase introduced by the roughness of the surface.

In order to calculate the complex amplitude A(x,y,z) of the field in the plane (x,y), we have to consider the propagation of the wave field. Using Fresnel diffraction, we get for the complex amplitude

$$A(\mathbf{x},z) = \frac{\exp(ikz)}{i\lambda z}\int d^2x_O\ V(\mathbf{x}_O)\exp\left\{i\frac{k}{2z}(\mathbf{x}_O - \mathbf{x})^2\right\}, \tag{5.22}$$

where the two-dimensional vectors $\mathbf{x} = (x,y)$ and $\mathbf{x}_O = (x_O, y_O)$ have been introduced.

The autocorrelation function $R_I(\Delta\mathbf{x})$ of the intensity for Gaussian circular pdf is given by [5.3]

$$R_I(\Delta\mathbf{x}) = \langle I(\mathbf{x}+\Delta\mathbf{x})I(\mathbf{x})\rangle = \langle I\rangle^2\left(1 + \left|\mu_A(\Delta\mathbf{x})\right|^2\right), \tag{5.23}$$

where

$$\mu_A(\Delta\mathbf{x}) = \frac{< A(\mathbf{x}+\Delta\mathbf{x})A^*(\mathbf{x}) >}{\sqrt{\left|A(\mathbf{x}+\Delta\mathbf{x})\right|^2\left|A(\mathbf{x})\right|^2}} \tag{5.24}$$

is the complex degree of correlation of $A(\mathbf{x})$. Using Eq. (5.22), the autocorrelation function of the complex amplitude becomes

$$\begin{aligned}\left\langle A(\mathbf{x}+\Delta\mathbf{x})A^*(\mathbf{x})\right\rangle = \frac{1}{\lambda^2 z^2}\exp\left\{-i\frac{\pi}{\lambda z}\Delta\mathbf{x}(2\mathbf{x}+\Delta\mathbf{x})\right\}\\ \times\int d^2x_O d^2x'_O < V(\mathbf{x}_O)V^*(\mathbf{x}'_O) > \exp\left\{i\frac{\pi}{\lambda z}(\mathbf{x}_O{}^2 - \mathbf{x}'_O{}^2)\right\}\\ \times\exp\left\{-i\frac{2\pi}{\lambda z}\left[\mathbf{x}_O(\mathbf{x}+\Delta\mathbf{x}) - \mathbf{x}'_O\mathbf{x}\right]\right\}.\end{aligned} \tag{5.25}$$

In order to further simplify the calculations, we assume that the roughness of the surface has a very short correlation length compared to the wavelength of the source. In that case, we have

$$\left\langle V(\mathbf{x}_O)V^*(\mathbf{x}'_O)\right\rangle \approx \kappa V_0(\mathbf{x}_O)V_0{}^*(\mathbf{x}'_O)\delta(\mathbf{x}_O - \mathbf{x}'_O), \tag{5.26}$$

where κ is a proportionality constant [5.3]. Using Eq. (5.26), the autocorrelation function of the amplitude is found to be

$$\left\langle A(\mathbf{x}+\Delta\mathbf{x})A^*(\mathbf{x})\right\rangle = \frac{\kappa}{\lambda^2 z^2}\exp\left\{-i\frac{\pi}{\lambda z}\Delta\mathbf{x}(2\mathbf{x}+\Delta\mathbf{x})\right\}\hat{I}_0\left(\frac{\Delta\mathbf{x}}{\lambda z}\right), \tag{5.27}$$

where

$$\hat{I}_0\left(\frac{\Delta\mathbf{x}}{\lambda z}\right) = \int d^2x_O\left|V_0(\mathbf{x}_O)\right|^2\exp\left\{-\frac{i2\pi}{\lambda z}\mathbf{x}_O\Delta\mathbf{x}\right\} \tag{5.28}$$

is the Fourier transform of the illumination intensity $I_0(\mathbf{x}_O) = |V_0(\mathbf{x}_O)|^2$. Using Eq. (5.23), the autocorrelation of the intensity becomes

$$R_I(\Delta\mathbf{x}) = \langle I \rangle^2 \left[1 + \left| \frac{\hat{I}_0\left(\frac{\Delta\mathbf{x}}{\lambda z}\right)}{\hat{I}_0(0)} \right|^2 \right]. \tag{5.29}$$

The average speckle shape is therefore determined by the Fourier transform of the intensity distribution of the illumination.

The average area of speckles is commonly defined by the coherence area [5.6]. Using the Parseval relation and Eq. (5.27), we find

$$A_S = \int d^2\mathbf{x} \, |\mu_A(\mathbf{x})|^2 = (\lambda z)^2 \frac{\int d^2\mathbf{x}_O |I_0(\mathbf{x}_O)|^2}{\left[\int d^2\mathbf{x}_O \, I_0(\mathbf{x}_O)\right]^2}. \tag{5.30}$$

5.1.2.2 Speckles in imaging systems.

As already mentioned, formation of speckles may take place when imaging a rough surface illuminated by coherent light, as shown in Fig. 5.5. The statistical properties of the intensity in the image of a rough object have been investigated in [5.7]. Similarly to the case of free-space propagation, the amplitude in the image plane can be calculated by considering the diffraction from the object plane to the image plane. We have therefore to consider the diffraction from the object plane to the pupil plane, the pupil function of the lens, and finally the diffraction from the pupil plane to the image plane. In this chapter, it is assumed that the coherent imaging system can be described by the space invariant amplitude impulse response [5.8]

$$h(\mathbf{x}_I) = \frac{1}{\sqrt{A_p \lambda d_I}} \int d^2\mathbf{x}_p P(\mathbf{x}_p) \exp\left\{-i \frac{2\pi}{\lambda d_I} \mathbf{x}_p \mathbf{x}_I\right\}, \tag{5.31}$$

where $P(\mathbf{x}_p)$ is the pupil function of the lens and A_p is the lens area.

The complex amplitude $A(\mathbf{x}_I)$ in the image plane is therefore given by

$$A(\mathbf{x}_I) = \int d^2\mathbf{x}_O V_0(\mathbf{x}_O) O(\mathbf{x}_O) \rho(\mathbf{x}_O) h(\mathbf{x}_I + M\mathbf{x}_O), \tag{5.32}$$

where V_0 is the complex amplitude of the incident light, $O(\mathbf{x}_O)$ is the object function, $\rho(\mathbf{x}_O)$ is the complex factor of random amplitude and phase introduced by the surface roughness and M is the magnification of the imaging system.

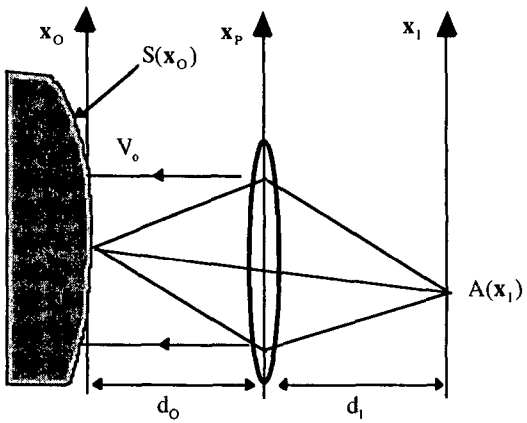

Figure 5.5: Geometry for speckle formation in an imaging system.

Similarly to the case of free-space propagation, the autocorrelation function of the complex amplitude has to be evaluated. Using Eq. (5.32) and the simplification given by Eq. (5.26) for the autocorrelation of the roughness, we find

$$\langle A(\mathbf{x}_I + \Delta\mathbf{x}_I)A^*(\mathbf{x}_I)\rangle = \kappa\int d^2\mathbf{x}_O |V_0(\mathbf{x}_O)|^2 |O(\mathbf{x}_O)|^2 h(\mathbf{x}_I + \Delta\mathbf{x}_I + M\mathbf{x}_O)h^*(\mathbf{x}_I + M\mathbf{x}_O). \tag{5.33}$$

Assuming that the intensity variations of the incident light are slow within the resolution area of the imaging system, the autocorrelation function becomes

$$\langle A(\mathbf{x}_I + \Delta\mathbf{x}_I)A^*(\mathbf{x}_I)\rangle = \kappa\left|V_0\left(\frac{\mathbf{x}_I}{M}\right)\right|^2\left|O\left(\frac{\mathbf{x}_I}{M}\right)\right|^2 C_h(\Delta\mathbf{x}_I), \tag{5.34}$$

where $C_h(\Delta\mathbf{x}_I)$ is the autocorrelation of the impulse response of the pupil $h(\mathbf{x}_I)$. Using Eq. (5.31) and the Wiener-Khinchine theorem, we get the final result

$$\langle A(\mathbf{x}_I + \Delta\mathbf{x}_I)A^*(\mathbf{x}_I)\rangle = \frac{\kappa}{A_p\lambda^2 d_I^2}\left|V_0\left(\frac{\mathbf{x}_I}{M}\right)\right|^2\left|O\left(\frac{\mathbf{x}_I}{M}\right)\right|^2 \hat{I}_p\left(\frac{\Delta\mathbf{x}_I}{\lambda d_I}\right) \tag{5.35}$$

where $\hat{I}_p$ is the Fourier transform of $|P(\mathbf{x}_P)|^2$, which is the intensity transmission of the pupil. The speckle shape is therefore determined by the geometry of the pupil. For a circular pupil of diameter D, the autocorrelation function of the intensity, obtained from Eq. (5.23), becomes

$$R_I(r) = <1>^2 \left[1 + \left| \frac{2J_1\left(\frac{\pi Dr}{\lambda d_I}\right)}{\frac{\pi Dr}{\lambda d_I}} \right|^2 \right], \tag{5.36}$$

where $r^2 = |\mathbf{x}_I|^2$ and J_1 is the first order Bessel function. Using Eq. (5.30), the average speckle area becomes

$$A_S = \frac{(\lambda d_I)^2}{A_p}. \tag{5.37}$$

The average diameter of the speckles can be defined, taking into account that the average speckle shape is circular, as

$$D_S = \frac{4}{\pi}\frac{\lambda d_I}{D} \cong 1.27\frac{\lambda d_I}{D}. \tag{5.38}$$

5.1.3 Speckle statistics in two-wavelength interferometry

In two-wavelength interferometry, the rough surface is illuminated by two superposed beams of different wavelengths λ_1 and λ_2. We have therefore the case of a superposition of correlated speckle patterns at the wavelengths λ_1 and λ_2. The aim of this chapter is to calculate first the correlation factor between the two speckle patterns, and then to deduce the statistics of the phase difference $\phi_1 - \phi_2$. Finally, we will explain how the speckle statistics can be improved by using spatially separated detectors.

5.1.3.1 Correlation factor and statistics of the synthetic phase.

As already discussed in chapter 5.1.1.3, the statistics of the phases of correlated speckle patterns depend on the complex degree of correlation of the amplitudes. Calculations of the autocorrelation function have been developed in Ref. [5.1] for a Fourier transform system with a lens. In this section, we will use the same approach to calculate the autocorrelation function $<A_1A_2^*>$ for an imaging system.

With reference to Fig. 5.5, we consider an imaging system of a rough object illuminated by two different wavelengths λ_1 and λ_2. The object functions are of the form

$$O_m(\mathbf{x}_O) = O_0(\mathbf{x}_O)\exp\left\{-i\frac{2\pi}{\lambda_m}2S(\mathbf{x}_O)\right\} \quad m = 1,2\ , \tag{5.39}$$

where $S(\mathbf{x}_O)$ is the macroscopic shape of the object. The function $O_0(\mathbf{x}_O)$ determines the local reflectivity of the object. The macroscopic shape of the object is assumed here to be a plane surface with a small tilt angle $\mathbf{s} = (s_x, s_y)$, namely

$$S(\mathbf{x}_O) = \mathbf{s}\,\mathbf{x}_O. \tag{5.40}$$

The microscopic structure of the object is described by

$$\rho_m(\mathbf{x}_O) = \exp\left[i\frac{2\pi}{\lambda_m}2g(\mathbf{x}_O)\right] \quad m = 1,2\,, \tag{5.41}$$

where $g(\mathbf{x}_o)$ is the height profile of the microscopic structure of the object. We assume that $g(\mathbf{x}_o)$ obeys a Gaussian probability density function [5.1], namely

$$p(g) = \frac{1}{\sqrt{2\pi\sigma_g}}\exp\left(-\frac{g^2}{2\sigma_g{}^2}\right), \tag{5.42}$$

where σ_g is the standard deviation of the microscopic profile or simply the surface roughness.

So far, we considered the space invariant impulse response of the imaging system. This approximation is valid provided that the image intensity is the quantity of interest. However, for interferometric applications, the phase of the complex amplitude in the image plane is of interest. We have therefore to consider the more general impulse responses [5.8]

$$h_m(\mathbf{x}_O,\mathbf{x}_I) = \frac{1}{\lambda_m{}^2 d_O d_I}\exp\left[ik_m\left(d_O + d_I + \frac{\mathbf{x}_I{}^2}{2d_I} + \frac{\mathbf{x}_O{}^2}{2d_O}\right)\right]$$
$$\times\int d^2x_p P(\mathbf{x}_p)\exp\left[-i\frac{k_m}{d_I}\mathbf{x}_p(\mathbf{x}_I + M\mathbf{x}_O)\right] \quad m = 1,2\,. \tag{5.43}$$

The phases of the illumination waves have also to be considered. In the following analysis, we assume that the illumination waves are plane waves propagating from the pupil plane to the object plane, namely

$$V_{im} = V_{om}\exp\left\{i\frac{2\pi}{\lambda_m}d_O\right\} \quad m = 1,2\,, \tag{5.44}$$

where V_{om} are the complex amplitudes of the incident light at each wavelength. The amplitudes of the speckle patterns at each wavelength take the form,

$$A_m(\mathbf{x}_I) = \int d^2x_O V_m(\mathbf{x}_O) O_m(\mathbf{x}_O) \rho_m(\mathbf{x}_O) h(\mathbf{x}_i + M\mathbf{x}_O) \quad m = 1,2. \tag{5.45}$$

We consider a detector in the image plane at a lateral position $\mathbf{x}_I$. Using Eqs. (5.39)–(5.45), it can be shown (see Annex A) that the complex degree of correlation is

$$\mu(\mathbf{x}_I) \approx \left[1 - \frac{D_S}{M\Lambda}\left|\frac{\mathbf{x}_I}{d_I} - 2\mathbf{s}\right|\right] \exp\left(-\frac{4\pi^2}{\Lambda^2} 2\sigma_g^{\,2}\right) \exp\left\{i\frac{2\pi}{\Lambda} d(\mathbf{x}_I)\right\}, \tag{5.46}$$

where

$$d(\mathbf{x}_I) = 2d_O + d_I - 2\mathbf{s}\frac{\mathbf{x}_I}{M} + \frac{\mathbf{x}_I^{\,2}}{2d_I}\left(1 + \frac{1}{M}\right). \tag{5.47}$$

D_S is the average speckle diameter defined by Eq. (5.38), and D_S/M is the resolution of the imaging system in the object plane.

The modulus of the correlation factor decreases with decreasing synthetic wavelength and increasing surface roughness σ_g. In addition, a surface tilt decreases the correlation of the two speckle fields, if the resolution of the imaging system D_S/M cannot be neglected compared to the synthetic wavelength Λ. For a lateral position $\mathbf{x}_I \neq 0$ of the detector, the decorrelation depends on the vectorial addition of $2\mathbf{s}$ and $\mathbf{x}_I/d_I$. The resulting vector can be interpreted as the surface tilt "seen" by the detector. The decorrelation due to a tilt is increased for large distances, since the object resolution D_S/M becomes larger.

From Eqs. (5.46) and (5.47) we can see that the phase of the correlation factor is

$$\psi = \frac{2\pi}{\Lambda}\left[2d_O + d_I - 2\mathbf{s}\frac{\mathbf{x}_I}{M} + \frac{\mathbf{x}_I^{\,2}}{2d_I}\left(1 + \frac{1}{M}\right)\right]. \tag{5.48}$$

The phase of the correlation factor is therefore only sensitive to the synthetic wavelength Λ and not to the optical wavelength λ. In addition, the phase is connected to the distance separating the detected area of the object and the detector $d(\mathbf{x}_I)$.

In two-wavelength interferometry, we measure directly the phase difference $\phi_2 - \phi_1$ between the two random phases ϕ_1 and ϕ_2 of the speckle fields. The measured phase $\phi_2 - \phi_1$ is then used to estimate the phase ψ of the correlation factor. Therefore, the variable $\phi = \phi_2 - \phi_1 + \psi$ can be interpreted as the statistical fluctuations of the phase measurement. The probability density function of the phase is then described by Eq. (5.19). The standard deviation of the phase measurement is therefore given by Eq. (5.20), and

depends on the modulus of the correlation factor |μ|. In order to obtain a phase resolution of $2\pi/200$, a correlation factor of 0.9997 is required.

In absolute distance measurements, the macroscopic average distance of the surface from the imaging lens, namely $d_0 - s\,x_l/M$, is of interest. We note that for a lateral position $x_l \neq 0$ of the detector, a systematic error on the phase will occur, due to the last term of Eq. (5.47). For highly accurate absolute distance measurement, a correction

$$C = \frac{x_l^2}{2d_l}\left(1 + \frac{1}{M}\right) \tag{5.49}$$

has therefore to be substracted to the measured distance.

5.1.3.2 Probability of detection

As already mentioned, the most probable intensity in a speckle pattern is zero. In practice, the intensity of the speckle pattern is integrated over the surface of the detector. If a speckle pattern is observed by means of a small detector compared to the speckle size, the pdf of the measured intensity is given by Eq. (5.6), and the variance is $\langle \Delta I_d^2 \rangle = \langle I \rangle^2$. For K speckles within the detection area, the measured intensity is the result of the superposition of K non-correlated intensities. The measured intensity is therefore given by the sum of the intensities of all speckles, which is equivalent to the intensity resulting from the incoherent superposition of K non-correlated speckle patterns [5.3]. The pdf of the measured intensity is therefore given by Eq. (5.13), and the variance is $\langle \Delta I_d^2 \rangle = \langle I \rangle^2 / K$.

In speckle interferometry, we have to consider the interference of a speckle pattern which returns from a scattering object and a uniform reference beam. For a heterodyne interferometer, and assuming a single speckle within the detector surface, the interference signal is

$$I(t) = I_{ref} + I_s + 2\,\mathrm{Re}\left\{A_{ref} A_s^* \exp(i2\pi ft)\right\}, \tag{5.50}$$

where I_{ref} and I_s are the intensities of the reference beam and of the speckle, and A_{ref} and A_s are the corresponding complex amplitudes. For K speckles within the detector surface, the resulting signal is given by the sum of K interference signals I_j, namely

$$I_{tot} = \sum_{j=1}^{K} I_j = I_{ref} + \sum_{j=1}^{K} I_{sj} + 2\,\mathrm{Re}\left\{A_{ref} \sum_{j=1}^{K} A_{sj}^* \exp(i2\pi ft)\right\}, \tag{5.51}$$

where I_{sj} and A_{sj} are the intensity and amplitude of the jth speckle, respectively. The interference signal is therefore given by the superposition of K speckles on an amplitude

basis. It can be shown [5.3] that the amplitude resulting from the addition of speckle patterns on an amplitude basis is also a circular complex Gaussian variable. The statistical properties of the heterodyne signal are therefore not changed by including several speckles within the detection area. However, the detector area should contain only a few speckles, in order to obtain sufficient modulation depth.

It follows that the power of the heterodyne signal W_h obeys negative exponential statistics, namely

$$p(W_h) = \frac{1}{\langle W_h \rangle} \exp\left(-\frac{W_h}{\langle W_h \rangle} \right). \tag{5.52}$$

In two-wavelength heterodyne interferometer, one has the sum of two speckle patterns. According to Eq. (2.33), the interference signal is given by the incoherent superposition of two heterodyne signals, i.e.

$$I(t) = I_0 + \sqrt{W_1} \cos(2\pi f_1 t + \Delta\phi_1) + \sqrt{W_2} \cos(2\pi f_1 t + \Delta\phi_2), \tag{5.53}$$

where W_1 and W_2 are the power of the heterodyne signals at λ_1 and λ_2, respectively. We assume here that the average power of the two heterodyne signals are equal, i.e. $\langle W_1 \rangle = \langle W_2 \rangle$. As seen in the previous section, for a synthetic wavelength much longer than the surface roughness, the correlation factor of the two speckle fields are close to unity. In this case, the complex amplitudes of the two speckle fields are nearly equal, and therefore $W_1 = W_2$. The modulation power of I(t) becomes therefore

$$P_{ac} = W_1[1 + \cos(\Delta\phi_{12})]. \tag{5.54}$$

The modulation power is proportional to the power of the individual heterodyne signal. Therefore, it obeys also a negative exponential, i.e.

$$p(P_{ac}) = \frac{1}{\langle P_{ac} \rangle} \exp\left(-\frac{P_{ac}}{\langle P_{ac} \rangle} \right). \tag{5.55}$$

The most probable modulation power is therefore zero, even if the detector area integrates over several speckles.

However, Dändliker et al. [5.2] have shown that the speckle statistics can be improved by using several spatially separated detectors with statistically independent speckles. The problem of low-intensity speckles can be overcome by thresholding [5.1] or by adding the modulation power of all detectors. For Q detectors, the pdf of the sum of the modulation power is then, similarly to Eq. (5.13),

$$p_Q(P_{ac}) = \frac{Q^Q P_{ac}^{\,Q-1}}{(Q-1)! < P_{ac} >^Q} \exp\left(-\frac{Q P_{ac}}{< P_{ac} >} \right). \tag{5.56}$$

5.2 Experimental results

We report here the results of distance measurements on non-cooperative targets [5.9].

The system presented in section 4.4 was adapted for measurements on non-cooperative targets. The final set-up, shown in Fig. 5.6, is similar to the one used for ESPI (Electronic Speckle Pattern Interferometry) [5.10], except of the moving reference and the lock-in CCD. The imaging lens has a focal length of 100 mm. The source consists of the low-power source described in chapter 3.3 followed by the semiconductor amplifier (see chapter 3.4). We used a synthetic wavelength of 4 mm in our experiment. The test object was a plane surface of frosted aluminium at 40 cm from the imaging lens.

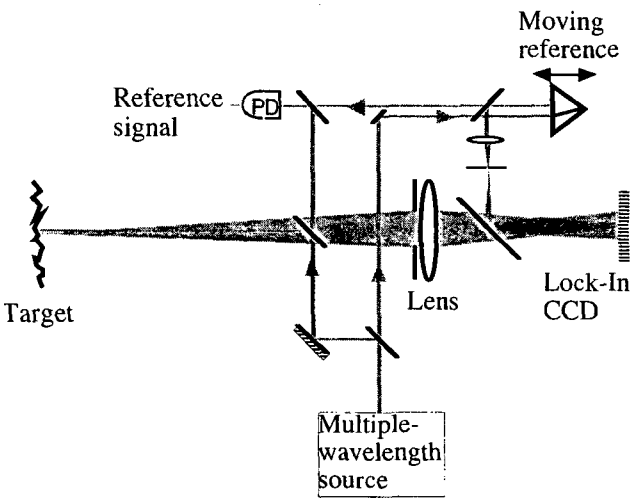

Figure 5.6: Multiple-wavelength interferometer set-up with non-cooperative target.

To improve the probability to detect "bright" speckles, we used the 2D-version of the lock-in CCD which is composed of 5x12 pixels (see Fig. 4.6). The modulation power of the interference signal is detected in ten intervals of 10 ms duration and 6 ms separation, phase shifted by 45° (see Fig. 5.7). Five 90° phase shifted values are obtained by adding two consecutive samples. The phase of the synthetic wavelength is then calculated using the five-frame error compensation algorithm (Eq. (4.2)). During the integration phase, the sensitive area of the pixel is active during 5 ms (8 x

0.625 ms). The effective integration time for one measurement is therefore of about 50 ms.

At first, we computed the phase for each pixel. Figure 5.8 shows the phases obtained from the 5x12 pixels of the lock-in CCD. The large phase errors are mainly due to the speckles of low intensity. To investigate the statistical properties of the signal, we recorded twenty statistically independent measurements by laterally moving the target at a fixed distance. We obtained by this way 1200 phase measurements, that we sorted in increasing modulation powers. Results are shown in Fig. 5.9. We note that for low modulation powers, we cannot obtain a significant value of the phase. The phase measurement can therefore be improved by thresholding with respect to the modulation power.

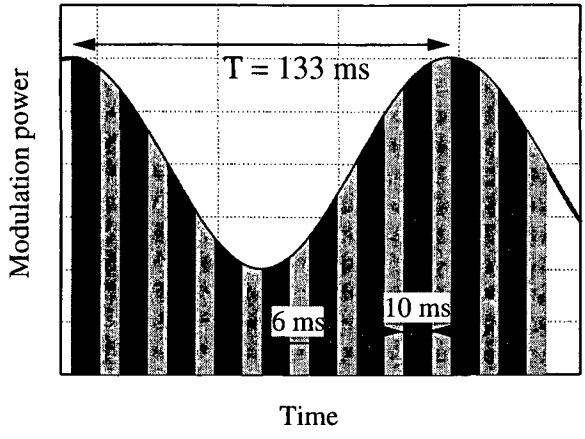

Figure 5.7: Integration phase (solid bars) and read-out phase (dashed bars) during the measuring time.

The phase fluctuations are also due to decorrelation between the two speckle fields. As already mentioned, the decorrelation is caused by surface tilt and by the surface roughness. Assuming a surface roughness of 10 μm, it can be shown from Eq. (5.46) that the correlation factor is about 0.9995 for Λ = 4 mm. The corresponding standard deviation of the phase would be 0.07 rad (Eq. (5.20)). The decorrelation caused by surface tilt depends on the image resolution in the object plane D_s/M. In our case the speckle diamater D_s was estimated to 10 μm, and the magnification factor M was about 0.3. If the surface is tilted by an angle of 10°, we see from Eq. (5.46) that the correlation factor is about 0.997, corresponding to a standard deviation of the phase of about 0.16 rad.

An appropriate signal processing can be applied to get a better phase resolution. Assuming that the object surface is plane within the illumination area, the phase measurements for each pixel can be fitted to a plane surface. This allows to measure the distance at the center of the illumination area and the tilt angle of the surface.

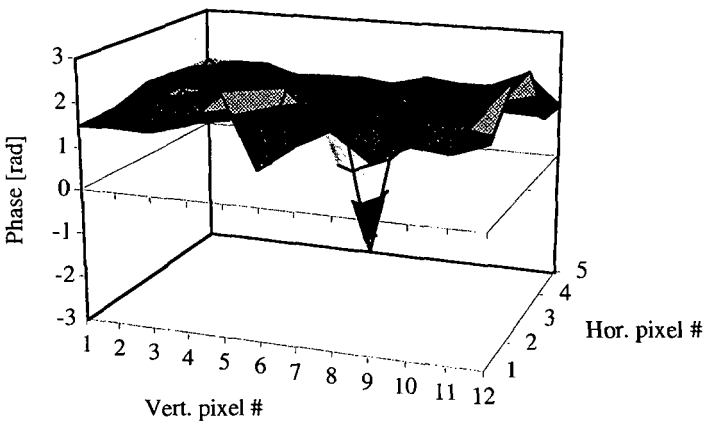

Figure 5.8: Phase measurements for the 5x12 pixels of the lock-in CCD.

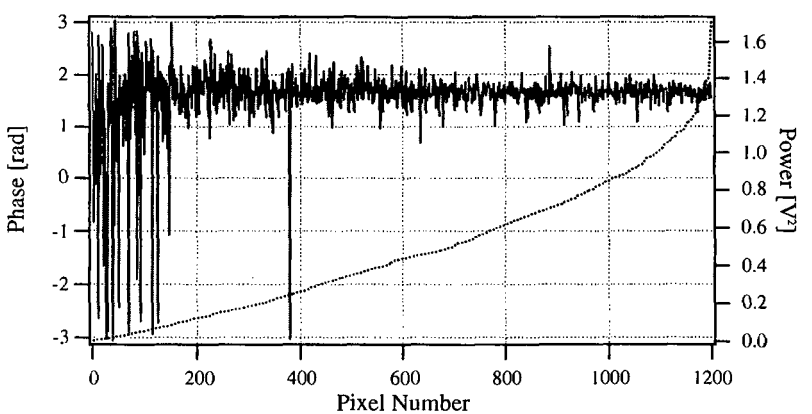

Figure 5.9: Phase measurements (solid) and power measurements (dotted), sorted by increasing power.

To improve the statistical signal quality, only 30 pixels (50% of 5x12) with the best modulation power were retained for the phase evaluation in our experiment. The phase

measurements for each retained pixel were then fitted to a plane surface. In this way, phase measurements at the center of the illumination area indicate a phase resolution of about $2\pi/200$, as shown in Fig. 5.10, corresponding to a distance resolution of about 10 μm. In this case, the tilt angle was less than 1° and was therefore too small to be measured.

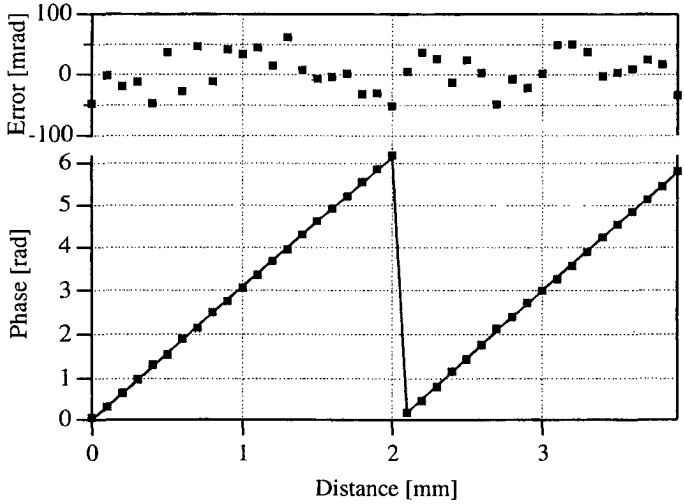

Figure 5.10: Phase measurements on non-cooperative targets over a range of 4 mm, after signal processing and thresholding.

5.3 Power limitation

One of the limiting factor for the maximal distance which can be measured with non-cooperative targets is the optical power of the scattered light which returns to the detector. From Fig. 5.11, we see that the power P_L which is collected by the lens depends on the solid angle defined by the distance d_o and the pupil diameter D. The collected power is therefore

$$P_L = P_i \rho \left(\frac{D}{d_o}\right)^2 \tag{5.57}$$

where P_i is the incident power on the target, and ρ is the diffuse reflection coefficient. The intensity in the image plane is therefore given by

$$I = \frac{4P_L}{\pi D_i^2} = \frac{4\rho}{\pi D_i^2}\left(\frac{D}{d_O}\right)^2 P_i, \tag{5.58}$$

where D_i is the diameter of the image of the illuminated spot on the target. In practice, the illuminated spot is chosen to give a diameter D_i in the image of about 2 mm, corresponding approximately to the size of the lock-in CCD.

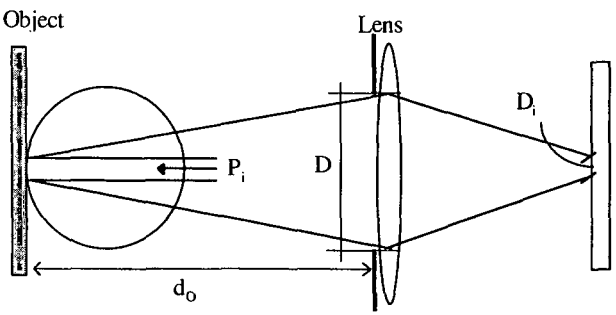

Figure 5.11: Image formation of a scattering surface.

The pupil diameter D must be chosen so that one pixel includes only a few speckles in order to get a good interference contrast [5.10]. In our experiment, we used a pupil diameter D of about 24 mm, giving a speckle diameter of about 4.5 µm. For $P_i = 90$ mW and a distance of 2.3 m, we measured an intensity of about 500 nW/cm^2 in the pupil plane. With an integration time of 0.625 ms per sample, we obtained a mean voltage of about 0.5 V from the lock-in CCD, which corresponds with $S_{VP} = 0.78$ µV/photon (see chapter 4.5) to about 600'000 photons. From Eq. (5.57), we see that the intensity in the image plane is inversely related to the square of the distance d_o. If the distance is increased by a factor 5, the intensity is decreased by a factor 25. At 11 m, one should therefore expect about 25'600 photons, corresponding to an optical power of 9 pW with an integration time of 0.625 ms (typical value). It has been shown in chapter 4.5 that at least 1670 photons must be detected to obtain a signal-to-noise ratio of 1000, corresponding to a phase resolution of $2\pi/200$. For distance measurements at 10 m, the signal quality is therefore high enough to achieve synthetic phase interpolation better than $2\pi/200$.

As already mentioned in chapter 4.3, the lock-in CCD has a fill-factor of less than 1%. In order to optimize the optical power, only those parts of the target which are seen by the pixels of the CCD should be illuminated. Therefore, the total output power can be substantially decreased by using appropriate beam-shaping optics. For that purpose, a microlens array was used in our experiment to match the illumination pattern with the

detector array, as described in Fig 5.12. A picture of the array of illumination spots on the target is shown in Fig. 5:13.

For an optical power of 20 μW per illuminated spot, we obtained a mean voltage of about 0.6 V per pixel at a distance of 2.3 m, corresponding to about 800'000 photons. At a distance of 11 m, about 32'000 photons are therefore expected, corresponding to an optical power of about 12 pW. Therefore, the corresponding signal-to-noise ratio should be high enough to achieve synthetic phase interpolation better than $2\pi/200$. We see therefore that the total optical power which is required by the CCD is of 5x12x20 μW = 1.2 mW for measurements at a distance of 10 m.

By using the microlens array, only a few mW of total optical power is therefore required for the measurements at several meter distance. This is of a great importance for an eye-safe system.

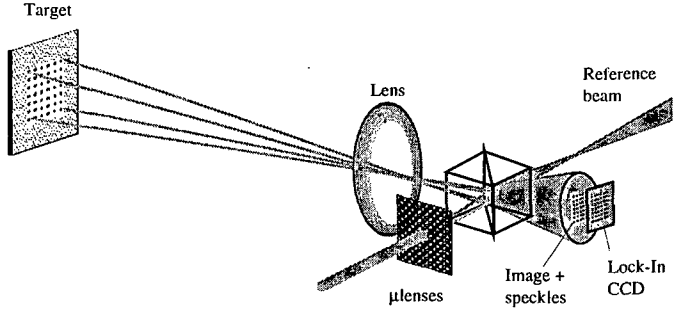

Figure 5.12: Optimization of the optical power by using an appropriate illumination pattern.

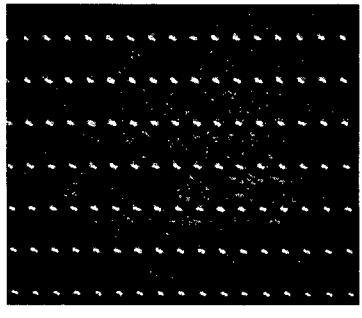

Figure 5.13: Picture of the array of illumination spots on the target (distance of 2 m).

References

[5.1] U. Vry and A. F. Fercher, "Higher-order statistical properties of speckle fields and their application to rough-surface interferometry", *J. Opt. Soc. Am. A* **3**, 988-998 (1986).

[5.2] R. Dändliker, M. Geiser, C. Giunti, S. Zatti, G. Margheri, "Improvement of speckle statistics in double-wavelength superheterodyne interferometry", *Appl. Opt.* **34**, 7197 (1995).

[5.3] J. W. Goodmann, "Statistical properties of laser speckle patterns", in *Laser Speckle and Related Phenomena*, J. C. Dainty (Springer-Verlag, Berlin, 1984).

[5.4] W.B. Davenport, W. L. Root, in *Random Signal and Noise* (McGraw Hill Book Co., New York, 1958)

[5.5] S. Donati and G. Martini, "Speckle-pattern intensity and phase: second-order conditional statistics", *J. Opt. Soc. Am.* **69**, 1690 (1979)

[5.6] J. W. Goodmann in *Statistical Optics* (J. Wiley & Sons, New York, 1985), chap. 5.6.

[5.7] S. Lowenthal and H. Arsenault, "Image formation for coherent diffuse objects: Statistical properties", *J. Opt. Soc. Am.* **60**, 1478-1483 (1970).

[5.8] J. W. Goodmann in *Introduction to Fourier Optics* (McGraw-Hill, 2nd ed., New York, 1985), chap. 5.3.

[5.9] R. Dändliker, Y. Salvadé and E. Zimmermann, "Distance measurement by multiple-wavelength interferometry", *J. Opt.* **29** (3), 105-114 (1998).

[5.10] R. Jones and C. Wykes in *Holographic and Speckle Interferometry* (Cambridge University Press, London, 1983).

Chapter 6

Limitations of interferometry due to the frequency fluctuations of laser diodes

Laser diodes are cost effective light sources which are of a great interest for interferometry. Especially, tunable laser diodes are promising for multiple-wavelength interferometry since one can choose the most appropriate synthetic wavelength with great flexibility. The novel concept of stabilized three-wavelength reported in chapter 3.3 allows to measure distances without ambiguity to within 200 mm and with a resolution better than 10 µm [6.1]. Combining time-of-flight distance measurement and multiple-wavelength interferometry allows to get micrometer accuracy over even larger distances.

However, multiple-wavelength interferometry, as classical interferometry, is limited by the coherence length of the laser diodes. Standard laser diodes exhibit a coherence length of about 10 m (see chapter 3.1). Distance measurements up to 5 m should thus be possible. However, the phase fluctuations become more important for increasing distances and the phase has to be averaged over a longer time T to reduce the statistical phase error. These phase fluctuations depend on the frequency fluctuations of the laser diodes. As already pointed out in section 3.3.4, the frequency noise spectrum $S_{\delta\nu}(f)$ is composed of two parts: a white noise part and a flicker noise part, which may become a limiting factor for interferometry.

The aim of this chapter is to relate the measured phase fluctuations, taking into account the integration time T, to the power spectral density (psd) of the frequency fluctuations of the laser sources [6.2, 6.3]. Measurements at the limit of the coherence length and the corresponding phase fluctuations will be reported.

6.1 Instantaneous phase fluctuations

Phase (or frequency) noise of laser sources is responsible for the spectral linewidth of laser emission. Indeed, for quasi-monochromatic light, the complex wavefunction is of the form

$$U(t) = V\exp[i\phi(t)]\exp(i2\pi\nu t), \tag{6.1}$$

where $\phi(t)$ is the random fluctuations of the phase. Using Eq. (2.35), we find the time-averaged interference signal

$$I = \left\langle |U(t) + U(t-\tau)|^2 \right\rangle = 2V^2 + 2V^2\,\mathrm{Re}\left\{\left\langle \exp[i\Delta\phi_\tau(t)] \right\rangle\right\}\cos(2\pi\nu\tau) \tag{6.2}$$

for an interferometric delay τ, where

$$\Delta\phi_\tau(t) = \phi(t) - \phi(t+\tau). \tag{6.3}$$

The instantaneous phase fluctuations $\Delta\phi_\tau(t)$ of the interference signal are introduced by a large number of independent events due to spontaneous emission. Therefore, they can be considered to follow a Gaussian probability density function (central limit theorem) [6.4], namely

$$p(\Delta\phi_\tau) = \frac{1}{\sqrt{2\pi\left\langle \Delta\phi_\tau^{\,2} \right\rangle}} \exp\left(-\frac{1}{2}\frac{\Delta\phi_\tau^{\,2}}{\left\langle \Delta\phi_\tau^{\,2} \right\rangle} \right). \tag{6.4}$$

Using Eq. (6.4), the ensemble average in Eq. (6.2) can be performed and yields

$$\left\langle \exp[i\Delta\phi_\tau(t)] \right\rangle = \exp\left(-\frac{1}{2}\left\langle \Delta\phi_\tau^{\,2} \right\rangle \right). \tag{6.5}$$

The fringe visibility $\mathcal{V}$ becomes therefore

$$\mathcal{V} = \exp\left(-\frac{1}{2}\left\langle \Delta\phi_\tau^{\,2} \right\rangle \right). \tag{6.6}$$

For a Lorentzian lineshape function the fringe visibility is reduced to 1/e at the limit of the coherence length, as defined in Table 2.1. From Eq. (6.6), the corresponding variance of the instantaneous phase fluctuations is

$$\left\langle \Delta\phi_{\tau_c}^{\,2} \right\rangle = 2. \tag{6.7}$$

We would like to relate now the instantaneous phase fluctuations $\Delta\phi_\tau(t)$ to the frequency noise of the light source. Equation (6.3) can be written as

$$\Delta\phi_\tau(t) = \phi(t) - \phi(t-\tau) = \int_{t-\tau}^{t} \dot{\phi}(t)\,dt, \tag{6.8}$$

where $\dot{\phi}(t) = d\phi/dt$. The statistical properties of these random fluctuations (noise) are conveniently described by power spectral densities. It can be shown that the relation between the power spectral densities corresponding to $\Delta\phi_\tau(t)$ and to $\dot{\phi}$ is given by [6.4]

$$S_{\Delta\phi_\tau}(f) = S_{\dot{\phi}}(f)\left[\left(\frac{\sin\pi f\tau}{\pi f\tau} \right)^2 \tau^2 \right]. \tag{6.9}$$

Since the frequency variation $\delta\nu$ is related to $\dot{\phi}$ by $\delta\nu = \dot{\phi}/2\pi$, we can introduce the frequency noise spectrum $S_{\delta\nu}(f)$ in Eq. (6.9), which gives

$$S_{\Delta\phi_\tau}(f) = 4\pi^2\tau^2 S_{\delta\nu}(f)\left(\frac{\sin\pi f\tau}{\pi f\tau}\right)^2. \tag{6.10}$$

The variance of the instantaneous phase fluctuations $\langle\Delta\phi_\tau^2\rangle$ can then be determined using the Parseval relation, which yields

$$\langle\Delta\phi_\tau^2\rangle = \int_0^\infty S_{\Delta\phi_\tau}(f)\,df. \tag{6.11}$$

Equation (6.11) is useful to relate the fringe visibility (Eq. (6.6)) to the frequency noise spectrum $S_{\delta\nu}(f)$. However, the instantaneous phase can never be observed physically, because of the finite detection bandwidth. Integrated phase fluctuations have therefore to be considered.

6.2 Integrated phase fluctuations

The measured phase fluctuations are given by a time averaged value of the instantaneous phase fluctuations during the observation time T, namely

$$\Delta\phi_{\tau,T}(t) = \frac{1}{T}\int_{t-T}^{t}\Delta\phi_\tau(t)dt. \tag{6.12}$$

The relation between the corresponding power spectral densities is thus given by

$$S_{\Delta\phi_{\tau,T}}(f) = S_{\Delta\phi_\tau}(f)\left(\frac{\sin\pi fT}{\pi fT}\right)^2. \tag{6.13}$$

Using Eq. (6.10), $S_{\Delta\phi_{\tau,T}}(f)$ becomes

$$S_{\Delta\phi_{\tau,T}}(f) = 4\pi^2\tau^2 S_{\delta\nu}(f)\left(\frac{\sin\pi f\tau}{\pi f\tau}\right)^2\left(\frac{\sin\pi fT}{\pi fT}\right)^2. \tag{6.14}$$

If the interferometric delay is much smaller than the integration time (which is usually the case), Eq. (6.14) can be approximated by

$$S_{\Delta\phi_{\tau,T}}(f) = 4\pi^2\tau^2 S_{\delta\nu}(f)\left(\frac{\sin\pi fT}{\pi fT}\right)^2. \tag{6.15}$$

Similarly to Eq. (6.11), the variance of the measured phase fluctuations $\langle\Delta\phi_{\tau,T}^2\rangle$ is obtained by using the Parseval relation, which gives then

$$\left\langle \Delta\phi_{\tau,T}{}^2 \right\rangle = \int_0^\infty S_{\Delta\phi_{\tau,T}}(f)\, df. \tag{6.16}$$

6.3 White frequency noise spectrum

In the case of a white frequency noise spectrum, i.e. $S_{\delta\nu}(f) = C_0$, it can be shown from Eqs. (6.10) and (6.11) that the instantaneous phase fluctuations become [6.4]

$$\left\langle \Delta\phi_{\tau}{}^2 \right\rangle = 2\pi^2 C_0 \tau. \tag{6.17}$$

From Eq. (6.7) we can easily see that the white noise level is related to the coherence time τ_c by

$$C_0 = \frac{1}{\pi^2 \tau_c}. \tag{6.18}$$

The integration of Eq. (6.14) gives for $T \geq \tau$

$$\left\langle \Delta\phi_{\tau,T}{}^2 \right\rangle = 2\frac{\tau^2}{\tau_c T}\left(1 - \frac{\tau}{3T}\right). \tag{6.19}$$

For a measuring time much greater than the interferometric delay ($T >> \tau$), Eq. (6.19) becomes

$$\left\langle \Delta\phi_{\tau,T}{}^2 \right\rangle = 2\frac{\tau^2}{\tau_c T}. \tag{6.20}$$

The variance of the phase fluctuations observed during a time $T = \tau_c$ is thus given by

$$\left\langle \Delta\phi_{\tau,\tau_c}{}^2 \right\rangle = 2\frac{\tau^2}{\tau_c{}^2}. \tag{6.21}$$

From Eqs. (6.20) and (6.21), it can easily be shown that the variance of the phase fluctuations for an integration time T can be expressed as

$$\left\langle \Delta\phi_{\tau,T}{}^2 \right\rangle = \left\langle \Delta\phi_{\tau,\tau_c}{}^2 \right\rangle \frac{\tau_c}{T}. \tag{6.22}$$

The variance of the phase fluctuations for an integration time T is thus reduced by averaging over (T/τ_c) independent observations. Therefore, the phase fluctuations observed during the time τ_c can be interpreted as the elementary phase fluctuations.

The elementary phase fluctuations can also be obtained by using statistical arguments. Indeed, assuming $\tau << \tau_c$, the phase fluctuations observed during τ_c are given by

$$\Delta\phi_{\tau,\tau_c}(t) = 2\pi\tau\Delta\nu_{\tau_c}(t), \tag{6.23}$$

where $\Delta\nu_{\tau_c}$ is the frequency fluctuation observed during the time τ_c, namely

$$\Delta\nu_{\tau_c}(t) = \frac{1}{\tau_c}\int_{t-\tau_c}^{t}\delta\nu(t')dt'. \tag{6.24}$$

The statistical variance of the elementary phase fluctuations, deduced from Eq. (6.23), is thus given by

$$\left\langle\Delta\phi^2_{\tau,\tau_c}\right\rangle = 4\pi^2\tau^2\left\langle\Delta\nu^2_{\tau_c}\right\rangle. \tag{6.25}$$

For a white frequency noise spectrum, it can be shown (see Annex B) that the variance of the frequency fluctuations observed during τ_c is

$$\left\langle\Delta\nu^2_{\tau_c}(t)\right\rangle = \frac{1}{2}\Delta\nu^2, \tag{6.26}$$

where $\Delta\nu$ is the linewidth (FWMH) of the laser emission. For a Lorentzian lineshape function, the linewidth is related to the coherence time by $\Delta\nu = 1/\pi\tau_c$ (see Table 2.1). Therefore, the variance of the elementary phase fluctuations becomes, as expected from Eq. (6.21), $\left\langle\Delta\phi^2_{\tau,\tau_c}\right\rangle = 2\tau^2/{\tau_c}^2$.

6.4 Frequency noise spectrum of stabilized laser diodes

Figure 6.1 shows the beat frequency between two standard laser diodes (SHARPLT027MD) which are stabilized on a common Fabry-Pérot resonator, as explained in chapter 3.3. We note that the beat frequency is very well fitted by a Lorentzian function. Therefore, the lineshape of standard laser diodes is also described to a good approximation by a Lorentzian function. Using the Wiener-Khintchine theorem, the fringe visibility can be considered to be a decreasing exponential, and we can use the relation $\Delta\nu = 1/\pi\tau_c$. From the beat note spectrum we measured a linewidth of $\Delta\nu = 9$ MHz, corresponding to a coherence length $L_c = 10.6$ m.

However, contrary to most other lasers, the frequency noise spectrum of a laser diode under free-running condition has two components: white noise and flicker noise. It can be expressed as $S_{\delta\nu}(f) = C_0 + C_1/f$. Typically, the flicker noise is dominant for frequencies below 100 kHz. Since the lineshape function is to a good approximation Lorentzian (see Fig. 6.1), the emission linewidth $\Delta\nu$ is mainly caused by the white noise

part of $S_{\delta\nu}(f)$. The value for C_0 is therefore approximately given by $C_0 = \Delta\nu/\pi$, which is about 2.7×10^6 Hz^2/Hz in our case.

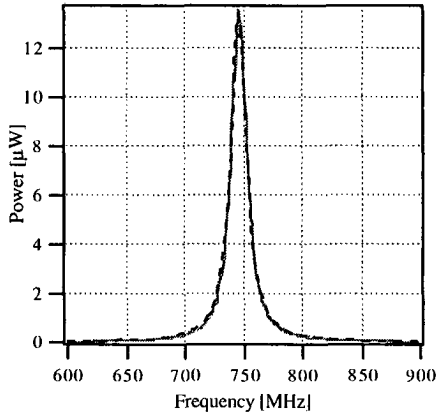

Figure 6.1: Beat note spectrum measurement (solid curve), fitted by a Lorentzian function (dashed curve).

We note that the flicker noise is divergent for $f \cong 0$. However, $S_{\delta\nu}(f)$ is reduced for low frequencies by the electronic feedback loop. As long as the regulator does not introduce additional noise, the frequency noise spectrum with electronic feedback is given by

$$S_{\partial\nu}(f)\Big|_{\text{with feedback}} = \frac{1}{|1+H(f)|^2} S_{\partial\nu}(f)\Big|_{\text{free-running}}, \tag{6.27}$$

where H(f) is the transfer function of the loop [6.5]. However, other noise sources affect the frequency stabilization: (i) the residual thermal fluctuations of the laser diodes, (ii) the shot noise and thermal noise in the photodetection and (iii) the electronic noise in the electronic feedback loop. In the case of laser diodes stabilized on a Fabry-Pérot resonator, the mechanical noise of the resonator may also affect the stabilization. From measurements of frequency noise of laser diodes stabilized on a Fabry-Pérot resonator, we observed that the frequency noise spectrum is more realistically described by the relation

$$S_{\partial\nu}(f)\Big|_{\text{with feedback}} = \frac{1}{1+f_{\min}/f} S_{\partial\nu}(f)\Big|_{\text{free-running}}, \tag{6.28}$$

where $f_{\min}$ is the cut-off frequency of the PI (proportional-integrator) regulator. Figure 6.2 shows a typical frequency noise estimated by using Eq. (6.28) with $f_{\min} = 1$ kHz, $C_1 = 10^{12}$ Hz^2 and $C_0 = 2.7 \times 10^6$ Hz^2/Hz. . In the case of laser diodes stabilized on a Fabry-Pérot resonator, we note that Eq. (6.28) allows to estimate the frequency

fluctuations relative to the Fabry-Pérot resonance rather than the absolute frequency fluctuations.

Experimental investigations were performed with stabilized standard laser diodes (SHARP LT027MD) as light sources. The aim of the experiment was to measure the phase fluctuations due to the frequency noise of laser diodes at the limit of the coherence length (10 m). The interferometric path difference, i.e. the length difference between the two arms of the interferometer, was therefore of 5 m so that the optical path difference is equal to the coherence length of the source.

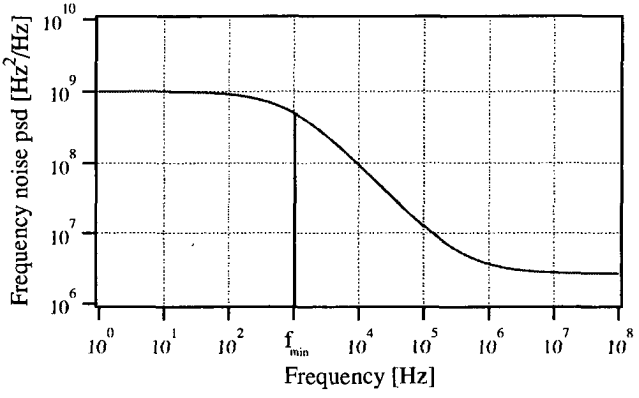

Figure 6.2: Estimated frequency noise spectrum of a stabilized laser diode.

Phase measurements at large distances are difficult to achieve by using classical (one-wavelength) interferometry, since interferometric stability at the optical wavelength (< 1 μm) is required. Therefore, we applied two-wavelength interferometry to reduce the measurement sensitivity. By using a large synthetic wavelength (200 mm), the phase fluctuations due to mechanical noise can be neglected. We used again the stabilized multiple-wavelength source described in chapter 3.3. The synthetic wavelength of Λ = 200 mm was generated. The fluctuations of the synthetic phase are connected to the frequency fluctuations of both lasers relative to the Fabry-Pérot resonances. The interferometric phase fluctuations at the individual optical wavelengths are given by Eq. (6.16). Assuming that both lasers exhibit the same frequency noise spectrum $S_{\delta\nu}(f)$, the variance of the synthetic phase fluctuations will be 2 times larger, since both lasers are independent.

In order to perform high-speed measurements, we used superheterodyne detection [6.6]. The optical set-up was therefore similar to the scheme depicted in Fig. 4.1, with an interferometric path difference of 5 m. After amplitude demodulation, the phase difference between the reference and interferometer signals was measured by means of a

phase demodulator. The phase-demodulator was specially designed for heterodyne interferometry and is fully described in [6.7]. The final stage of the demodulator is a first order low-pass filter with a cut-off frequency of about 6.9 kHz. Therefore, the measuring time must be at least 140 µs to ensure independent measurements of the synthetic phase. Similarly to Eq. (6.15), the power spectral density of the measured synthetic phase fluctuations $\Delta\Phi_{\tau,T}$ can be approximated by

$$S_{\Delta\Phi_{\tau,T}}(f) = 4\pi^2\tau^2 2S_{\delta\nu}(f)|G(f)|^2, \tag{6.29}$$

where G(f) is the transfer function of the low-pass filter of the phase demodulator. By means of a FFT spectrum analyzer we measured the psd of the phase fluctuations for free-running and stabilized laser diodes. For frequencies below 6 kHz, the values of the transfer function G(f) is approximately 1 and Eq. (6.29) can be approximated by

$$S_{\Delta\Phi_{\tau,T}}(f) \approx 8\pi^2\tau^2 S_{\delta\nu}(f). \tag{6.30}$$

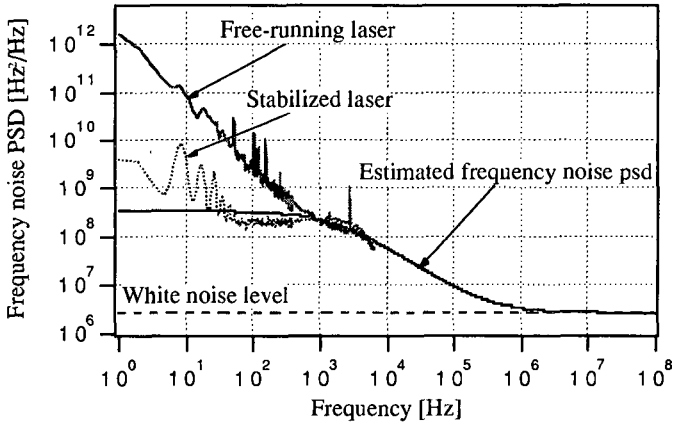

Figure 6.3: Measured frequency noise spectrum for free-running and stabilized laser diode, compared with the frequency noise psd estimated with Eq. (6.28).

For an interferometric path difference of 5 m, the delay τ is about 30 ns. Using Eq. (6.30), the frequency noise spectrum $S_{\delta\nu}(f)$ can be evaluated from the measurement of the phase fluctuations psd. Results are shown in Fig. 6.3. The measured values were fitted with the function described by Eq. (6.28). Results of the fit show a magnitude C_1 of the flicker noise of about 7×10^{11} Hz^2 and a cut-off frequency f_{min} of the regulation of

about 2 kHz. The white noise level C_0 was estimated from the linewidth measurement and found to be 2.7×10^6 Hz^2/Hz, as already mentioned.

At low-frequencies (below 20 Hz) we note that the frequency noise is larger than expected. The frequency stabilization is therefore less efficient at low frequencies. The reason may be the mechanical noise of the Fabry-Pérot resonator. We would like to mention that the measured noise level at low frequencies (i.e. about 2×10^9 Hz^2/Hz) corresponds very well to the frequency noise level previously deduced by measuring the error signal of the stabilization loop.

The analog output signal of the phase-demodulator was sampled with 12 bits resolution and a sampling period of 140 μs to obtain independent phase measurements (NB-MIO16L card and Labview software). If N consecutive samples are averaged, the integration time T will be given by Nx140 μs. In this way, the fluctuations of the synthetic phase were measured for different integration times T. The standard deviation of these fluctuations is then divided by $\sqrt{2}$ to determine the phase fluctuations due to one individual laser diode. On the other hand, we calculated the phase fluctuations from the frequency noise spectrum evaluated by Eq. (6.28) and the fluctuations that would be obtained for the white frequency noise only.

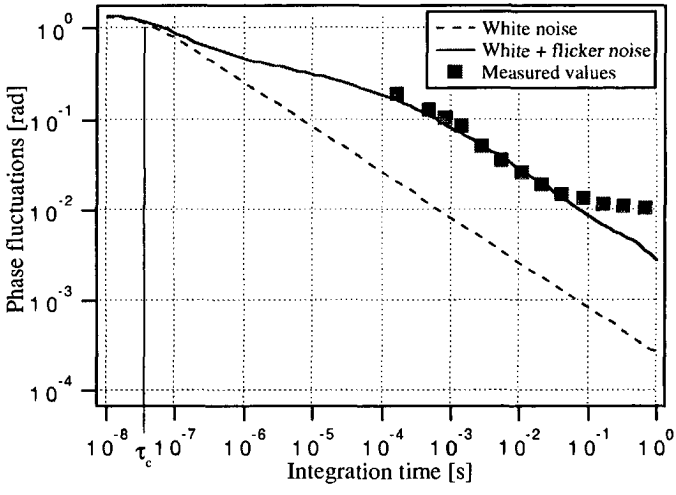

Figure 6.4: Interferometric phase fluctuations for different integration times T: measured values and calculated values for white frequency noise only (dotted curve) and for the estimated frequency noise spectrum (solid curve).

As shown in Fig. 6.4, the measured values correspond very well to the values predicted from the estimated frequency noise spectrum for integration times below 20 ms. We note

that these values are larger by one order of magnitude than the phase fluctuations calculated from the white frequency noise only. For longer integration times, the measured values are higher than expected. The reason is the observed additional noise at low frequencies shown in Fig. 6.3.

6.5 Frequency noise of DBR laser diodes

As already mentioned, SDL-5722 DBR laser diodes exhibit a linewidth of about 2.5 MHz. The coherence length is therefore about 40 m, i.e. four times larger compared with standard laser diodes. This means that the fringes can be observed up to an interferometric path difference of at least 20 m. However, similarly to standard laser diodes, their frequency noise spectrum exhibits also a 1/f noise part, which will cause fluctuations of the interferometric phase.

Comparisons of different types of GaAlAs laser diodes are reported in [6.8] in terms of frequency noise, which show that the 1/f noise of DBR lasers is reduced compared with Fabry-Pérot laser diodes. Indeed, recent frequency noise measurements of SDL DBR lasers reported in [6.9] indicate a flicker noise magnitude of about $C_1 = 1 \times 10^{11}$ Hz^2, compared with 7×10^{11} Hz^2 for our standard laser diodes. By using stabilized DBR lasers, one should therefore expect considerably smaller fluctuations of the interferometric phase for path differences up to 10 m.

6.6 Conclusion

In conclusion, we demonstrated that interferometry using laser diodes is limited by the coherence length of the source (about 10 m for standard laser diodes and 40 m for DBR laser diodes) and by the flicker noise part of the frequency noise spectrum, which is the main cause for the fluctuations of the interferometric phase. We showed that an efficient stabilization loop is required to suppress at the most the 1/f noise. From Fig. 6.4, we see that the measured phase fluctuations at the coherence length are about $2\pi/400$ for an integration time of 100 ms. The phase fluctuations in two-wavelength interferometry with two independent laser diodes are $\sqrt{2}$ times larger, i.e. about $2\pi/280$. In spite of the flicker noise, this allows to use a chain of synthetic wavelengths with $\Lambda_n/\Lambda_{n+1} = 1/100$ for highly accurate absolute distance measurements.

Previous investigations showed that the use of DBR laser diodes gives a substantial advantage for multiple-wavelength interferometry because of the wide mode-hop free tunability. We saw in this chapter that a stabilized multiple-wavelength composed of DBR laser diodes should provide better performance in terms of coherence length (about

40 m) and also in terms of interferometric phase fluctuations. These novel sources are thus very promising for highly accurate measurements of large distances.

References

[6.1] E. Zimmermann, Y. Salvadé and R. Dändliker, "Stabilized three-wavelength source calibrated by electronic means for high-accuracy absolute distance measurement", *Opt. Lett.* **21** (7), 531-533 (1995).

[6.2] Y. Salvadé, E. Zimmermann and R. Dändliker, "Limitations of interferometry due to frequency fluctuations of laser diodes", *Proc. Topical Meeting on Optoelectronic/ Displacement Measurements and Applications* (EOS, Nantes, 1997).

[6.3] Y. Salvadé, E. Zimmermann and R. Dändliker, "Limitations of multiple-wavelength interferometry due to frequency fluctuations of laser diodes", *Proc. of International Workshop on Interferometry* (Optical Society of Japan, Waco, 1996), 9-10.

[6.4] K. Petermann in *Laser diode modulation and noise* (Kluwer Academic Publishers, Dordrecht, 1988), chapter 7.

[6.5] K. Petermann in *Laser diode modulation and noise* (Kluwer Academic Publishers, Dordrecht, 1988), chapter 10.

[6.6] R. Dändliker, R. Thalmann and D. Prongué, "Two-wavelength laser interferometry using superheterodyne detection", *Opt. Lett.* **13**, 339-341 (1988).

[6.7] E. Zimmermann in *Signal Processing For Optical Phase Detection* (PhD Thesis, University of Neuchâtel, 1997), chapter 3.

[6.8] N. Sagna, C. Mandache and P. Thomann, "Noise measurements in single-mode GaAlAs diode lasers", *Proc. of the 6th European Frequency and Time Forum*, (ESTEC, Noordwijk, 1992), pp. 521-525.

[6.9] Y. Shevy and H. Deng, "Frequency-stable and ultranarrow-linewidth semiconductor laser locked directly to an atomic-cesium transition", *Opt. Lett.* **23**, 472-474 (1998).

Chapter 7

Conclusion

A new measuring system has been proposed for absolute distance measurements based on multiple-wavelength interferometry. The laser source as well as the detection technique have been optimized for highly accurate measurements over large distances on non-cooperative targets.

The source consists of laser diodes stabilized on a common stable Fabry-Pérot resonator. Emitted wavelengths around 800 nm (780–850 nm) were chosen to enable detection with CCD sensors ($\lambda < 1$ µm), and considering the great choice of laser diodes which are commercially available at these wavelengths. The novel concept of multiple-wavelength source developed in this work allows a calibration of the synthetic wavelength by beat frequency measurements with an accuracy better than 10^{-5}. The calibration accuracy is limited by the 1/f noise part of the frequency noise spectrum of laser diodes.

Low-cost standard laser diodes ($\lambda = 780$ nm) can be used for measurements up to 5 m on cooperative targets. The main drawback of standard devices is the mode-hop characteristic which limits the choice of synthetic wavelengths. Moreover, the low optical power may be insufficient for the measurements on non-cooperative targets because of the light scattering. These problems can be overcome by using high-power Distributed Bragg Reflector laser diodes. Devices emitting at 850 nm are recently commercially available. High-power (100 mW) and better spectral characteristics are provided at the same time. Their optical frequency can be tuned continuously over at least 1.5 nm, and their coherence length is about 40 m, that is 4 times longer than for the standard low power laser diodes.

A compact and portable system is a key element for industrial applications. For this reason, the use of a bulky confocal resonator as frequency reference in the multiple-wavelength source was critical. We investigated different solutions to replace the bulky resonator by a fiber-optic resonator. Modern fiber-optic technologies allow to write two identical Bragg gratings at different location in the same optical fiber. A fiber-optic Fabry-Pérot resonator composed of fiber Bragg gratings seemed therefore to be attractive. However, we have shown theoretically and experimentally that the frequency separation between two consecutive resonances does not remain sufficiently constant

over 75 GHz, because of the dispersion of the gratings. Therefore, we used a commercially available fiber-optic resonator composed of dielectric mirrors. Two DBR diode lasers and this fiber Fabry-Pérot resonator were used to realize a two-wavelength source with calibration by beat-frequency measurements. Calibration of the synthetic wavelength better than 10^{-5} has been achieved with this laser source.

Heterodyne technique allows to obtain a signal which is directly sensitive to the synthetic wavelength rather than to the optical wavelength. This is of a great importance, since interferometric stability at the optical wavelength is not any more required. Absolute distance measurements were realized over 200 mm with an accuracy of 10 µm. An inexpensive method for generating the heterodyne frequency and the phase shifting at the same time has been developed by means of a moving reference mirror. In addition, two-dimensional absolute distance measurement has been demonstrated to be feasible using a novel smart CCD sensor. We have shown that heterodyne detection with the lock-in CCD allows to perform shot noise limited detection, even for low power in the measuring arm. To obtain a phase interpolation better than $2\pi/200$, only 650 fW of optical power per pixel is required for an integration time of 0.625 ms. This is of a great importance for the measurements on diffusing surfaces, where the power of the returning light may be very low.

Applications of interferometry to non-cooperative targets (rough surfaces) suffer from the speckle effect. For a single photodiode, the most probable value for the detected interference contrast is zero, even if the detector area integrates over several speckles. However, two-dimensional measurements allow to improve the speckle statistics. The lock-in CCD is therefore of a great help for the measurements on non-cooperative targets. By fitting the phase measurements obtained for each pixel to a plane surface, the distance at the center of the illumination area and the tilt angle of the surface can be measured. In this way, distance resolution better than 10 µm has been obtained.

Optimization of the optical power is an important task for an eye-safe system. The lock-in CCD has a fill-factor of less than 1%. In order to optimize the optical power, only those parts of the target which are seen by the pixels of the CCD should be illuminated. Therefore, the total output power can be substantially decreased by using appropriate beam-shaping optics. We have shown that a microlens array can be used to match the illumination pattern with the detector array. In this way, only a few mW of total optical power is required for the measurements at several meter distance.

Finally, we have demonstrated that interferometry using laser diodes is limited by the coherence length of the source (about 10 m for standard laser diodes and 40 m for DBR

laser diodes) and by the flicker (1/f) noise part of the frequency noise spectrum, which is the main cause for the fluctuations of the interferometric phase. An efficient stabilization loop is therefore of great importance to suppress at the most the 1/f noise of laser diodes. Experimental investigations have been realized with standard laser diodes. We have shown that the phase fluctuations due to the flicker noise part are larger by one order of magnitude than the fluctuations due to the white noise part of the frequency noise spectrum. However, we have demonstrated that measurements at the limit of the coherence length (10 m) with a phase resolution better than $2\pi/200$ are feasible in spite of the flicker noise. A stabilized multiple-wavelength composed of DBR laser diodes should provide better performance in terms of coherence length (about 40 m) and also in terms of interferometric phase fluctuations compared to standard laser diodes.

Future tasks are the measurements at larger distances (10 m) on non-cooperative targets by combining time-of-flight distance measurements with multiple-wavelength interferometry. For instance, the DISTO system available from Leica can measure distances up to 30 m on non-cooperative targets with a resolution of a few mm. The combination of the DISTO with the described multiple-wavelength interferometer should allow to perform absolute distance measurements over large distances (10 m) with micrometer accuracy.

Future work will also deal with the application of multiple-wavelength interferometry to shape measurement. Commercially available laser tracking interferometers (e.g. Leica LT500) allow to follow a prism retroreflector and thus to scan the shape of large objects. The integration of a multiple-wavelength interferometer in a scanning unit should allow to measure the shape of large objects without the need of a prism retroreflector and without the severe restriction of incremental measurement. In that case, a single photodiode with superheterodyne detection can be used as detector rather than the lock-in CCD, since a local image of the surface can be realized by scanning. Signal processing can be applied after the scan to suppress at the most the speckle effect. Several additional tests should be realized to determine the reliability of multiple-wavelength interferometry for shape measurement. For instance, speckle decorrelation due to the object shape should be investigated. In addition, tests on different materials should allow to determine the effect of the object roughness and the object reflectivity on the measurement accuracy.

Annex A

Complex degree of correlation between speckle fields in the image plane for two-wavelength interferometry

(following calculations developed in Ref. [A.1] for a Fourier transform system)

We consider an imaging system of a rough object illuminated by two different wavelengths λ_1 and λ_2. The object functions are of the form

$$O_m(\mathbf{x}_O) = O_0(\mathbf{x}_O)\exp\left\{-i\frac{2\pi}{\lambda_m}2S(\mathbf{x}_O)\right\} \qquad m = 1,2\ , \tag{A.1}$$

where $S(\mathbf{x}_0)$ is the macroscopic shape of the object which is assumed here to be a plane surface with a small tilt angle $\mathbf{s} = (s_x,s_y)$, namely

$$S(\mathbf{x}_O) = \mathbf{s}\ \mathbf{x}_O. \tag{A.2}$$

The microscopic structure of the object is described by

$$\rho_m(\mathbf{x}_O) = \exp\left[i\frac{2\pi}{\lambda_m}2g(\mathbf{x}_O)\right] \qquad m = 1,2\ , \tag{A.3}$$

where $g(\mathbf{x}_O)$ is the height profile of the microscopic structure of the object. We assume also that the illumination waves are plane waves propagating from the pupil plane to the object plane, namely

$$V_m = V_{0m}\exp\left\{i\frac{2\pi}{\lambda_m}d_O\right\} \qquad m = 1,2\ . \tag{A.4}$$

The impulse responses of the imaging system are of the form

$$h_m(\mathbf{x}_O,\mathbf{x}_I) = \frac{1}{\lambda_m{}^2 d_O d_I}\exp\left[ik_m\left(d_O + d_I + \frac{\mathbf{x}_I{}^2}{2d_I} + \frac{\mathbf{x}_O{}^2}{2d_O}\right)\right]\hat{P}\left(\frac{\mathbf{x}_I + M\mathbf{x}_O}{\lambda_m d_I}\right) \quad m = 1, 2\ , \tag{A.5}$$

where

$$\hat{P}(\mathbf{p}) = \int d^2x_p P(\mathbf{x}_p)\exp\left[-i2\pi\mathbf{x}_p\mathbf{p}\right] \tag{A.6}$$

is the two-dimensional Fourier transform of the pupil function. The amplitudes of the speckle patterns in the image plane at each wavelength are

$$A_m(\mathbf{x}_I) = \int d^2x_O V_m(\mathbf{x}_O) O_m(\mathbf{x}_O) \rho_m(\mathbf{x}_O) h(\mathbf{x}_i + M\mathbf{x}_O) \quad m = 1,2. \tag{A.7}$$

Therefore, the autocorrelation function $\langle A_1 A_2^* \rangle$ can be written as

$$\langle A_1(\mathbf{x}_I) A_2^*(\mathbf{x}_I) \rangle = \int d^2x_O d^2x'_O V_1(\mathbf{x}_O) V_2^*(\mathbf{x}'_O) O_1(\mathbf{x}_O) O_2^*(\mathbf{x}'_O) \times \langle \rho_1(\mathbf{x}_O) \rho_2^*(\mathbf{x}'_O) \rangle h_1(\mathbf{x}_I, \mathbf{x}_O) h_2^*(\mathbf{x}_I, \mathbf{x}'_O). \tag{A.8}$$

We assume that the microscopic profile $g(\mathbf{x}_O)$ obeys a Gaussian probability density function, namely

$$p(g) = \frac{1}{\sqrt{2\pi\sigma_g}} \exp\left(-\frac{g^2}{2\sigma_g^2} \right), \tag{A.9}$$

where σ_g is the standard deviation of the microscopic profile. Assuming that the roughness has a very short correlation length, it can be shown [A.1] from Eqs. (A.3) and (A.9) that

$$\langle \rho_1(\mathbf{x}_O) \rho_2^*(\mathbf{x}'_O) \rangle = \kappa \exp\left(-\frac{4\pi^2}{\Lambda^2} 2\sigma_g^2 \right) \delta(\mathbf{x}_O - \mathbf{x}'_O), \tag{A.10}$$

where $\Lambda = \lambda_1 \lambda_2 / |\lambda_1 - \lambda_2|$ and κ is a proportionality constant. By substituting Eq. (A.10) into Eq. (A.8), the autocorrelation function becomes

$$\langle A_1(\mathbf{x}_I) A_2^*(\mathbf{x}_I) \rangle = \kappa \exp\left(-\frac{4\pi^2}{\Lambda^2} 2\sigma_g^2 \right) \int d^2x_O V_1(\mathbf{x}_O) V_2^*(\mathbf{x}_O) O_1(\mathbf{x}_O) O_2^*(\mathbf{x}_O) \times h_1(\mathbf{x}_I, \mathbf{x}_O) h_2^*(\mathbf{x}_I, \mathbf{x}_O). \tag{A.11}$$

Using Eqs. (A.1)–(A.5), we find

$$\langle A_1(\mathbf{x}_I) A_2^*(\mathbf{x}_I) \rangle = \frac{\kappa |V_0|^2}{\lambda_1^2 \lambda_2^2 d_O^2 d_I^2} \exp\left[i \frac{2\pi}{\Lambda} (2d_O + d_I) \right] \exp\left(i \frac{2\pi}{\Lambda} \frac{\mathbf{x}_I^2}{2d_I} \right) \times \exp\left(-\frac{4\pi^2}{\Lambda^2} 2\sigma_g^2 \right) \int d^2x_O |O_0(\mathbf{x}_O)|^2 \exp\left(i \frac{4\pi}{\Lambda} \mathbf{s}\, \mathbf{x}_O \right) \exp\left(i \frac{2\pi}{\Lambda} \frac{\mathbf{x}_O^2}{2d_O} \right) \times \hat{P}\left(\frac{\mathbf{x}_I + M\mathbf{x}_O}{\lambda_1 d_I} \right) \hat{P}^*\left(\frac{\mathbf{x}_I + M\mathbf{x}_O}{\lambda_2 d_I} \right). \tag{A.12}$$

Assuming that the object reflectivity varies slowly with respect to the resolution of the imaging system and by applying the change of variable $\mathbf{x}_O = -\mathbf{x}_I/M + \Delta\mathbf{x}_O$, Eq. (A.12) becomes

$$\langle A_1(\mathbf{x}_1)A_2^*(\mathbf{x}_1)\rangle = \frac{\kappa|V_0|^2}{\lambda_1^2\lambda_2^2 d_O^2 d_I^2}\left|O_0\left(-\frac{\mathbf{x}_I}{M}\right)\right|^2 \exp\left[i\frac{2\pi}{\Lambda}\left(2d_O + d_I + \frac{\mathbf{x}_I^2}{2d_I} - 2s\frac{\mathbf{x}_I}{M}\right)\right]$$
$$\times\exp\left(-\frac{4\pi^2}{\Lambda^2}2\sigma_g^2\right)\exp\left[i\frac{2\pi}{\Lambda}\frac{\mathbf{x}_I^2}{2M^2 d_O}\right]\int d^2\Delta\mathbf{x}_O \exp\left(i\frac{4\pi}{\Lambda}s\,\Delta\mathbf{x}_O\right)$$
$$\times\exp\left[-i\frac{2\pi}{\Lambda}\frac{\mathbf{x}_I\Delta\mathbf{x}_O}{Md_O}\right]\exp\left[i\frac{2\pi}{\Lambda}\frac{\Delta\mathbf{x}_O^2}{2d_O}\right]\hat{P}\left(\frac{M\Delta\mathbf{x}_O}{\lambda_1 d_I}\right)\hat{P}^*\left(\frac{M\Delta\mathbf{x}_O}{\lambda_2 d_I}\right). \quad (A.13)$$

Significant contributions to the autocorrelation function $\langle A_1A_2^*\rangle$ arise only for object coordinates $\Delta\mathbf{x}_O$ within the resolution area of the imaging system. The resolution area in the object plane is

$$A_O = \frac{A_S}{M^2} = \frac{d_O^2}{d_I^2}A_S, \quad (A.14)$$

where A_S is the average speckle area defined by Eq. (5.37). Therefore, if the resolution area is very small compared to Λd_O, we have

$$\frac{\Delta\mathbf{x}_O^2}{2\Lambda d_O} \approx 0. \quad (A.15)$$

Assuming an average speckle area A_S = 100 μm^2, distances d_O = 10 m and d_I = 100 mm, we obtain a resolution A_O = 1 mm^2 in the object plane. In our experiment, we used a synthetic wavelength Λ of 4 mm. The area Λd_O is therefore of 40'000 times larger than the resolution A_O. Therefore, the approximation given by Eq. (A.15) is valid in our experiment, and the quadratic phase factor in the integral of Eq. (A.13) can be neglected. In addition, using the relation $d_I = Md_O$, we have

$$\langle A_1(\mathbf{x}_1)A_2^*(\mathbf{x}_1)\rangle = \frac{\kappa I_0(\mathbf{x}_1)}{\lambda_1^2\lambda_2^2 d_O^2 d_I^2}\exp\left(-\frac{4\pi^2}{\Lambda^2}2\sigma_g^2\right)\exp\left\{i\frac{2\pi}{\Lambda}d(\mathbf{x}_1)\right\}$$
$$\times\int d^2\Delta\mathbf{x}_O \exp\left[i\frac{2\pi}{\Lambda}\Delta\mathbf{x}_O\left(2s - \frac{\mathbf{x}_I}{d_I}\right)\right]\hat{P}\left(\frac{M\Delta\mathbf{x}_O}{\lambda_1 d_I}\right)\hat{P}^*\left(\frac{M\Delta\mathbf{x}_O}{\lambda_2 d_I}\right), \quad (A.16)$$

where

$$I_0(\mathbf{x}_I) = |V_0|^2 \left| O_0\left(-\frac{\mathbf{x}_I}{M}\right)\right|^2 \tag{A.17}$$

is the object intensity, and

$$d(\mathbf{x}_I) = 2d_O + d_I - 2s\frac{\mathbf{x}_I}{M} + \frac{\mathbf{x}_I^2}{2d_I}\left(1+\frac{1}{M}\right). \tag{A.18}$$

Performing the change of variable $\mathbf{u} = M\Delta\mathbf{x}_O/\lambda_I d_I$, we find

$$\left\langle A_1(\mathbf{x}_I)A_2^*(\mathbf{x}_I)\right\rangle = \frac{\kappa I_0(\mathbf{x}_I)}{\lambda_2^2 d_I^2}\exp\left(-\frac{4\pi^2}{\Lambda^2}2\sigma_g^2\right)\exp\left\{i\frac{2\pi}{\Lambda}d(\mathbf{x}_I)\right\}$$
$$\times\int d^2u \exp\left[i2\pi\frac{\lambda_I}{M\Lambda}(2d_I s - \mathbf{x}_I)\mathbf{u}\right]\hat{P}(\mathbf{u})\hat{P}^*\left(\frac{\lambda_I}{\lambda_2}\mathbf{u}\right), \tag{A.19}$$

Since the wavelengths are assumed to be very close to each other, the ratio λ_I/λ_2 is approximately 1. Using the Wiener-Khintchine theorem, Eq. (A.19) becomes then

$$\left\langle A_1(\mathbf{x}_I)A_2^*(\mathbf{x}_I)\right\rangle = \frac{\kappa I_0(\mathbf{x}_I)}{\lambda_2^2 d_I^2}A_p\exp\left(-\frac{4\pi^2}{\Lambda^2}2\sigma_g^2\right)$$
$$\times C_p\left[\frac{\lambda_I}{M\Lambda}(\mathbf{x}_I - 2d_I s)\right]\exp\left\{i\frac{2\pi}{\Lambda}d(\mathbf{x}_I)\right\}, \tag{A.20}$$

where A_p is the lens area, and

$$C_p(\Delta\mathbf{x}) = \frac{1}{A_p}\int d^2x\ P(\mathbf{x})P(\mathbf{x}-\Delta\mathbf{x}) \tag{A.21}$$

is the normalized autocorrelation function of the pupil $P(\mathbf{x})$. It can easily be shown that the normalized correlation factor is

$$\mu(\mathbf{x}_I) = \frac{\left\langle A_1(\mathbf{x}_I)A_2^*(\mathbf{x}_I)\right\rangle}{\sqrt{\left\langle A_1(\mathbf{x}_I)A_1^*(\mathbf{x}_I)\right\rangle\left\langle A_2(\mathbf{x}_I)A_2^*(\mathbf{x}_I)\right\rangle}}$$
$$= C_p\left[\frac{\lambda_I}{M\Lambda}(\mathbf{x}_I - 2d_I s)\right]\exp\left(-\frac{4\pi^2}{\Lambda^2}2\sigma_g^2\right)\exp\left\{i\frac{2\pi}{\Lambda}d(\mathbf{x}_I)\right\}. \tag{A.22}$$

For a circular pupil of diameter D, the normalized autocorrelation of $P(\mathbf{x})$ is

$$C_p(\Delta\mathbf{x}) = \frac{2}{\pi}\left[\cos^{-1}\left(\frac{|\Delta\mathbf{x}|}{D}\right) - \frac{|\Delta\mathbf{x}|}{D}\sqrt{1-\left(\frac{|\Delta\mathbf{x}|}{D}\right)^2}\right]. \tag{A.23}$$

By expanding $C_p(\Delta x)$ in a Taylor serie around zero, Eq. (A.23) becomes to a first-order approximation

$$C_p(\Delta x) \approx 1 - \frac{4}{\pi}\frac{|\Delta x|}{D}. \tag{A.24}$$

In our experiment, this approximation can be used if

$$\frac{\lambda_l}{M\Lambda}|x_i - 2d_i s| < D. \tag{A.25}$$

For a wavelength $\lambda_l = 850$ nm, a synthetic wavelength $\Lambda = 4$ mm, a magnification factor $M = 1/100$, a distance $d_i = 100$ mm, and assuming that $|x_i| < 1$ mm and $|s| < 1$, we find

$$\frac{\lambda_l}{M\Lambda}\left(|x_i| + |2d_i s|\right) \le 4 \text{ mm} \tag{A.26}$$

which is smaller than the lens aperture $D \approx 20$ mm that we used in our experiment. Approximation of Eq. (A.24) is therefore valid. The correlation factor becomes then

$$\mu(x_i) \approx \left[1 - \frac{D_S}{M\Lambda}\left|\frac{x_i}{d_i} - 2s\right|\right] \exp\left(-\frac{4\pi^2}{\Lambda^2} 2\sigma_g{}^2\right) \exp\left\{i\frac{2\pi}{\Lambda} d(x_i)\right\}, \tag{A.27}$$

where $D_S = (4/\pi)\lambda d_i/D$ is the average diameter of speckles.

References

[A.1] U. Vry and A. F. Fercher, "Higher-order statistical properties of speckle fields and their application to rough-surface interferometry", *J. Opt. Soc. Am. A* **3**, 988-998 (1986).

Annex B

Calculation of the variance of the frequency fluctuations observed during the coherence time

The frequency fluctuation observed during the time τ_c is given by

$$\Delta\nu_{\tau_c}(t) = \frac{1}{\tau_c}\int_{t-\tau_c}^{t}\delta\nu(t')dt'. \tag{B.1}$$

It can also be written as

$$\Delta\nu_{\tau_c}(t) = \frac{1}{\tau_c}\int_{-\infty}^{+\infty}\mathrm{rect}_{\tau_c}(t'-t)\delta\nu(t')dt', \tag{B.2}$$

where the function rect_{τ_c} is defined as

$$\mathrm{rect}_{\tau_c}(t) = \begin{cases} 1 & \text{for } 0 < t < \tau_c \\ 0 & \text{elsewhere} \end{cases}. \tag{B.3}$$

To determine the variance, we calculate first the square of $\Delta\nu_{\tau_c}(t)$. Using Eq. (B.1), we find

$$\Delta\nu_{\tau_c}{}^2(t) = \frac{1}{\tau_c{}^2}\int_{-\infty}^{+\infty}dt'\int_{-\infty}^{+\infty}dt''\mathrm{rect}_{\tau_c}(t'-t)\mathrm{rect}_{\tau_c}(t''-t)\delta\nu(t')\delta\nu(t''). \tag{B.4}$$

By performing statistical averaging, we obtain the variance of the frequency fluctuations observed during τ_c, i.e.

$$\left\langle\Delta\nu_{\tau_c}{}^2(t)\right\rangle = \frac{1}{\tau_c{}^2}\int_{-\infty}^{+\infty}dt'\int_{-\infty}^{+\infty}dt''\mathrm{rect}_{\tau_c}(t'-t)\mathrm{rect}_{\tau_c}(t''-t)\left\langle\delta\nu(t')\delta\nu(t'')\right\rangle. \tag{B.5}$$

The autocorrelation function of the frequency fluctuations can be deduced using the Wiener-Khintchine theorem. Since the power spectral density of the frequency noise $S_{\delta\nu}(f)$ is a white noise of level C_0, we obtain

$$\left\langle\delta\nu(t')\delta\nu(t'')\right\rangle = \int_0^{\infty}C_0\exp[i2\pi(t'-t'')f]\,df = \frac{1}{2}C_0\delta(t'-t''). \tag{B.6}$$

Using Eqs. (B.5) and (B.6), the variance of the frequency fluctuations is found to be

$$\left\langle \Delta\nu_{\tau_c}{}^2(t) \right\rangle = \frac{1}{\tau_c{}^2}\frac{1}{2} C_0 \int_{-\infty}^{+\infty} dt' \mathrm{rect}^2_{\tau_c}(t'-t). \tag{B.7}$$

The integration of $\mathrm{rect}^2_{\tau_c}(t)$ is equal to τ_c. Moreover, the white noise level is related to the coherence time by [B.1]

$$C_0 = 1/\pi^2\tau_c. \tag{B.8}$$

By substituting Eq (B.8) into Eq. (B.7), we find

$$\left\langle \Delta\nu_{\tau_c}{}^2(t) \right\rangle = \frac{1}{\tau_c}\frac{1}{2} C_0 = \frac{1}{2}\frac{1}{\pi^2\tau_c{}^2}. \tag{B.9}$$

The full width at half maximum (FWHM) of the emission linewidth $\Delta\nu$ is related to the coherence time by

$$\Delta\nu = 1/\pi\tau_c. \tag{B.10}$$

Using Eqs. (B.9) and (B.10), we see finally that the variance of the frequency fluctuations observed during τ_c is related to the emission linewidth by

$$\left\langle \Delta\nu_{\tau_c}{}^2(t) \right\rangle = \frac{1}{2}\Delta\nu^2. \tag{B.11}$$

References

[B.1] K. Petermann in *Laser diode modulation and noise* (Kluwer Academic Publishers, Dordrecht, 1988), chapter 7.

Acknowledgments

Many people have contributed to this thesis and I would like to thank them all. First of all, I would like to express my gratitude to Prof. R. Dändliker, the director of this thesis, who gave me the opportunity to work in his research group, and for his guidance and encouragement throughout these past years. I would like also to thank him for everything he taught me during my studies. I was very proud and lucky to work under his direction. I am also grateful to the members of the jury, Prof. H. J. Tiziani, Dr. P. Thomann and Dr. H.-P. Herzig for their critical review of my thesis.

Special thanks to Dr. E. Zimmermann, who introduced me to the domain of interferometry and for his valuable suggestion about multiple-wavelength interferometry. Many thanks also to Dr. A. Courteville for fruitful discussion and for the friendly atmosphere in the office. Furthermore, I would like to thank Mr. E. Rochat and Mr. K. Haroud for their help in the domain of optical fibers. I am also grateful to the technical staff, Mr. M. Groccia and Mr. A. Jeandupeux who manufactured the electronic part of the interferometer, and Mr. P. Nussbaum and Mrs. I. Philipoussis for providing the microlens array. I would like also to express my gratitude to the other members of IMT for the pleasant atmosphere I encountered.

The project could not have been performed without the financial support of the Swiss Priority Programs OPTIQUE I and II. I wish to thank all project partners for the pleasant cooperation. Especially, I would like to thank Dr. P. Seitz and Dr. T. Spirig from CSEM Zürich for providing the lock-in CCDs, and Dr. D. Meier from Leica AG for his suggestions during the project. Many thanks to the Observatoire Cantonal de Neuchâtel, and especially to Dr. P. Thomann, for providing the electronic schemes for laser diode stabilization, for fruitful discussion and for his invaluable knowledge about phase noise of laser diodes.

Finally, I am immensely grateful to my parents for their encouragement and their support and to my wife Estelle for her assistance, her patience and, most importantly, for her love in me.